Interactions of nanoparticles with cells for nanomedical applications

AMADEUS STEVENSON

Jesus College

University of Oxford

Michaelmas Term 2014

A thesis submitted in partial fulfilment of the requirements for the degree of

Doctor of Philosophy at the University of Oxford

Interactions of nanoparticles with cells for nanomedical applications

Amadeus Stevenson, Jesus College

DPhil Condensed Matter Physics, Michaelmas Term 2014

Abstract

Nanotechnology is a rapidly growing field focused on the manipulation and control of materials with dimensions under 100 nm. The novel electronic, optical and mechanical properties observed at the nanoscale have resulted in a number of applications in catalysis, light emitting devices, solar power, self-cleaning surfaces and medicine. Medical applications of nanotechnology ("nanomedicine") are particularly promising for rapid clinical diagnosis and targeted treatments.

Understanding the interactions of nanoparticles with living matter is of fundamental importance for all application areas: manufacture, use and disposal of the growing number of nanoproducts will result in increased environmental exposure in addition to direct exposure through nanomedical applications. However, there is a lack of standard methodologies for assessing these interactions.

In this work the stability of silver-based nanoparticles was established by UV-Visible (UV-Vis) spectroscopy, atomic force microscopy (AFM) and transmission electron microscopy (TEM). The presence of a higher valence metal or polymer on the nanoparticle surface was demonstrated to improve stability.

A standard methodology was developed to study nanoparticle-cell interactions: an "atlas" of the effects of known drugs on a cell is created, and compared with the effects of a nanoparticle. *Escherichia coli* was selected as a model organism and the effects of a range of antibiotics were characterised through a combination of microbiological assays and AFM. Susceptibility, population cell growth and individual heights, widths, lengths and volumes of bacteria were obtained on a 2% agarose substrate in air.

The methodology was applied and adjusted for silver nanoparticles due to the interactions of silver with the bacterial growth medium. 10 and 30 nm silver nanoparticles and ions were found to kill *E. coli* through an internal mechanism of action, with a size-specific effect on the height of bacteria.

Finally, a novel AFM characterisation method is described to examine the mechanical properties of live bacterial and human cells in liquid.

Acknowledgments

The journey of a DPhil student is not always a straightforward one and I would like to thank Dr. Sonia Trigueros for helping me navigate it. Her supervision and help were a constant source of support during my time at Oxford. Her patience in helping a physicist understand a biological world held no bounds.

I would like to thank Dr. Sonia Contera for showing me the world of nano, and for her assistance with all things AFM.

My thanks go out to Prof. Arvind Raman and Alexander Cartagena from the University of Purdue for their fruitful collaboration and time spent at Oxford. Their enthusiastic, open-minded and generous spirit was a real inspiration.

I would also like to warmly thank Dr. Sergi Civit from the University of Barcelona for working with us and introducing me to applied statistics and R. Your patience and willingness to help was limitless.

The Life Sciences Interface Doctoral Training Centre funded four of my years in Oxford and I am extremely grateful for their support, both pecuniary and otherwise. Sam was always available to talk to and David ensured any student's troubles were brief.

Jesus College provided a wonderful setting for many enjoyable evenings spent in addition to my academic work. Their financial support through the Writing Up Scholarship and the Graduate Research Allowance was invaluable, and the staff committed to the wellbeing of their students.

I would like to thank all the support staff in the Clarendon Laboratory for making all of the work done there possible – from maintenance, stores, the workshop through to the catering staff and the administrative offices.

To the Kapinidians and Tuckerites I thank you for your support and company. It was a pleasure to share an office with you.

Finally I would like to thank my family for making it all possible, especially Kitty. Without your constant support and strength I would not have come this far.

For my parents

Contents

Chapter 1

Introduction

Nanotechnology is the manipulation and control of matter at the nanoscale (10^{-9} m). In 1959 Richard Feynman described the potential of matter at such a "*small scale*", predicting its impact on the fields of computing and biology (Feynman 1960). He anticipated that improvements in the resolving power of the electron microscope would enable an understanding of fundamental biological processes such as protein synthesis and deoxyribonucleic acid (DNA) sequencing. While advances in electron microscopy have indeed been instrumental in progressing nanotechnology, the processes and sample preparation techniques required to "*look at*" the biological specimens Feynman described ultimately limit their use (Newman 1987, Wang 2003, Segal 2009). Specimens must withstand the high-energy beams of electrons used for imaging, and either be conducting and able to withstand a vacuum, or withstand low temperatures and low pressures. The invention of the scanning tunnelling microscope (STM) in 1982, followed four years later with the atomic force microscope (AFM), for the first time allowed matter to be probed at the nanoscale without the restrictive requirements of electron microscopy (Binnig, Rohrer et al. 1982, Binnig, Quate et al. 1986). The ability to investigate nanomaterials using these technologies led to a Nobel Prize in 1986 and the rapid sustained growth of the new field of nanotechnology, illustrated in Figure 1.1.

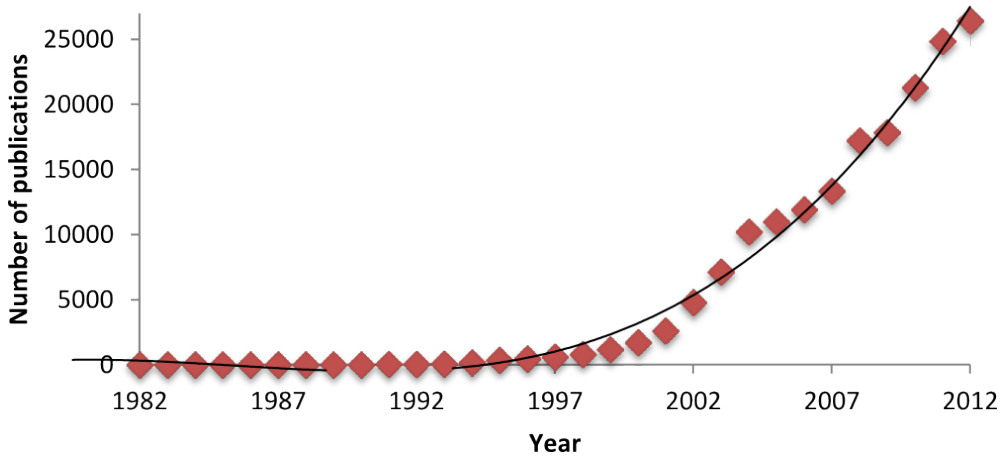

Figure 1.1 Number of nanotechnology-related peer reviewed publications per year between 1982 and 2012. Publications were sourced from the online Scopus® search engine and include a title, abstract or keyword containing "nanoparticle", "nanomaterial" or "nanotechnology". A rapid increase in publications from 1996, ten years after the invention of the atomic force microscope, can be observed.

The sustained interest in nanotechnology is due to the unique properties observed at the nanoscale. The rest of this chapter explores these novel properties and applications, summarises common nanomaterial characterisation techniques and focuses on interactions with living matter. As the number of nanotechnology applications continue to rise, the importance of establishing standard methodologies to investigate how nanomaterials interact, intentionally or otherwise, with the environment and its organisms is highlighted and forms the motivation for this thesis.

1.1 Novel properties at the nanoscale

Nanomaterials can be defined as materials with at least one dimension under 100 nm and may exist naturally (e.g. volcanic ash), incidentally (e.g. car exhaust fumes) or intentionally (nanotechnology) (Oberdorster, Oberdorster et al. 2005, Recommendation 2011/696/EU). The novel properties of nanomaterials arise from their size: surface area to volume ratios increase greatly, electromagnetic waves interact distinctly and macroscopic forces such as gravity and inertia become less important as Van der Waals, electrostatic and steric forces dominate (Bishop, Wilmer et al. 2009). An overview of some of the consequent properties is presented below.

1.1.1 Surface area related properties

The surface area to volume ratio of a three-dimensional object scales with $\frac{1}{r}$, where r is the characteristic dimension (e.g. radius of a sphere or diameter of a cube): for every halving of a cube's diameter, its surface area to volume ratio doubles (Figure 1.2). Nanomaterials are many orders of magnitude smaller than their bulk counterparts, resulting in substantial increases in surface area. For example, dividing a 1cm diameter cube into 10 nm diameter cubic nanoparticles would result in a million-fold increase in surface area.

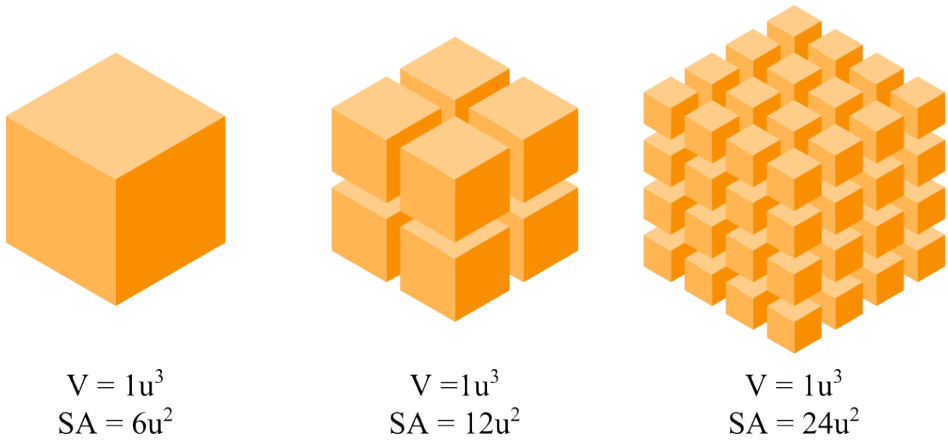

Figure 1.2 Illustration of surface area to volume scaling for cubic objects of fixed volume. As the dimensions of the object half, the surface area doubles.

Surface area is a key component in many applications such as catalysis or sensing. Lim, Jiang et al. (2009) reported a 2.5 times increase in catalytic activity for platinum-based oxygen reduction, the rate-limiting step in proton-exchange membrane fuel cells, by growing platinum "nanodendrites" on palladium core nanoparticles. Nanodendrites are highly branched nanostructures (Jian, Chen et al. 2003). The increased active surface area greatly improved catalytic performance compared to the same mass of bulk catalyst.

Yoo, Kim et al. (2008) doubled the lithium storage capacity of graphite anodes for use in lithium ion batteries by employing graphene sheets spaced with carbon nanotubes and carbon fullerenes. Fullerenes, nanotubes and graphene are respectively zero-,one- and

two- dimensional carbon nanomaterials (Geim and Novoselov 2007). The enhanced performance of the graphene nanosheets was attributed to an increase in accommodation sites for lithium ions and an altered electronic structure compared to graphite.

Engel, Elnathan et al. (2010) developed arrays of silicon nanowire field-effect transistors doped with (3-aminopropyl)triethoxysilane (APTES) to detect 2,4,6-trinitrotoluene (TNT) in air and in liquid. By measuring the change in conductance of the nanowires as TNT bound to the amine groups in APTES the team was able to detect sub-fM concentrations of TNT.

Xu, Lu et al. (2010) deposited a 20 nm film of silver nanoparticles on a flexible microstructured polymer surface, mimicking the hierarchical micro/nano structure of a lotus leaf. The biomimetic surface exhibited superhydrophobicity with a contact angle of 166° (polytetrafluoroethylene (PTFE, marketed as Teflon™) has a contact angle ≈ 100°) with applications in self-cleaning and anti-fog surfaces (Yasuda, Okuno et al. 1994).

Haruta, Kobayashi et al. (1987) reported novel low temperature catalysts of carbon monoxide by depositing nanoparticles of gold, a noble metal inert when in bulk, on metal oxides. This size dependent catalytic effect was attributed to quantisation effects in the electronic structure of small clusters below 2 nm (Valden, Lai et al. 1998, Haruta 2003).

These examples demonstrate the wide range of application areas harnessing enhanced surface area to volume ratios in nanomaterials. Novel optical properties are now considered.

1.1.2 Optical properties

The interaction of electromagnetic waves with matter encompasses a number of physical phenomenon including absorption, (re-)emission, reflection and refraction which depend on the size of the material in addition to its electronic structure.

In bulk crystalline semiconductors the repeated overlap of constituent atomic orbitals results in the formation of continuous allowed energy levels forming bands (Weller 1993). In a typical semiconductor the valence (occupied) and conduction (unoccupied) bands will be separated by an energy gap. On absorption of a photon of equal or greater energy than this gap, an electron from the valence band can be excited to the conduction band, resulting in an electron-hole pair (an exciton) with a characteristic exciton radius. As the size of a (nanostructured) semiconductor falls below the exciton radius, a discretisation of energy levels occurs (Figure 1.3A). These quantised energy levels result in discrete absorption peaks (Figure 1.3B), and can be fine-tuned by controlling the size of the semiconductor nanostructures, often referred to as “quantum dots”.

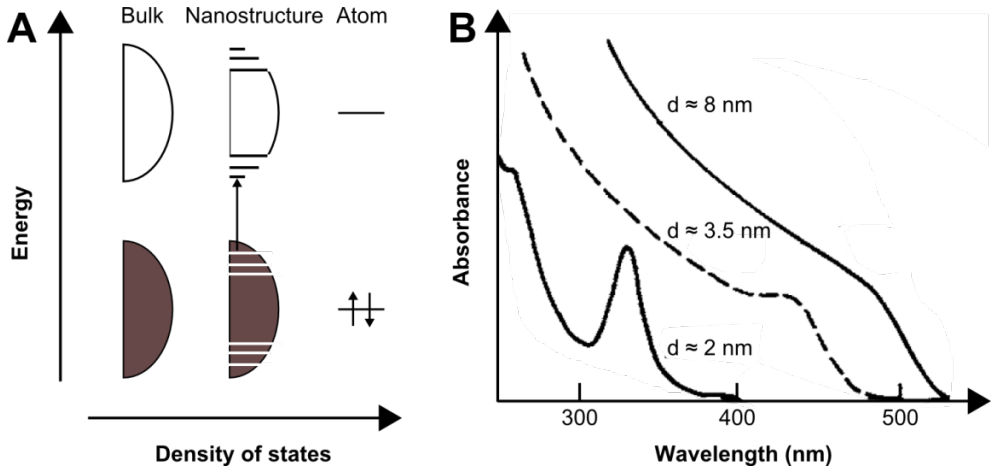

Figure 1.3 Quantisation effects in semiconductor nanostructures. **(A)** Illustration of electronic structure for a bulk, nanostructured and atomic semiconductor (adapted from Alivisatos (1996)). **(B)** Absorption spectra for cadmium sulphide (CdS) quantum dots of different diameters (adapted from Weller (1993)). A discrete absorption peak can be seen as the diameter of the nanostructure approaches 2 nm.

Semiconductor nanostructures have found applications in many areas such as light emitting devices (LEDs), photovoltaics and fluorescent labelling (Rogach 2011).

Sunscreens consisting of fine particles (≈0.2 μm) of titanium dioxide and zinc oxide (ZnO) have been manufactured for a number of decades due to their absorption and scattering of UV light (Sayre and Kollias 1990). However, visible light scattering produces aesthetically displeasing white solutions when sunscreen is applied to the skin, and results in limited consumer uptake. Reducing particle size below 100 nm reduces scattering in the visible light range, and enhances absorption and scattering in the UV-A and UV-B ranges (Dransfield 2000, Popov, Priezzhev et al. 2005). These aesthetically acceptable transparent sunscreens are widely available today and accounted for 1000 tons of nanoparticle manufacture in 2003/04 (Borm, Robbins et al. 2006).

Colvin, Schlamp et al. (1994) fabricated LEDs by combining a semiconducting polymer with a layer of cadmium selenide (CdSe) nanocrystals. They reported voltage tuning of colour, with the possibility of further colour tuning by varying the nanocrystal diameters.

Chanyawadee, Harley et al. (2009) reported a sixfold enhancement in photocurrent conversion efficiency for photovoltaics incorporating CdSe/CdS quantum dots.

Gao, Cui et al. (2004) synthesised CdSe core-zinc sulphide shell quantum dots capped with tri-*n*-octylphosphine oxide, a block co-polymer, and polyethylene glycol (PEG) for stabilisation in biological environments. By attaching targeting ligands to these probes they were able to image and localise human prostate cancer tumours in mice. Without appropriate capping quantum dots can exhibit toxic effects to bacterial and human cells due to the poisonous nature of cadmium salts (Flick, Kraybill et al. 1971, Hossain and Mukherjee 2013).

Gharghi, Gladden et al. (2011) demonstrated a visible light range “invisibility cloak” for a 6 μm wide-300nm high “bump” using nanoporous silicon oxide with exceptionally low refractive index ($n < 1.25$) coupled to a silicon nitride waveguide.

In addition to semiconductor nanostructures, metal nanostructures exhibit unique optical properties due to localised surface plasmon resonance (LSPR) (Hutter and Fendler 2004, Garcia 2011). Incident electromagnetic radiation excites the collective oscillations of conduction electrons in a metal known as surface plasmons, resulting in polarization, displacement and a resultant restoring force between the electrons and the nanostructure nuclei (Figure 1.4A). When the wavelength of incident radiation equals the plasmon resonance wavelength, strong characteristic absorbance peaks arise (Figure 1.4B).

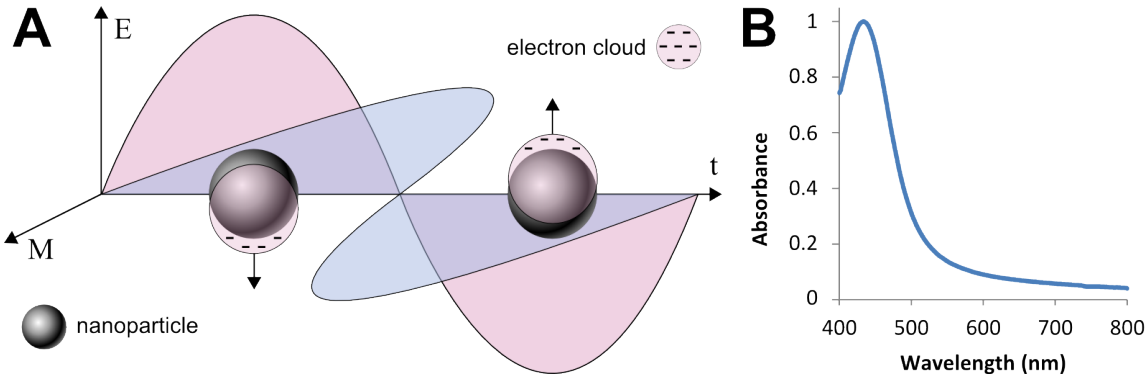

Figure 1.4 (A) Illustration of localised surface plasmon resonance (LSPR) in a metallic nanoparticle (adapted from Kelly, Coronado et al. (2003)). The electric field component of incident light polarises the conductive electron cloud of the nanoparticles, leading to strong absorbance peaks at the plasmon resonance wavelength. **(B)** Absorption spectra for 20 nm silver nanoparticles, displaying a characteristic absorbance around 420 nm.

The plasmon resonance wavelength depends strongly on the size, shape and material of the nanostructure, in addition to the surrounding medium (Link and El-Sayed 2000). This sensitivity has been widely exploited in sensing and plasmonics.

Englebienne (1998) coated gold nanoparticles with monoclonal anti-human chorionic gonadotropin (hCG) antibodies and detected LSPR shifts when nanograms of hCG, naturally produced by cancerous tumours, were introduced to nanoparticle solutions. These shifts were attributed to a change in the refractive index at the nanoparticle surfaces upon ligand binding.

Haes and Van Duyne (2002) developed a nanoscale biosensor based on arrays of biotin-functionalised triangular silver nanoparticles. Streptavidin binding resulted in a 27 nm LSPR shift for concentrations down to the low-picomolar/high-femtomolar region.

Raschke, Kowarik et al. (2003) similarly functionalised gold nanoparticles with biotinylated bovine serum albumin (BSA) and detected LSPR shifts from single nanoparticles when streptavidin was introduced.

Pillai, Catchpole et al. (2007) reported a 16-fold enhancement in the absorption of 1050 nm light from silicon solar cells and a 12-fold enhancement in electroluminescence in silicon based LEDs after the addition of a layer of silver nanoparticles, acting as light traps. The large optical cross-section of the silver nanoparticles due to LSPR increased the scattering of longer wavelengths of light into the devices.

In addition to the novel surface area-related and optical properties of nanomaterials, some novel mechanical properties of nanomaterials are described.

1.1.3 Mechanical properties

The mechanical properties of both naturally occurring and engineered nanomaterials have been explored intensively. For example, multi-walled carbon nanotubes, first intentionally synthesised in 1991, possess a Young's modulus and tensile strength of 950 GPa and 63 GPa respectively, 5 and 120 times greater than steel (Iijima 1991, Yu, Lourie et al. 2000, Patnaik and Hopkins 2004). These extraordinary properties have resulted in a number of applications including polymer nanocomposite materials, gigahertz oscillators, mechanical resonators for force detection and nanoinjectors (Zheng and Jiang 2002, Coleman, Khan et al. 2006, Chen, Kis et al. 2007, Moser, Guttinger et al. 2013).

The mechanical performance of bone is now understood to be a result of the structured arrangement of mineral nanoparticles within collagen fibrils, paving the way for engineering artificial substitutes for treatment (Fratzl, Gupta et al. 2004, Zhu, Xiao et al. 2009). Similarly, the remarkable strength of silk fibres is now known to be due to the arrangement of nanoscale protein crystals embedded in a polymer network (Gosline, Guerette et al. 1999). This design has been replicated synthetically to create strong and highly elastic nanocomposites (Liff, Kumar et al. 2007). Tsuji, Ueji et al. (2002) reported that nanostructured steel possessed improved strength and ductility compared to traditionally produced steel due to the nanoscaled grain size.

Electrospinning biodegradable fabrics with variable nanopore size holds promise for artificial tissue scaffolding, where implanted cells are able to adhere and grow in a wound site (Keun Kwon, Kidoaki et al. 2005).

The climbing ability of geckos is a result of the ≈500,000 hairs or setae on each foot, each containing hundreds of nanosized spatulae (Autumn, Liang et al. 2000). The sum van der Waals interactions between the spatulae and a surface result in ≈10 N of adhesive force per foot, more than sufficient to stick the ≈100 g creatures to a surface. Efforts to recreate this adhesive ability synthetically using carbon nanotubes as spatulae have been successfully reported (Yurdumakan, Raravikar et al. 2005, Ge, Sethi et al. 2007).

These remarkable combined properties of nanomaterials have understandably led to a rapid increase in their study, manufacture and use. As their properties depend heavily on size, shape and composition the ability to accurately characterise nanomaterials has been crucial to their widespread adoption and use.

1.2 Nanomaterial characterisation techniques

The fundamental challenge in characterising nanomaterials is their size: optical microscopy is diffraction limited to roughly 200 nm and sample preparation techniques for alternative microscopies are often complex and distinct from the environments nanomaterials are used in (Heintzmann and Ficz 2006). Modern optical techniques which overcome the diffraction limit such as stimulated emission depletion microscopy (STED), photo-activated localisation microscopy (PALM) and stochastic optical reconstruction microscopy (STORM) require fluorescently labelled specimens and are not suitable for imaging inorganic materials (Hell and Wichmann 1994, Betzig, Patterson et al. 2006, Rust, Bates et al. 2006). Given the importance of characterisation techniques and their use in this thesis, a broad overview of those available and used is now given.

1.2.1 Electron microscopy

Electron microscopy can be broadly grouped into transmission and scanning electron microscopy (TEM/SEM), which both utilise electrons for image formation instead of photons, allowing the characterisation of nanomaterials below the optical diffraction limit.

Ernst Ruska built the first transmission electron microscope in 1931 with a magnification of 16x following the earlier work of J.J. Thomson, Louis de Broglie and G.P. Thomson on “cathode rays” (electron beams) and electron diffraction (Knoll and Ruska 1932, Haguenau, Hawkes et al. 2003). Briefly, an electron source generates high voltage electrons which are condensed, focussed and transmitted through a sample held in a vacuum. Samples must be electron transparent (typically less than a 100 nm thick) and able to withstand the vacuum environment (Kohl and Reimer 2008). The resulting diffraction and image planes can be focussed and projected onto a fluorescent screen or

camera (Figure 1.5A). As electron wavelength λ relates directly to energy $E = \frac{hc}{\lambda}$ ($h =$ Planck's constant, $c =$speed of light), in theory arbitrarily high-resolution images could be obtained by increasing electron energy (voltage) sufficiently. In practise resolution is limited by aberrations in electron optics, limited brightness in electron sources and higher energies causing radiation damage to biological specimens in particular although state-of-the-art high-resolution TEM (HRTEM) has achieved sub-atomic resolution below 0.05 nm (Kisielowski, Freitag et al. 2008, Kohl and Reimer 2008, Segal 2009). Other advanced techniques such as high-angle annular dark field scanning transmission electron microscopy (HAADF STEM) have been used to characterise inorganic nanomaterials at atomic resolution, in three dimensions (Gontard, Dunin-Borkowski et al. 2009).

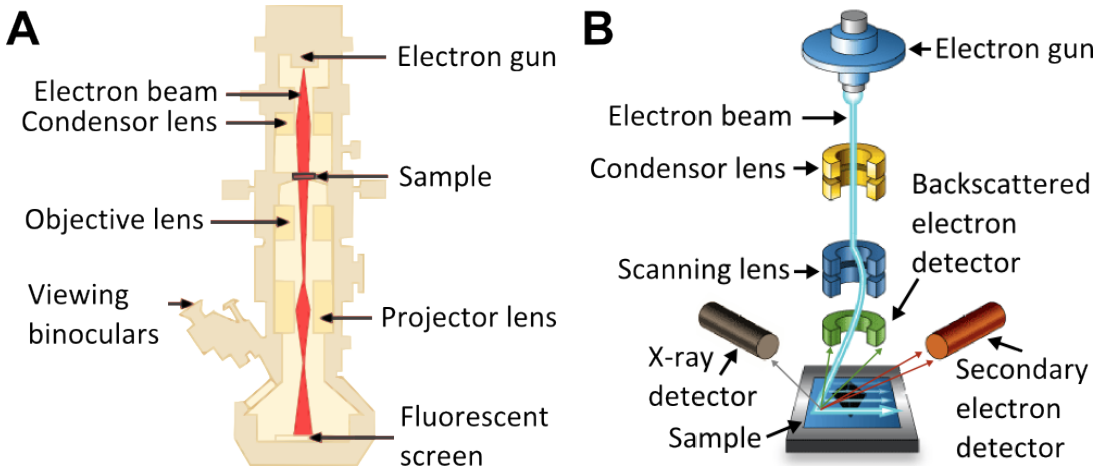

Figure 1.5 Schematic of **(A)** a transmission electron microscope, adapted from Dundee (2007) and **(B)** a scanning electron microscope, adapted from AMMRF (2013).

Scanning electron microscopy was invented in 1938 by Manfred von Ardenne and first commercially available in 1965 from the Cambridge Instrument Company (Haguenau, Hawkes et al. 2003). An electron beam is focussed onto a discrete spot or pixel on the sample and raster scanned under vacuum; at each pixel secondary (inelastically scattered) electrons, backscattered (elastically scattered) electrons and characteristic x-rays emitted from the sample can be detected and reconstructed to form a topographic (secondary electrons), compositional (back-scattered) or spectroscopic (energy dispersive

x-rays (EDX)) image (Figure 1.5B). Samples must be conducting to prevent surface charge build-up and robust under vacuum. High resolution SEM has recently achieved 0.8 nm resolution (de Andrade Rosa, de Souza et al. 2013).

TEM and SEM are primarily suited to inorganic materials; imaging low atomic number and water-rich organic materials requires substantial sample preparation. TEM sample preparation for organic and biological matter is particularly complex as final samples must be thin (≈100 nm) for imaging. Chemical fixation, dehydration, embedding and ultra-thin sectioning are common strategies for TEM, as well as cryogenic preparation and imaging (Fernández-Morán 1952, Palade 1952, Williams 1953, Adrian, Dubochet et al. 1984). Contrast in low atomic number samples can be enhanced through staining or immunolabelling (Singer 1959, Bernhard 1969).

Chemical fixation and dehydration (or cyrofixation), as well as coating with a thin conductive layer are established techniques for SEM sample preparation (Schatten 2013). Variable pressure environmental SEM (ESEM) was recently developed to allow samples to be imaged in a low pressure (100s of Pa, c.f. atmospheric pressure is in the order of 100 kPa) environment that can sustain hydrated samples without requiring coating (Danilatos 1994, Stokes 2008).

Considerable progresses in electron microscopy and sample preparation have ensured its place in the nanotechnologist's toolkit, though probing biological matter in particular remains challenging, and impossible for live cells.

1.2.2 Scanning probe microscopy

Binnig, Rohrer et al. (1982) first demonstrated controlled quantum tunnelling under moderate vacuum at room temperature between a tungsten tip and a platinum plate. Attaching piezoelectric elements to the tip and plate they were able to control the

distance between them with angstrom resolution. By applying a constant voltage between tip and plate and varying the tip-plate distance, they confirmed an exponential relationship between tunnelling gap and current. In 1982 they extended this setup to involve raster scanning, at constant tunnelling voltage and current, surfaces of $CaIrSn_4$ and Au. As the tunnelling current varied as a function of tip-surface distance and surface work function, feedback electronics altered the Z piezoelectric component to maintain a constant current. Calibrating the relationship between Z voltage and tip distance it was possible to map the topography of the surfaces with atomic resolution (Binnig, Rohrer et al. 1982). A schematic of a scanning tunnelling microscope (STM) is shown in Figure 1.6A.

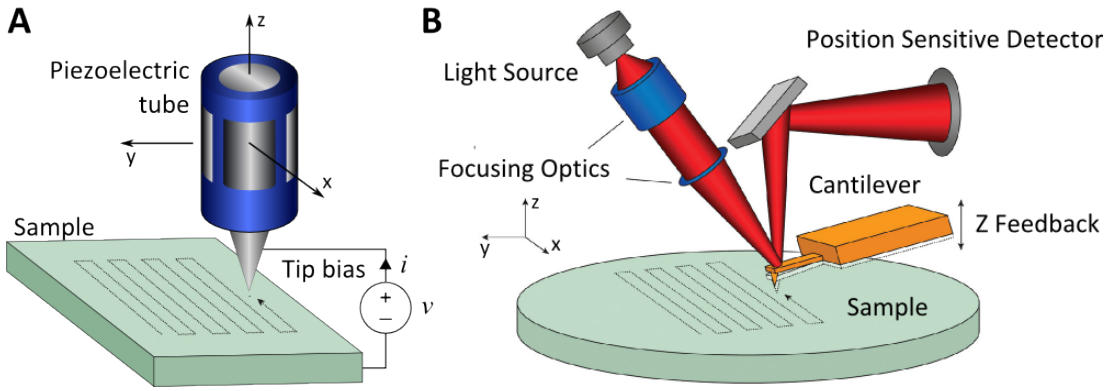

Figure 1.6 Illustration of **(A)** a scanning tunnelling microscope and **(B)** an atomic force microscope using the beam deflection method, adapted from Geisse (2009). A laser is focused onto the reflective cantilever probe and detected by a four-quadrant photodiode, allowing both vertical and lateral motion to be tracked with high sensitivity.

Subsequent advances have allowed imaging in air and liquid, though the sample must be conducting for tunnelling to occur (Morita, Otsuka et al. 1988). Eigler and Schweizer (1990) successfully used STM to not only image individual atoms, but also manipulate their positions to design a structure atom by atom (the logo of their employer, IBM).

Four years after the invention of the STM, Binnig, Quate et al. (1986) developed an alteration to the microscope for imaging non-conducting surfaces. They added a gold foil cantilever with a sharp diamond tip between the STM tip and a ceramic surface. As the surface approached the cantilever and diamond tip, the tip-surface interaction forces

deflected the cantilever, altering the tunnelling current between the STM tip and cantilever surface. Running the STM in constant current mode resulted in a constant force being applied between the diamond tip and surface as it was scanned, allowing the resultant Z piezoelectric response to be mapped to the height of the non-conducting sample. A simpler optical method for measuring the deflection of the cantilever was proposed by Meyer and Amer (1988), and is a common detection mechanism in commercial AFMs (Figure 1.6B). Further detail on different imaging modes is presented in the next chapter. In addition to imaging, AFMs can be operated in force spectroscopy mode for nanomechanical assays, where quantitative mechanical properties of samples can be obtained through analysis of tip-sample interaction forces as a function of tip-sample distance and indentation speed (Butt, Cappella et al. 2005).

The AFM resulted in a plethora of scanning probe microscopes (SPM) such as magnetic force microscopy, kelvin probe microscopy and chemical force microscopy which work on a similar basis: a probe/sample interaction, a detection mechanism, raster scanning and feedback for image formation (Rugar, Mamin et al. 1990, Nonnenmacher, O'Boyle et al. 1991, McKendry, Theoclitou et al. 1998, Gerber and Lang 2006). Recent developments in high-speed AFM have overcome the challenges of slow scan speeds through substantial improvements in cantilever, scanner and feedback design (Ando, Kodera et al. 2001, Humphris, Miles et al. 2005, Fantner, Schitter et al. 2006).

The ability to image and manipulate samples without the stringent sample preparation needs or vacuum environments of TEM/SEM have proven fundamental to the progression of nanotechnology – both in terms of understanding nanomaterials and their interactions with living matter in particular.

1.2.3 Other characterisation techniques

In addition to the EM and SPM techniques described above, there are a number of additional techniques for probing the properties of nanomaterials.

Dynamic light scattering **(DLS)** uses a monochromatic coherent light source to track the time-dependent scattering fluctuations of solutions of small particles. The fluctuations can be correlated to the particles Brownian motion and, via the Stokes-Einstein relation, their hydrodynamic size (Pecora 1985). If an external electric field is applied to the solution, the electrophoretic mobility of the particles can be measured and related to their zeta potential (magnitude of electric charge at the interface of the particle and liquid) (Murdock, Braydich-Stolle et al. 2008). Estimating nanoparticle radii in liquid using DLS provides complementary information to EM measurements, which are conducted in vacuum/air.

Another optical technique for readily characterising the absorption and scattering of nanomaterials in liquid is UV-Visible **(UV-Vis)** spectroscopy. A broad-spectrum light source, such as a tungsten halogen bulb, is used with a monochromator to produce a beam of light of specific wavelength. The sample of interest is placed in a standardised cuvette made out of quartz or plastic, and placed in the path of the monochromated light. The light transmitted through the sample is measured as the ratio of intensity of light before (I_0) and after the sample (I_1):

$$\begin{aligned} \text{Transmittance} &= \frac{I_1}{I_0}, \\ \text{Absorbance} &= -\log_{10}(\text{Transmittance}) \end{aligned} \tag{1.1}$$

with absorbance defined as per eq. (1.1). Absorbance is unitless, though often quoted in the literature with A.U. (absorbance units) or O.D. (optical density), and is a measure of light that has been absorbed and/or scattered by the sample. Where the sole mechanism

of interaction is absorption, the absorbance can be related to concentration and molar absorptivity of the sample with the Beer-Lambert relation:

$$A = \epsilon l c \tag{1.2}$$

where A = absorbance, ϵ = molar absorptivity ($M^{-1}cm^{-1}$), l = path length of cuvette (cm) and c = concentration of the sample (M = mol dm^{-3}) (Schmidt 2005). Measuring the absorbance as a function of wavelength produces an absorbance spectra for the material (Figure 1.7).

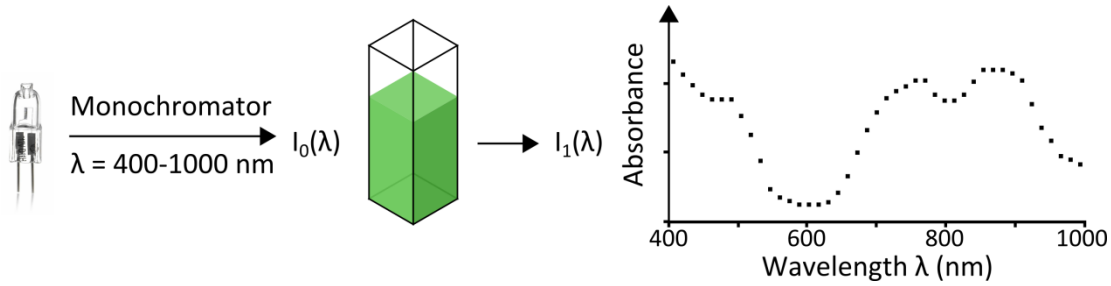

Figure 1.7 Recording absorbance spectra by measuring absorbance as a function of wavelength with UV-Vis spectroscopy.

Other material characterisation techniques include x-ray diffraction **(XRD)** and small-angle x-ray scattering **(SAXS)** for determining nanostructure crystallinity, size and shape, elemental analysis using inductively coupled plasma atomic emission spectroscopy **(ICP-AES)** and surface analysis via x-ray photon spectroscopy **(XPS)** and Auger electron spectroscopy **(AES)** (Glatter and Kratky 1982, Thompson and Walsh 1989, Watts and Wolstenholme 2003, Pecharsky and Zavalij 2009).

No single technique is sufficient to characterise a nanomaterial; the appropriate choices will depend on the initial and final states of the nanomaterial (e.g. a powdered nanostructure dispersed in an inorganic solution for application on a surface, or an aqueous solution of nanomaterials intended for waste water filtration) as well as the resources available to the nanotechnologist. For example, HRTEM is a research discipline in its own right compared to commercially available traditional (lower resolution) TEM.

Having explored the properties of nanomaterials and how they can be characterised, their interactions with living matter are now explored.

1.3 Nanotechnology and living matter

Biology functions at the nanoscale: DNA, proteins and cell membranes are all structured on the nanoscale, and nature has already developed remarkable nano-sized molecular machinery (Vallee and Hook 2003). There are two aspects to examine when considering nanotechnology applied to biology and medicine: intended interactions (e.g. “nanomedicine”) and unintended interactions (requiring “nanotoxicology”).

1.3.1 Nanomedicine

The application of nanotechnology to medicine is an exciting field that has made rapid progress over the last decade in the diagnosis and treatment of disease, primarily through the possibility of designing multi-functional contrast agents and therapeutics that target specific moieties, avoiding unnecessary systemic side-effects (Ferrari 2005, Vogel 2008).

1.3.1.1 Diagnostics

Magnetic resonance imaging (MRI) is a widely used non-invasive technique to image internal tissue structures, by measuring the radio frequency (RF) response of magnetised nuclei inside a patient exposed to an external alternating magnetic field (Mitchell and Cohen 2004). Contrast mechanics in MRI are complex, and can be enhanced by the injection of contrast agents such as gadolinium or iron oxide particles which enhance the RF relaxation times of adjacent protons (Mitchell and Cohen 2004). These contrast agents are non-specific – they increase contrast throughout the body. Huh, Jun et al. (2005) overcame this limitation by functionalising 9 nm diameter water-stabilised iron oxide nanoparticles with the cancer-targeting antibody Herceptin (trastuzumab). Five minutes

after injection into mice with implanted tumours, MRI contrast was significantly and selectively enhanced in the tumorous regions compared to controls. Similarly, Sun, Du et al. (2010) functionalised 10 nm diameter iron oxide nanoparticles with PEG allowing the modular addition of targeting ligands. They attached chlorotoxin, a tumour targeting peptide to the particles and observed substantial MRI imaging contrast around tumours in mice after injection.

In addition to enhanced MRI imaging, nanomedicine has been applied to a number of clinical laboratory tests. Elghanian (1997) developed a colorimetric system able to detect 10 fM of a specific 30 base single-stranded DNA molecule. Gold nanoparticles were functionalised with carefully designed mercapto-alkyl-oligonucleotides chosen to hybridise the target DNA molecules. In the absence of targets the gold nanoparticles appeared red due to the characteristic LSPR of gold at 520 nm. In the presence of targets, hybridisation between multiple nanoparticles and target molecules resulted in nanoparticle clusters. These clusters appeared blue due to a shift in LSPR caused by coupling between nanoparticles in the clusters (Dusemund, Hoffmann et al. 1991).

Wu, Datar et al. (2001) developed a cantilever-based sensor for prostate-specific antigens (PSA) in human serum albumin. By functionalising a cantilever surface with polyclonal anti-PSA antibody, they were able to detect 0.2 ng/ml concentrations of PSA as the antigens bound to their antibodies, causing a measurable deflection of the cantilever. This is close to the clinical detection requirement for prostate cancer.

Zheng, Patolsky et al. (2005) successfully reported the detection of 0.9 pg/ml concentrations of PSA in undiluted serum using arrays of silicon nanowires. Similarly to the previous work cited for detecting TNT, the nanowires were coated with marker

recognition antigens, which altered the conductance of the arrays when the markers bound.

As well as improving diagnosis techniques, nanomedicine has generated many potential new treatments.

1.3.1.2 Treatment

Numerous nanomedicine treatments have been reported in the literature, with a recent search of the US clinical trials database revealing 184 studies completed or underway (NIH 2013).

Gobin, O'Neal et al. (2005) developed an improved solder paste for heat-induced laser tissue welding by tuning the absorption of silica-core gold-shell nanoparticles to the near-infrared (NIR) region. Water and haemoglobin have the lowest absorption in the NIR window, allowing deeper penetration through tissue than visible light (Weissleder 2001). The nanoshells were a million-fold more effective as absorbers than indocyanine green, the traditional ingredient in tissue solder paste, as well as more stable and larger so less diffusive, limiting damage to surrounding tissue.

Johannsen, Gneveckow et al. (2005) locally injected a human patient presenting prostate cancer with 15 nm diameter aminosilane coated iron oxide nanoparticles. By externally applying a 100 kHz alternating magnetic field, they were able to increase the tumour temperature by up to 10°C due to inductive heating losses from the nanoparticles.

Dickerson, Dreaden et al. (2008) injected PEG coated gold nanorods into mice with squamous cell carcinoma (skin cancer). The LSPR absorption of the nanorods peaked at 800 nm. By exposing the tumours to NIR excitation, they observed a 10-20°C heating effect compared to controls without nanorods, inducing hyperthermia in the cancerous cells in a minimally-invasive way.

Peiris, Bauer et al. (2012) developed multi-component nanoparticles for targeted drug delivery comprising of a chain of three iron oxide nanoparticles conjugated to a liposome containing the anti-cancer drug doxorubicin. 24-hours after injection into breast tumour bearing mice, a local RF field was applied to the tumour site. The induced vibration of the magnetic nanoparticles ruptured the conjugated liposome, releasing its payload at the site of RF stimulation. This resulted in strong anti-cancer effects without unwanted side-effects due to the localised distribution of the drug.

Taratula, Kuzmov et al. (2013) developed multi-functional lipid-based nanostructures containing the anti-cancer drugs doxorubicin or paclitaxel as a payload, with a targeting receptor for lung cancer cells and small interfering RNA (siRNA) to reduce the amount of drug pumped out by the cancerous cells. After inhalation of the nanostructures by mice, the nanostructures delivered the drug at the tumour site, reducing side-effects to healthy tissue.

The beneficial application of nanomaterials with living matter such as those described constitutes a large and growing body of activity. The study of harmful interactions of nanomaterials with the environment and living matter within is now discussed.

1.3.2 **Nanotoxicology**

At the start of 2014 the internet-based Project of Emerging Nanotechnologies Consumer Products Inventory listed over 1600 commercially available products advertising “nano” properties (Nanotechnologies 2014). When these products reach their end-of-life, their disposal will ultimately result in exposure to the environment. Many questions remain as to how such materials affect workers at high doses, users at intended doses, and the wider environment upon disposal.

The study of the harmful interactions of nanomaterials with living matter has had a confusing history. Donaldson, Stone et al. (2004) first coined the phrase "nanotoxicology" for the toxicological study of nanomaterials "*where there is the potential for substantial human exposure*", whereas Oberdorster, Oberdorster et al. (2005) defined nanotoxicology as the "*science of engineered nanodevices and nanostructures that deals with their effects in living organisms*". The confusion arises from the different focuses of nanotoxicology; one is concerned with the harmful impact on human health while the other with the effects (harmful or otherwise) on the *wider* environment, not limited to humans.

This thesis adopts the latter, broader, definition of nanotoxicology: if a nanomaterial is found to have no negative impact on human health, it could be a candidate for drug delivery. Conversely a toxic nanomaterial could be a candidate for e.g. targeted cancer therapy (Soenen, Demeester et al. 2013). In both cases there is a fundamental need to understand the basics of nanoparticle-cell interactions for viruses, bacteria, plant, animal and human cells.

The majority of nanotoxicology research to date has focussed on the toxicity of nanomaterials to humans, via animal models (Fischer and Chan 2007, Fadeel and Garcia-Bennett 2010, Krug and Wick 2011). Only relatively recently has the field extended to include fish, daphnia and other environmentally critical organisms such as bacteria (Farkas, Christian et al. 2011, Arora, Rajwade et al. 2012, Poynton, Lazorchak et al. 2012, Suresh, Pelletier et al. 2013).

1.4 Motivations for the thesis

Nanotechnology is a rapidly advancing field of research with direct application to human biology through nanomedicine, and indirect application to humans, animals, plants, fungi

and bacteria through the environmental exposure of nanotechnology-containing products. Our understanding of the potentially harmful consequences of nanomaterials with humans and other organisms is growing, but there is yet to exist a standard methodology for studying the interaction of cells with nanoparticles (Hunt, Lynch et al. 2013). This thesis seeks to overcome this oversight through the development of a standard methodology to study the interactions of nanoparticles with cells in a cell- and nanomaterial-agnostic way.

1.5 Overview of the thesis

- Chapter 2 contains the general materials and methods used in this thesis.
- Chapter 3 characterises the stability of four silver-based nanoparticles in colloidal dispersions.
- Chapter 4 presents a standard methodology to study the interaction of nanoparticles with cells, applied to the model bacterium *Escherichia coli (E. coli)*.
- Chapter 5 applies the methodology to determine the interaction of silver nanoparticles with *E. coli*.
- Chapter 6 presents the results of a collaborative effort to study the mechanical properties of live *E. coli* and human red blood cells using multi-harmonic AFM, as an extension to the methodology presented in Chapter 4.
- Chapter 7 summarises the findings in this thesis, draws overall conclusions and sets out future directions for the research generated.

Chapter 2

Materials and Methods

This chapter describes the overall materials and methods used in this thesis. Novel methods and sample preparation techniques developed for this thesis can be found in the relevant results chapters.

2.1 Introduction

Nanotechnology and nanotoxicology are inherently multi-disciplinary fields requiring knowledge of chemistry, materials science, physics, engineering, biology and medicine. A number of techniques from different disciplines were used in this thesis and are briefly described here.

2.2 Laboratory materials

All materials were purchased from Fisher Scientific (Leicestershire, UK) unless otherwise specified. Double distilled water (ddH_20, Millipore, Hertfordshire, UK) with a specific resistivity of 18 MΩcm was used to make up all solutions. Muscovite mica was purchased from SPI Supplies (West Chester, PA, USA).

2.3 Cell biology

E. coli DH5α and human red blood cells (RBC) served as model cells in this thesis for nanotoxicology assays and technique development. DH5α is a well-studied and common laboratory strain of *E. coli* that is readily available to researchers (Grant, Jessee et al. 1990, Neidhardt 1996). Human RBC were chosen due to their ease of harvesting.

2.3.1 **Human RBC**

Human RBC were harvested from group members' fingertips using sterile lancets (Becton Dickinson, Oxfordshire, UK), diluted in 1x phosphate buffer saline (PBS) and used immediately.

2.3.2 ***E. coli***

2.3.2.1 **Culture and growth curves**

E. coli DH5α were grown in Luria-Bertani (LB) medium at 37°C shaking at 152 rpm (Minitron incubator, Infors HT, Surrey, UK), and on LB-Agar plates at 37°C (Heraeus incubator, Thermo Scientific, Hampshire, UK).

The growth of *E. coli* cultures over time was measured by UV-Vis spectroscopy. This simple, reproducible, technique allowed the measurement of the effects of agents (nanoparticles or drugs) on cell growth (Figure 2.1, Protocol 2.1).

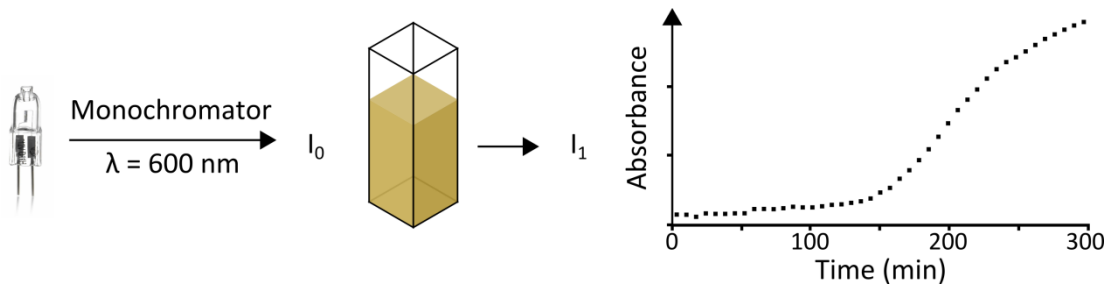

Figure 2.1 Diagram illustrating time-varying UV-Vis spectroscopy used to measure bacterial culture growth. The optical absorbance of 1 ml samples of culture at 600 nm was recorded as a function of time.

Protocol 2.1 – Bacterial growth curve

1. Calibrate the UV-Vis spectrophotometer (UV-Mini 1240, Shimadzu, Japan) at 600 nm with 1 ml of fresh LB.
2. Inoculate a conical flask with 45 ml autoclaved LB with 45 µl of saturated overnight *E. coli* culture.

3. Measure the 600 nm wavelength absorbance of a 1 ml sample of the new culture as time point $t = 0$ minutes, before placing the flask to incubate at 37°C shaking at 152 rpm.
4. Every 30 minutes, measure the absorbance of a new 1 ml sample taken from the culture.
5. When the absorbance of the culture reaches 0.2 (arbitrary absorbance units), rapidly split 20 ml of the culture, under sterile conditions, into a control flask and a flask for testing.
6. Add any agent to the required concentration to the testing flask, and an equal volume of ddH_20 to the control flask. Prepare an additional 1 ml cuvette with the agent added to LB at the same final concentration for calibration.
7. Measure the absorbance of 1 ml samples of each flask using their respective calibrations and place both flasks in the incubator.
8. Every 20 minutes, measure the absorbance of new 1 ml samples taken from both flasks using their respective calibrations.
9. The process continues until no significant changes in absorbance are observed.

This protocol allows for at least 20 time points, or 400 minutes of growth. If longer time is needed, measurements can be made at larger time intervals. Steps 4-8 must be completed in the minimal time possible and under sterile conditions to reduce fluctuations incurred by the drop in temperature of the surroundings. The protocol should be prepared in triplicate, and repeated on at least two separate days.

Once growth curves were obtained, arbitrary absorbance units were converted to number of viable cells (colony forming units) per millilitre as follows.

2.3.2.2 Colony forming unit (CFU) counts

Quantifications of the number concentration of live (colony forming) bacteria in culture for arbitrary absorbances were made by serial dilution and plating overnight. 1 ml samples of culture were drawn, serial-diluted and 50 µl sub-samples were spread in triplicate on LB-Agar plates. CFU were enumerated after overnight incubation at 37°C and (CFU) ml^{-1} was extrapolated as follows:

$$(\text{CFU})\ ml^{-1} = (\text{CFU}) \times 10^{\text{serial}} \times \text{dilution factor}$$

where $\text{serial} = \text{number of serial dilutions, typically 3-4, and } \text{dilution factor} = \frac{1000}{50\mu l}$.

Triplicate plates containing between 2 and 200 individually identifiable colonies were counted and averaged.

By measuring CFU for a range of arbitrary absorbance units, the linear conversion factor of $(1.7 \pm 0.8) \times 10^8$ CFU/ml/absorbance units was obtained for absorbances between 0 and 1 (arbitrary units).

2.3.2.3 Kirby-Bauer disk diffusion assays

Disk diffusion assays are a common method of assessing susceptibility of bacteria to a drug and were carried out according to established protocols (Murray 2007). Briefly, 6 mm diameter filter paper disks (Whatman Grade 2, Fisher Scientific, Leicestershire, UK) were impregnated with the drug or nanoparticle of interest, and placed on LB-Agar plates inoculated with *E. coli* DH5α. After overnight incubation, the zone of inhibition was measured from the diameter of growth inhibition (including the disk) to the nearest 0.1 mm (Figure 2.2).

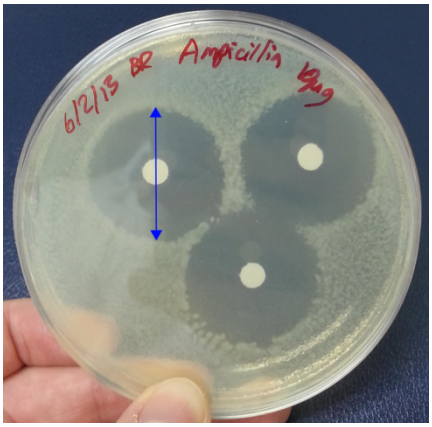

Figure 2.2 Example disk diffusion experiment highlighting (blue arrow) the diameter of growth inhibition around three disks impregnated with the drug ampicillin. Outside of this zone a thick "carpet" of uninhibited bacterial growth can be seen.

2.4 Atomic Force Microscopy (AFM)

The investigation of nanostructures and the morphological effects of their interactions with bacteria were undertaken in Chapters 3, 4 and 5 using a commercial MFP-3D AFM (Asylum Research, Santa Barbara, CA). In Chapter 6 the mechanical properties of bacteria and human RBC were revealed using a novel implementation of multi-harmonic AFM. An overview of the general imaging techniques used is described below.

As described in the introduction, AFM is a type of SPM which consists of four components:

1. A cantilever probe with nanometre sized tip which interacts with the surface of a sample,
2. A three-dimensional system for positioning the probe extremely precisely, for example a piezoelectric XY stage on which the sample resides and a separate piezoelectric Z element attached to the cantilever holder,
3. A probe-surface interaction detection mechanism, for example a laser reflected off the back of the cantilever onto a four-quadrant photodiode, allowing both vertical and horizontal motion of the cantilever to be monitored, and
4. A feedback system to control raster scanning and image formation.

These four elements allow the interaction of the probe and sample to be measured at different XYZ positions. Probe-sample interaction forces include long range electrostatic forces, long range Van der Waals forces, short range contact forces, capillary forces (in air), solvation, hydration, hydrophobic, hydrophilic and double layer forces (in liquid) and surface adhesion (Butt, Cappella et al. 2005, Garcia 2010).

Image formation relies on recording these interactions as the tip is raster scanned across the sample surface, which may be in vacuum, air, liquid and may be conducting or insulating. There are a number of imaging modes available including contact, intermittent contact ("Tapping Mode") and non-contact (not used in this thesis).

2.4.1 **Contact mode**

In contact mode, the probe tip is lowered until repulsive contact forces between the tip and sample result in an initial Z deflection of the cantilever, which is then maintained as a setpoint. A larger deflection setpoint corresponds to a larger applied force and *vice versa*. The sample is raster scanned, resulting in changes to the deflection as the tip interacts with the sample. A feedback loop compensates for these changes in deflection, moving the probe up or down to maintain the setpoint deflection. In the absence of deformation of the sample this change in Z can be correlated to the height of the sample and a topography image is generated. The lateral deflection can also be recorded. The feedback mechanism is often based on a proportional-integral-derivative (PID) controller. The feedback gain, setpoint, scan speed and scan angle are adjusted to obtain a clear image of the topography, deflection and lateral deflection of the probe as it scans the sample. The deflection signal is also referred to as the error signal, as any deviations from the setpoint indicate feedback errors, highlighting edges and indicating that feedback parameters may be sub-optimal. For soft (e.g. biological) samples contact forces may be

excessive and damage the samples. Reducing the setpoint will reduce contact forces at the cost of a losing contact altogether. Reducing scan speed can reduce lateral forces during imaging at the cost of longer image formation.

Imaging samples in liquid removes capillary forces present in air and reduces van der Waals forces between the tip and sample allowing lower imaging forces (Weisenhorn, Hansma et al. 1989). Samples must, however, be well attached to the surface as the tip exerts lateral forces during raster scanning across the surface.

2.4.2 **Tapping mode**

Tapping (or intermittent contact/alternate contact) mode, employs the vibration of the probe by, for example, an additional piezo-element mounted at the base of the probe (acoustic excitation), the application of a varying electric field to the probe in the presence of a fixed magnetic field (Lorentz force excitation) or the application of a varying magnetic field to a magnetically coated probe (Schemmel and Gaub 1999, Buguin, Du Roure et al. 2001). The resulting cantilever motion can be approximated by:

$$z = z_0 + A\cos(\omega t - \varphi) \tag{2.1}$$

where z is the displacement of the cantilever, z_0 the static displacement, A the amplitude, ω the driving angular frequency and φ the phase shift with respect to the driving force. As the oscillating probe is lowered towards the surface the amplitude A changes as a function of both long and short range attractive and repulsive tip-sample interaction forces. In amplitude modulation imaging mode, a setpoint amplitude lower than the free amplitude far from the sample is chosen, and the probe scanned across the sample allowing for image formation via feedback on the amplitude. In addition to height and amplitude, the phase shift φ and lateral motion of the probe can be obtained.

Amplitude modulation AFM has a number of benefits over contact mode including lower forces exerted on the sample due to intermittent interactions between the tip and sample, reduction in shear force as the probe is scanned, and the additional data channels available (Zhong, Inniss et al. 1993).

A point-mass model can be used to approximate the probe motion as follows:

$$m\ddot{z} = -kz - \frac{m\omega_0}{Q}\dot{z} + F_0 \cos \omega t + F_{ts}(d) \tag{2.2}$$

where m is the effective mass of the cantilever, k the cantilever spring constant, $\omega_0 = \sqrt{\frac{k}{m}}$ the resonant frequency, $Q = \frac{m\omega_0}{c}$ the quality factor, c the viscous damping coefficient, F_0 the driving amplitude and $F_{ts}(d)$ the tip-sample interaction forces (Garcia 2010).

For high Q values (corresponding to low viscous damping such as when imaging in air), changes in the phase φ of the cantilever have been shown to correspond to changes in the material properties of the sample through both dissipative and conservative channels (Cleveland 1998, Paulo and García 2001). Such material contrast is useful in identifying features which would otherwise not be revealed in topography.

In liquid the additional hydrodynamic drag experienced by the oscillating probe results in a decrease in its resonance frequency and Q factor, given the higher density of the liquid compared to air. This leads to lower amplitude oscillations and necessitates a change in feedback parameters to accommodate these. Additionally, tuning the cantilevers with acoustic excitation leads to an array of resonance peaks due to the complex interaction between the liquid and holder and the entire length of the cantilever. Heating effects within the sample also affect cantilever dynamics as the sample temperature increases and the deflection drifts, and must be taken into account during imaging.

2.4.3 Lateral resolution

Commercially available AFMs such as the MFP-3D used in this thesis utilise sub-nanometer precision closed-loop piezoelectric actuators to manipulate the sample and/or probe in the XYZ directions. Atomic resolution of periodic structures using AFM has been obtained in vacuum and in liquid by tuning short-range interaction forces to maximise lateral imaging resolution (Giessibl, Hembacher et al. 2000, Voïtchovsky, Kuna et al. 2010). For samples containing isolated features of comparable or smaller radii to an AFM tip however, geometric tip convolution prevents the reliable characterisation of lateral dimensions (e.g. nanoparticle diameters) (Mott, Cotts et al. 2008). The height of raised features under AFM is unaffected by geometric convolution.

2.4.4 Basic image processing

The sample stage used in an atomic force microscope is not nanometrically flat: samples will be systematically tilted (Figure 2.3A). During scanning it is common to correct this in software by applying line-by-line “flattening” which is then saved onto the image, which may introduce “streaky line” artefacts (Figure 2.3B). To correctly compensate for tilt and other imaging artefacts, restoring the saved data to its raw state can be achieved by the “Ultra Restore Layer” function in manufacturer’s software (Igor Pro 6.22A, MFP3D 101010+1901), and allows for more controlled processing.

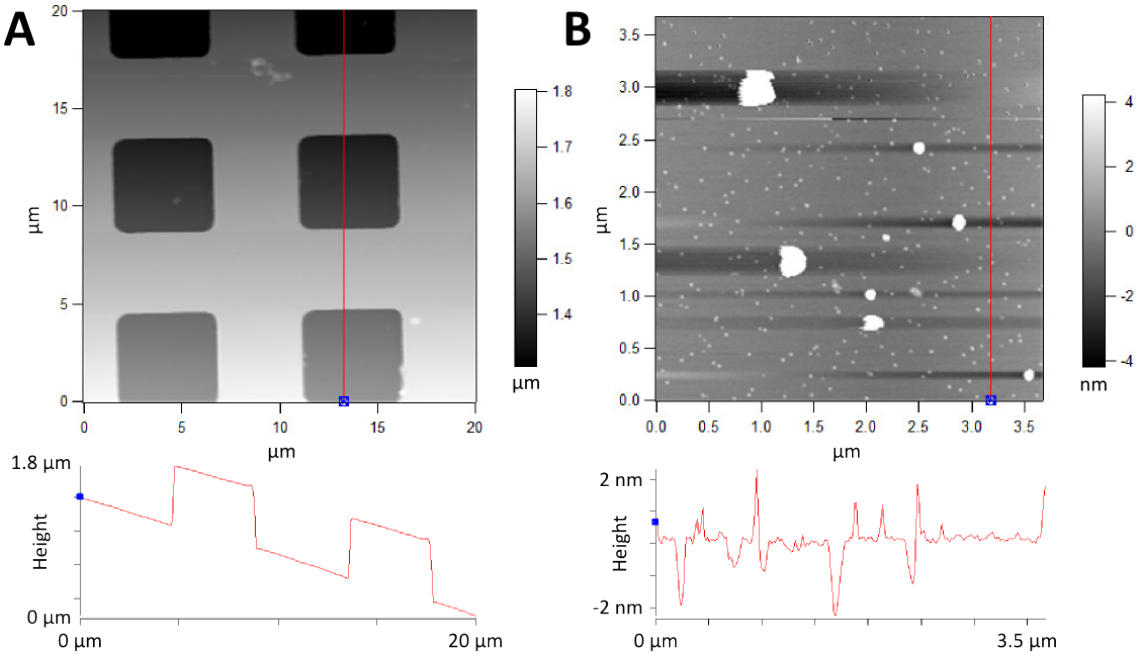

Figure 2.3 AFM **t**opography images with XY cross-sections underneath, showing common artefacts as a result of (**A**) tilt in AFM topography due to experimental setup and (**B**) "streaky lines" caused by line-by-line flattening as the image is scanned then saved.

Raw data can then be corrected either by subtracting a fitted line applied to each line ("flattening") or by subtracting a plane to the whole image ("planefitting"). The following types of fits can be used:

- 0^{th} order fit. This subtracts the average height from the image, and is useful when defining the $z = 0$ plane;
- 1^{st} order fit. This fits a straight line to each line or a 2D plane to the image and subtracts it from the data. This is commonly used to remove systematic tilt.
- 2^{nd}, 3^{rd} order fits. These fit higher order polynomials to the data and subtract, and are not used in this thesis.
- Histogram (flatten only). This line-by-line method compares histograms of lines and applies a 0^{th} order subtraction.
- Magic Mask (flatten only). This performs a 1^{st} order flatten, and calculates an iterative mask of the flattened image, excluding taller objects, and applies a 1^{st} order flatten to the remaining data (the substrate).

Depending on the sample, different modes of planefitting or flattening may be used (Figure 2.4). Ideally, a single 1st order planefit should suffice to remove tilt from the substrate and not introduce further artefacts.

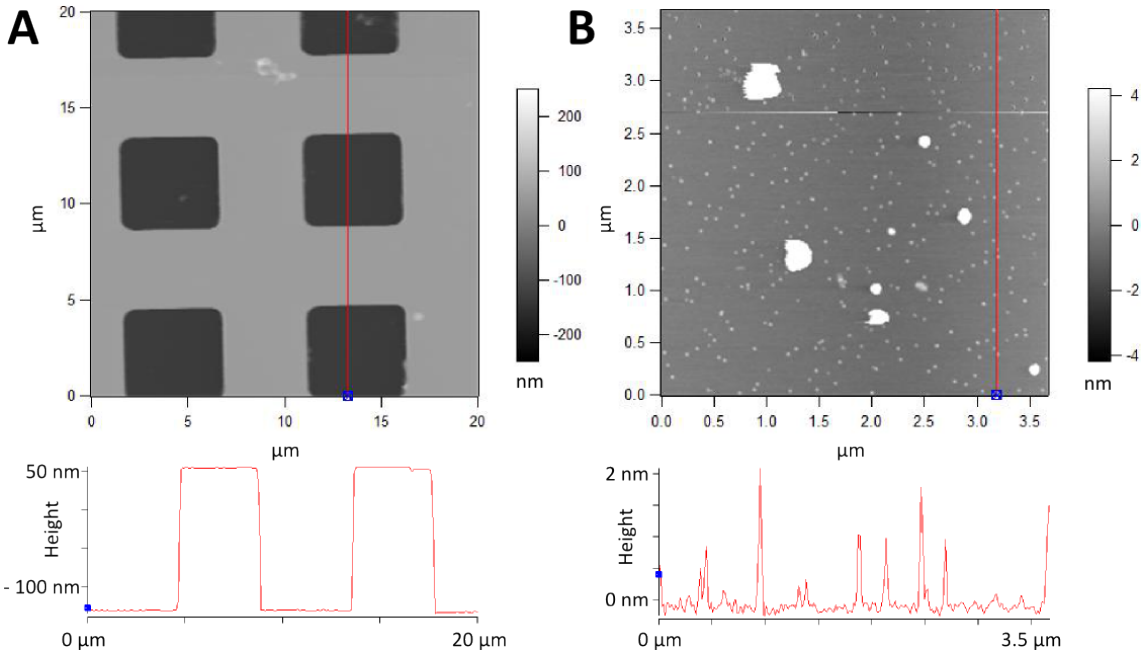

Figure 2.4 Processed AFM **t**opography images with XY cross-sections underneath from **Figure 2.3** (**A**) histogram flattening and (**B**) "magic mask" flattening. The remaining horizontal line artefact in (B) is probably caused by the tip jumping from the substrate or external noise and can be removed manually.

In addition to these procedures, manually defining the $Z = 0$ plane can be achieved by subtracting or adding a discrete offset in the following manner:

```
ExtractLayer()
LayerData=LayerData+1.04e-7
ARExecuteControl("OldCommandPop","ARImGr0Drifttest0001",6,"Insert Layer")
```

This example would add a Z offset of 104 nm to the entire "ARImGr0Drifttest0001" image.

2.5 Statistical tools

Statistical tools are widely used throughout this thesis to gain a quantitative understanding of the experimental data collected. They include methods to describe, summarise and visualise data, methods to combine and compare nanoparticle

characterisation data and methods to compare the effects of different treatments on *E. coli*. In this section a summary of the key concepts and statistical techniques used is provided (Rice 2007).

2.5.1 Descriptive statistics

Exploratory data analysis conducted in this thesis includes basic visualisation techniques such as histograms to display frequency distributions of the data (Figure 2.5A), and boxplots to display summary statistics (Figure 2.5B). Boxplots allow a quick way of assessing homogeneity of data (i.e. are the median and mean similar? Is the median centred within the IQR?). Summary statistics calculated include those for location (e.g. mean, median) and dispersion (e.g. variance, IQR).

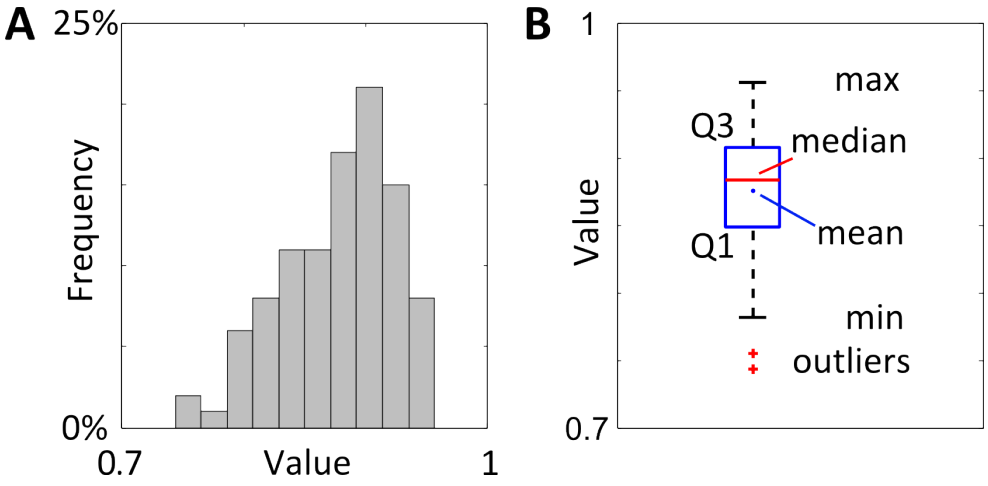

Figure 2.5 Examples of basic data visualisation: (**A**) Histograms display the frequency of data, binned into groups, and (**B**) boxplots display the same data with max, min, median, mean and outliers labelled as displayed. Q3 and Q1 represent the 75th and 25th quartiles respectively. The interquartile range (IQR, blue box) is defined as (Q3 – Q1). The range is defined as (max – min), where max and min correspond to Q3 + (1.5*IQR) and Q1 – (1.5*IQR) respectively. Outliers are defined as values falling outside the range.

2.5.2 Inferential statistics

After describing and summarising the data, it is often necessary to make inferences based on data from two or more experiments. For example, in testing the effectiveness of a new drug, a series of experiments between a control and the drug may be conducted resulting in two distributions of data (e.g. heights of cells). The question of interest would

be whether the two distributions are different. Hypothesis testing allows this question to be answered quantitatively through the establishment and testing of a null and alternative hypothesis. Loosely speaking the null hypothesis would be that there are no significant differences between the two data sets. The alternative hypothesis would be that there *are* differences between the data sets. The test is then conducted at a significance level alpha (α) (0.05 in this thesis). The resulting p-value corresponds to the probability of an effect as or more extreme than that observed in the drug data set occurring by chance. If the p-value is below the significance level α, the null hypothesis is rejected.

The false rejection of the null hypothesis is a Type I error, while a false acceptance of the null hypothesis is a Type II error. It is important to minimise the number of Type I and II errors, which are related to each other by the sample size. With any hypothesis test the underlying assumptions behind the test (e.g. data is normally distributed, or variances are equal between datasets) must themselves be rigorously tested. Tests for normality include a Shapiro-Wilk test and Bartlett's test. The null hypothesis (that the data is normally distributed) is rejected when the p-value < α.

For multiple comparisons (e.g. multiple drugs), global methods must be used to compare across samples.

2.5.2.1 **Analysis of Variance (ANOVA)**

When multiple datasets are considered (e.g. multiple drug are tested), multiple comparisons between groups are of interest. Global tests that look for differences between groups include ANOVA for normally distributed data and the Kruskal-Wallis test for non-normally distributed data. These global tests can be used to discover differences

between group means or medians respectively without elucidating which groups the difference(s) is/are due to.

Exhaustively testing two-samples at a time within a large group will result in an increase in Type I errors and post-hoc multiple comparison techniques must be employed. For normally distributed data, Tukey's Honest Significant Difference method can be employed to test for significant differences between groups. For non-normally distributed data the Kruskal-Wallis multiple comparison test can be employed. In both cases, significant differences between specific groups are found, while reducing the rate of Type I errors.

2.5.3 Summary

Figure 2.6 summarises the statistical techniques used in this thesis, with the exception of bootstrapping, which is described in Chapter 3 and Appendix A.

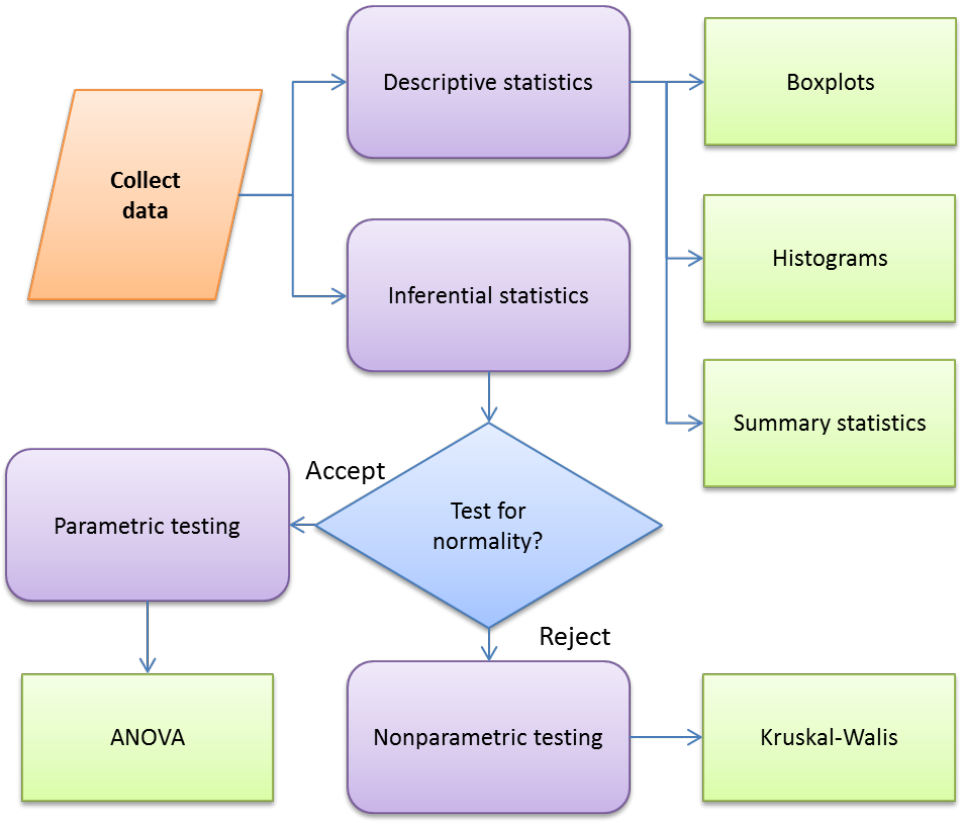

Figure 2.6 Summary of statistical tools used in this thesis. From data collected experimentally, descriptive statistics can be immediately calculated. Inferential statistics require careful design, in particular with respect the sample sizes used, and the normality of data acquired.

Chapter 3

Improved stability of silver nanoparticles

Prior to the development of a standard methodology to study the interactions of nanoparticles with cells, the effects of three different stabilisation strategies on silver nanoparticles are reported and discussed. Nanoparticles are characterised using UV-Vis spectroscopy, TEM and AFM. The work in this chapter was published in Nanoscale Research Letters *(Stevenson, Blanco Bea et al. 2012).*

Contributions: *nanoparticle synthesis, functionalisation and UV-Vis spectroscopy were conducted by Duani Blanco Bea, Dr. Sonia Trigueros and Dr. Alberto Iglesias Cerveto at the University of Havana, Cuba. Transmission electron microscopy (TEM) data were obtained by Dr. Mike Shaw at the Sir William Dunn School of Pathology, University of Oxford. Dr. Sergi Civit at the University of Barcelona proposed and conducted the bootstrap statistical analysis. Analysis of TEM data was developed and conducted by the author. Acquisition and analysis of AFM data were conducted by the author with supervision from Dr. Sonia Contera.*

3.1 Introduction

The properties of nanostructures depend critically on their size, shape, dispersion and surface charge, particularly as they interact with biological entities (Verma and Stellacci 2010). Their accurate characterisation is essential before undertaking further studies investigating their application and/or toxicity.

Silver nanoparticles are a subset of metallic nanoparticles which are attractive for many applications due to their strong plasmonic characteristics and availability of synthesis methods (Mulvaney 1996). The biomedical properties of silver are also of great interest, given the antibacterial nature of silver which has been utilised for many centuries (Lansdown 2010). Dendrimeric nanoparticles with silver cores were explored in our group as candidates for drug delivery, but the stability of silver nanoparticles in the aqueous

solutions required for biological interactions was poor (Trigueros 2008). This chapter details the characterisation of four silver-based nanoparticles synthesised in an effort to improve the stability of silver nanostructures in collaboration with the University of Havana, Cuba.

3.1.1 Nanoparticle synthesis

There are two broad manufacturing methods for engineered nanoparticles: “top down” and “bottom up”. Top down synthesis involves breaking down bulk material to form nanoscale structures, for example via mechanical milling, laser ablation, focused ion beam or electron beam lithography (Morales and Lieber 1998, Arbain, Othman et al. 2011) (Vieu, Carcenac et al. 2000, Khizroev and Litvinov 2004). Bottom up methods include colloidal synthesis (this work), chemical vapour deposition and molecular self-assembly (Li, Xie et al. 1996, Goodman, Schaap et al. 2005). The choice of synthesis pathway will depend greatly on the final medium of the nanostructure: milling methods are suitable for dry powders, and polyol synthesis suited for inorganic applications (Feldmann and Jungk 2001). For nanoparticles in aqueous solutions, colloidal synthesis is popular and was one of the first methods recorded to produce gold nanoparticles (Faraday 1857).

The quantitative study of colloidal synthesis arrived with the advent of electron microscopy which allowed the nucleation and growth of nanoparticles synthesised via chemical reduction of a precursor to be studied (Turkevich and Hillier 1949, Turkevich, Stevenson et al. 1951). Figure 3.1 shows an illustration of the reduction, nucleation and growth process. Colloidal synthesis is a popular method due to the ability to synthesise nanoparticles directly in aqueous solution, however controlling the size and shape of nanoparticles synthesised remains challenging: particles are often heterogeneous in size

and shape unless multiple reaction parameters are carefully regulated (Chen, Jiao et al. 2010, Zhang, Xie et al. 2010). Synthesis via multiple steps, seed-mediated growth or via organic solvents has overcome several of these problems, although these syntheses increase in complexity with the number of steps involved, and will limit potential biomedical applications when organic solvents are used (Jana, Gearheart et al. 2001, Jana and Peng 2003, Dong, Ji et al. 2009). Transfer of nanoparticles from their organic solvents to aqueous systems requires re-characterisation of their physical properties as well as their long-term stability.

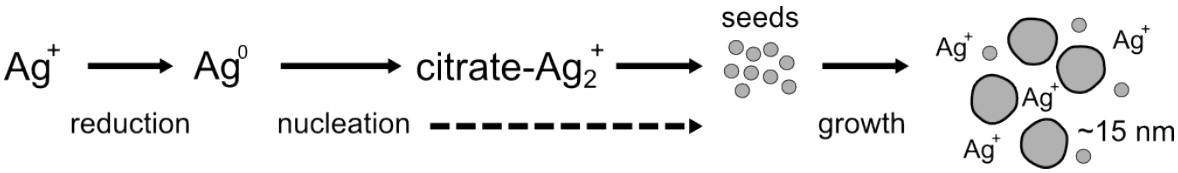

Figure 3.1 Cartoon illustrating the reduction, nucleation and growth of silver nanoparticles from a silver salt (typically $AgNO_3$) and trisodium citrate.

One of the key steps to controlling the stability of nanoparticles post-synthesis lies in their functionalisation (or "capping"). In this chapter three strategies to functionalise nearly monodisperse silver-based nanoparticles directly in aqueous solution are compared. 14 nm quasi-spherical nanoparticles were functionalised with polyethylene glycol (PEG), gold (core-shell) and chromium (alloy). UV-Vis spectroscopy, TEM and AFM were used to characterise the nanoparticles and establish their stability in liquid. Statistical bootstrapping tools were applied to test the validity of the techniques, demonstrating a close relationship between homogeneity of nanoparticle size, shape and particle sphericity.

3.2 Materials and methods

3.2.1 Silver nanoparticle synthesis and UV-Vis characterisation

Nanoparticle synthesis, functionalisation and UV-Vis spectroscopy were conducted by Duani Blanco Bea, Dr. Sonia Trigueros and Dr. Alberto Iglesias Cerveto at the University of Havana, Cuba.

Silver nanoparticles coated with citrate (Ag nanoparticles) were obtained using the Turkevich method (Turkevich, Stevenson et al. 1951). A solution of silver nitrate (125 ml, 1mM) was heated to 95 °C, to which a solution of trisodium citrate (7.75 mM) was added. Nearly 15 minutes later a colour change was observed indicating the formation of nanoparticles, and the solution was cooled to room temperature and stored at 5 °C. During synthesis a constant pH 6.5 was maintained.

PEG-functionalised silver nanoparticles (AgPEG) were obtained by immediately adding a solution of PEG-6000 (80 mM) to freshly synthesised (as above) silver nanoparticles (50 ml), cooling the sample to -5 °C for 8 hours before storing at 5 °C.

Silver-gold nanoshells (Ag-Au) were obtained by the successive reduction of two metal salts. A fresh solution of silver nanoparticles was prepared as previously described, then immediately heated to 90 °C, to which a solution of hydrogen tetrachloroaurate (1.2 mM) was added. The reaction mixture was heated to 95 °C and a further solution of trisodium citrate (7.75 mM) was added. When a colour change was observed the mixture was cooled gradually to room temperature and stored at 5 °C. During the second reaction, chloride ions produced from the reduction of hydrogen tetracholoaurate reacted with unbound silver forming a silver halide which sedimented rapidly and was easily removed from the final mixture.

Silver-chromium alloy nanoparticles (AgCr) were synthesised by co-reducing two metal salts. A solution of potassium dichromate dissolved in sulphuric acid (5 ml, 42 mM) was diluted twice in water (10 ml) and added to a solution of silver nitrate (125 ml, 1 mM) before heating to 95 °C. A solution of trisodium citrate (7.75 mM) was then added. When a colour change was observed the mixture was cooled to room temperature and stored at 5 °C.

UV-Vis absorption spectra of all nanoparticle samples were obtained using an MDR-23 monochromator, LOMO, Russia.

3.2.2 Transmission electron microscopy (TEM)

Transmission electron microscopy (TEM) images of nanoparticles were obtained by Dr. Mike Shaw at the Sir William Dunn School of Pathology, University of Oxford. The author developed and performed TEM analysis.

Aliquots of nanoparticles were deposited on formvar-coated 200 mesh copper grids, and the excess liquid was wicked off with filter paper. The samples were air-dried and examined unstained in a Tecnai 12 TEM (FEI, Eindhoven, Nl). Images were recorded using a Gatan US1000 2K CCD camera.

TEM images obtained consisted of 16-bit greyscale images and were analysed using ImageJ 1.43u (NIH, Bethesda, MD). The perimeter of each nanoparticle was obtained manually using a digital stylus. Automatic thresholding was possible for well-separated nanoparticles, but failed when nanoparticles were closely clustered. For consistency, all images were processed manually. Perimeter and areas were extracted before calculating circularity $= 4\pi\left(\frac{Area}{Perimeter^2}\right)$ and estimated diameter $= 2\sqrt{\frac{Area}{\pi}}$ considering the particles to be spherical. Both metrics were sensitive to pixel density, with smaller particles

yielding larger rounding errors due to the lower number of pixels available. Histograms of nanoparticle diameters were obtained using Matlab R2010a (Mathworks, Massachusetts, U.S.A.).

3.2.3 Atomic force microscopy (AFM)

AFM was carried out in air and in liquid operating in amplitude modulation mode with Olympus AC240 (k = 2 Nm^{-1}) silicon cantilever tips in air and Olympus TR800/400 (k = 0.57 Nm^{-1}/0.08 Nm^{-1}) silicon nitride cantilevers in liquid.

Nanoparticle heights were calculated by thresholding topography images and extracting the Z-range of each particle. Lateral data (nanoparticle diameters) were heavily affected by tip-sample convolution. Deconvolution algorithms were evaluated in the software packages SPIP 3.2.10.0 (Image Metrology, Hørsholm, Denmark), Gywddion 2.22 (Czech Metrology Institute, Brno, Czech Republic) and WSxM 3.0 (Horcas, Fernandez et al. 2007). Due to the uncertainty in the tip angle and hence geometry in contact with the sample, deconvolution of lateral dimensions, dependent on accurate tip geometry, was not pursued (Villarrubia 1997). Histograms of nanoparticle heights were obtained using Matlab R2010a.

3.2.4 Bootstrap statistical analysis of TEM and AFM data

Dr. Sergi Civit at the University of Barcelona formulated and conducted the bootstrap statistical analysis.

TEM diameters and AFM heights were combined according to the eccentricity statistic distribution ε (eq. (1.2)) using non-parametric bootstrap resampling techniques:

$$\varepsilon = \sqrt{\frac{a^2 - b^2}{a^2}} = \sqrt{1 - \left(\frac{b}{a}\right)^2} \tag{3.1}$$

where $0 < \varepsilon < 1$, and a and b are the one-half of ellipse's major and minor axes (diameter and height) respectively. As the eccentricity value ranges from 0 to 1, the nanoparticle can be classed as spherical to ellipsoidal respectively. The sphericities of nanoparticles resulting from different stabilisation strategies were then compared via the non-parametric Kruskal-Wallis hypothesis test (Appendix A). This enables a three-dimensional characterisation of nanoparticles without the need for highly specialised techniques such as annular dark-field scanning transmission electron microscopy (ADF STEM) (Gontard, Dunin-Borkowski et al. 2009).

3.3 Results

3.3.1 AFM sample preparation

Imaging nanoparticles in liquid required careful sample preparation: the correct substrate is required for nanoparticles to be sufficiently attached to the surface for imaging in liquid, without altering the structure of the nanoparticles themselves.

For AFM imaging in liquid (Ag, AgCr) nanoparticle samples (2 μl) were diluted in NaCl (48 μl, 20 mM with 50 mM HEPES, pH 6.5) and bath sonicated (Ultrawave U300, Ultrawave, Cardiff, UK) for 15 minutes. Samples were then incubated on freshly cleaved mica for 20 minutes at room temperature before imaging in the same NaCl buffer. Due to the hydration of PEG, the height of AgPEG nanoparticles characterised by AFM in liquid was found to be twice the value of the diameter from TEM. As such, AgPEG nanoparticles were characterised in air by adding 2 μl nanoparticle sample onto freshly cleaved mica and air-drying before imaging. It was not possible to sufficiently attach the larger Ag-Au nanoparticles to various surfaces for imaging in liquid. Ag-Au nanoparticles were instead imaged in air after coating freshly cleaved mica with poly-l-lysine (0.01% 5 μl), drying, incubating with nanoparticle sample (2 μl nanoparticle solution with 48 μl NaCl, pH 6.5)

for 2 hours before washing with milli-Q water and drying. Low scan rates were used (typically 0.3 Hz line scan rate) to minimise the displacement of nanoparticles on the sample surface during scanning.

3.3.2 Silver nanoparticle instability

Citrate coated silver nanoparticles were characterised in air and in liquid (Figure 3.2). The nanoparticles exhibited a narrow absorption peak at 433 nm due to plasmonic resonance (Figure 3.2A), indicating a narrow size and shape distribution immediately post-synthesis (Bohren and Huffman 1998). TEM and AFM data obtained 100 days after synthesis gave a (median ± interquartile range (IQR)) particle diameter and height of 14 ± 10 nm (Figure 3.2B) and 10 ± 29 nm (Figure 3.2C) respectively. The large IQR in both TEM and AFM data show strong heterogeneity in the size and shape of nanoparticles synthesised. Large (> 100 nm height) aggregates were observed directly in liquid (Figure 3.2C), confirming that the instability of silver nanoparticles observed was not due to drying-induced aggregation during TEM sample preparation.

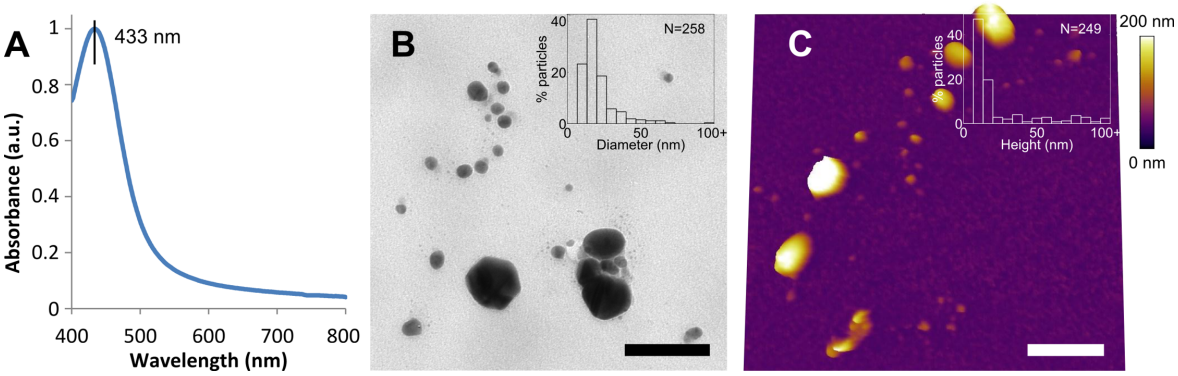

Figure 3.2 Characterisation of silver nanoparticles (AgNP). (**A**) UV-Vis absorbance (arbitrary units) spectrum showing narrow absorption peak at 433 nm. (**B**) Transmission electron microscopy (TEM) image showing heterogeneous nanoparticles 100 days post-synthesis (scale bar: 100 nm), with inset particle diameter distribution. (**C**) Atomic force microscopy (AFM) topography image in liquid showing heterogeneous nanoparticles 100 days post-synthesis (scale bar: 700 nm), with inset particle height distribution.

3.3.3 Silver nanoparticle functionalisation with PEG

To improve the stability of the silver nanoparticles, they were functionalised with polyethylene glycol (PEG) immediately after synthesis. The resulting AgPEG nanoparticles

are shown in Figure 3.3. The UV-Vis spectrum shows a distinct shift in the absorbance from 433 nm to 894 nm (Figure 3.3A). TEM characterisation gave a median metallic particle diameter of 47 ± 27 nm (Figure 3.3B). AFM characterisation gave a median particle height of 40 ± 14 nm (Figure 3.3C). The substantial absorbance shift observed has been reported during photo-induced conversion of nanospheres to nanoplates, although no evidence of nanoplates during both TEM and AFM characterisation was found (Jin, Cao et al. 2001, Aherne, Ledwith et al. 2008). The shift may be due to a complex coupled absorbance phenomenon arising due to the proximity of nanoparticles linked with PEG (Dusemund, Hoffmann et al. 1991). Drying the sample for AFM in the presence of ethanol, smaller seed particles absorbed by PEG surrounding the core silver nanoparticles were indeed observed (Figure 3.3C inset). Trapping seeds in this way will prevent further uncontrolled growth via Ostwald ripening (Kahlweit 1975). The use of PEG as a functionalising agent is common and attributed to steric repulsion between PEG chains adsorbed on nanoparticle surfaces (Shkilnyy, Soucé et al. 2009). The combination of steric repulsion and the trapping of seeds prevents further uncontrolled growth and improves stability. The larger particle size after functionalisation could be explained by the reported activity of PEG as a reducing agent of silver ions (Li, Guo et al. 2010). PEG may continue to catalyse ion reduction in the nanoparticle solution, consequently increasing nanoparticle size.

3.3.4 Silver nanoparticle functionalisation with gold

To explore the effects of non-steric stabilisations on surface stability, silver nanoparticles were functionalised with gold to create bimetallic silver-gold nanoshells (Ag-Au). Gold nanoparticles synthesised by the same Turkevich method are known for their homogeneity, and suggest an increased stability between gold and citrate, providing the motivation for a gold shell (Frens 1973).

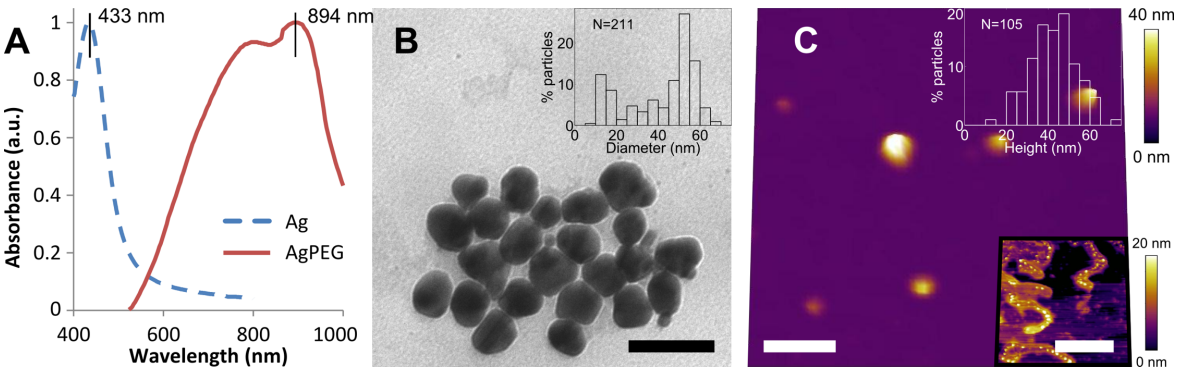

Figure 3.3 Characterisation of PEG-functionalised silver nanoparticles (AgPEG). (**A**) UV-Vis absorbance spectrum showing a significantly shifted absorption peak at 894 nm. The original silver nanoparticle spectrum is shown for comparison. (**B**) TEM image showing homogeneous nanoparticles 100 days post-synthesis (scale bar: 100 nm), with inset particle diameter distribution. (**C**) AFM topography image in air showing disperse homogeneous nanoparticles 100 days post-synthesis (scale bar: 1 μm), with upper inset particle height distribution. Lower inset shows AgPEG nanoparticles dried in ethanol (scale bar: 1 μm), revealing absorption of small nanoparticles in PEG.

Two types of bimetallic nanoparticles can be obtained: i) nanoparticles consisting of two metals with well separated distributions called core-shell nanoparticles (nanoshells) and ii) nanoparticles with a homogeneous distribution of two metals called alloys (Toshima and Yonezawa 1998). Nanoshells can be obtained by successive reduction of two metals; in the first step the metal of the nucleus of the nanoparticle is reduced and then, in the second step, a layer is formed by the reduction of a second metal. Figure 3.4 shows the Ag-Au nanoshells obtained. The UV-Vis spectra contain two absorption peaks at 439 nm and 629 nm (Figure 3.4A), indicating the complex resulting electronic structure of the bimetallic nanoparticles. A redshift in the gold peak of 103 nm from 526 nm to 629 nm, and a smaller shift of 29 nm in the silver peak from 410 nm to 439 nm were observed. TEM and AFM data obtained 100 days post-synthesis gave a median particle diameter of 39 ± 16 nm (Figure 3.4B), and a median particle height of 28 ± 14 nm (Figure 3.4C) respectively. The lack of smaller seed-like particles observed is likely due to the sedimentation step during synthesis: any silver salts remaining bind strongly to halides resulting in precipitation (Davies and Jones 1949). The nanoshells obtained were homogenous in both size and shape, in contrast to the pure silver nanoparticles. The

higher valence of gold used (+3 compared to +1 for silver) may affect metal-citrate bonding, with more citrate ions able to bind to each metal ion at the surface, subsequently leading to increased stability.

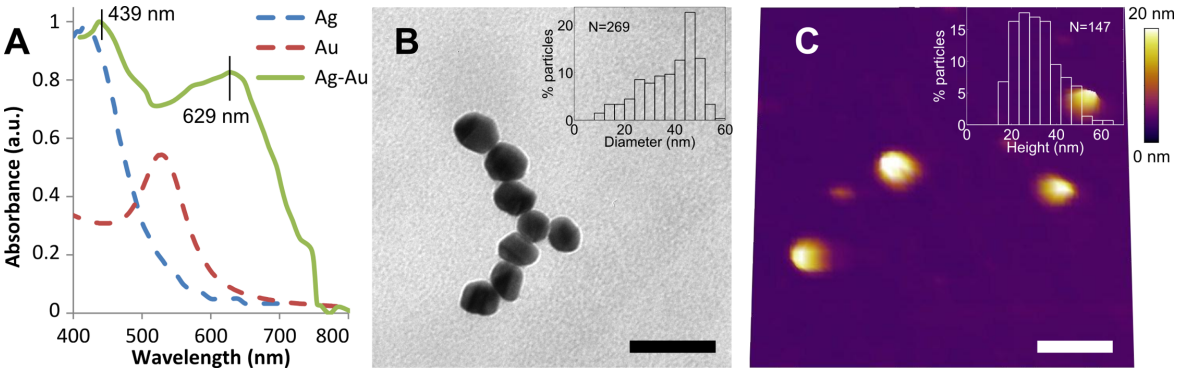

Figure 3.4 Characterisation of bimetallic silver-gold nanoshells (Ag-Au). (**A**) UV-Vis absorbance spectra showing pure silver and pure gold nanoparticles for comparison, and the Ag-Au bimetallic nanoparticle, with two absorption peaks at 439 nm and 629 nm. (**B**) TEM image showing homogeneous nanoparticles 100 days post-synthesis (scale bar: 100 nm), with inset particle diameter distribution. (**C**) AFM topography image in air showing disperse homogeneous nanoparticles 100 days post-synthesis (scale bar: 800 nm), with inset particle height distribution.

3.3.5 Silver nanoparticles alloyed with chromium

To further investigate whether a weak silver-citrate affinity at the nanoparticle surface is responsible for nanoparticle instability, silver-chromium alloy nanoparticles were synthesised with a mixture of two metals, where chromium has a higher valence (+6) than silver or gold.

The characterisation of AgCr alloy nanoparticles obtained is shown in Figure 3.5. The presence of chromium in the nanoparticles did not alter the position of the UV-Vis absorption peak substantially (479 nm compared to 433 nm for pure silver, Figure 3.5A), but broadened the spectrum, corresponding to the reported broader absorption of Cr^{3+}/Cr^{6+} (Fahnestock, Manesse et al. 2009). TEM and AFM characterisation 100 days post-synthesis gave a median particle diameter of 12 ± 6 nm (Figure 3.5B) and a median particle height of 7 ± 4 nm (Figure 3.5C) respectively. The diameter and height distributions were well confined to below 40 nm, although smaller seeds were found to

be numerous. Despite the presence of these seeds, the alloy nanoparticles remained stable in size, shape and dispersability confirming that the presence of a higher valence metal (chromium) on the nanoparticle surface significantly improves stability, without requiring the complete capping of the core metal.

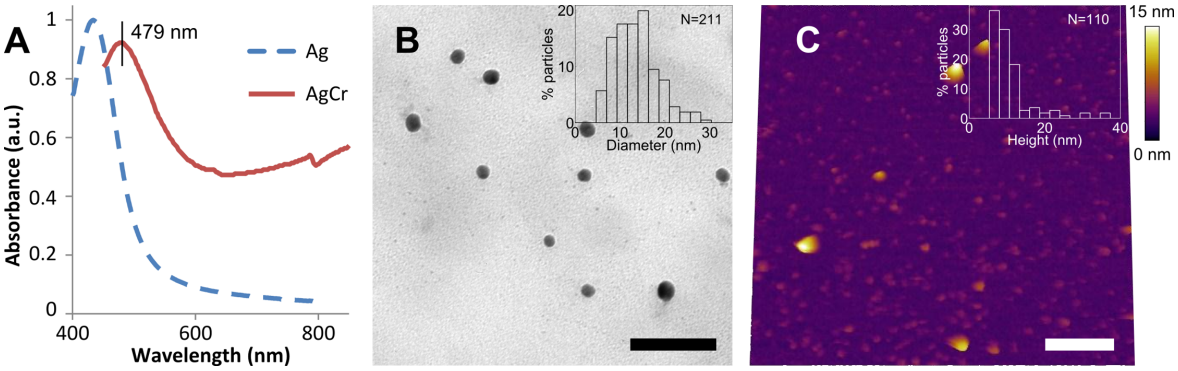

Figure 3.5 Characterisation of bimetallic silver-chromium alloy nanoparticles (AgCr). (**A**) UV-Vis absorbance spectrum showing an absorption peak at 479 nm. The spectrum for pure silver nanoparticles is shown for comparison. (**B**) TEM image showing disperse nanoparticles 100 days post-synthesis (scale bar: 100 nm), with inset particle diameter distribution. (**C**) AFM topography image in liquid showing disperse nanoparticles 100 days post-synthesis (scale bar: 150 nm), with inset particle height distribution.

3.3.6 Size and shape distributions of nanoparticles from TEM

To quantify the effects previously described on the size and shape of the nanoparticles obtained, TEM nanoparticle profiles were analysed. Figure 3.6 shows two-dimensional histograms of nanoparticle diameters and circularities calculated for all four types of nanoparticles synthesised in this study.

In a TEM image, circularity is defined as the ratio of the area of a nanoparticle with its perimeter, determined via segmentation. Circularity ranges from a value of 1 for a circular object (spherical or disc-shaped nanoparticle, with the latter eliminated due to the complete absence of discs in the data) to 0 for a highly elongated object (rod-shaped). No single particles with circularity lower than 0.4 were observed.

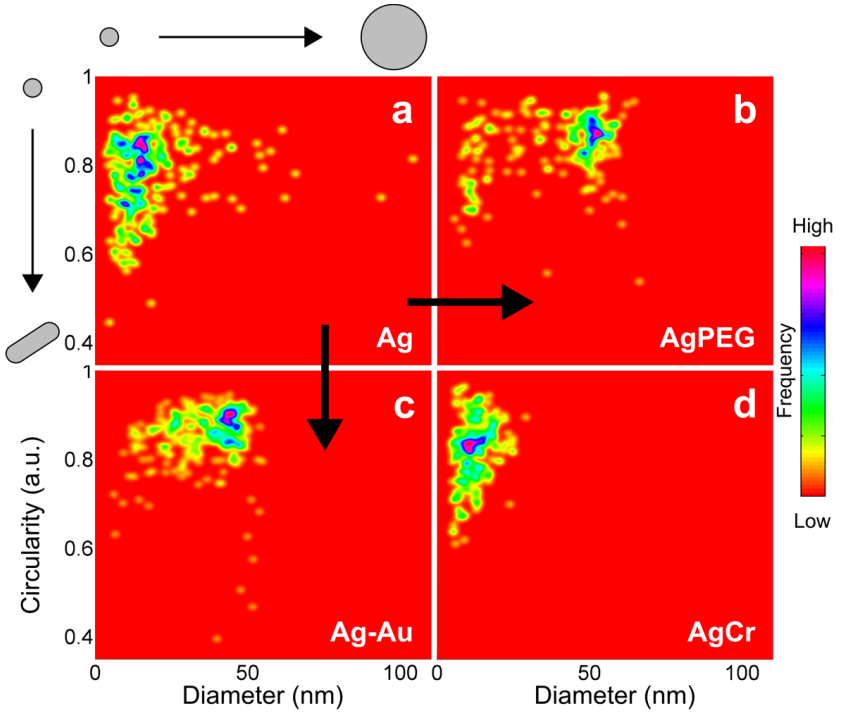

Figure 3.6 Two dimensional histogram of nanoparticle diameter correlated to 2D circularity from TEM data. A circularity of 1 indicates a spherical particle, and 0.4 indicates a rod-shaped particle. More dense regions appear purple and represent larger populations. (**a**) Ag, (**b**) AgPEG, (**c**) Ag-Au and (**d**) AgCr nanoparticles.

Silver nanoparticles (Figure 3.6a) were the most heterogenic in size and shape. Functionalising silver nanoparticles with PEG (Figure 3.6b) resulted in particles with an increased diameter and circularity, both more narrowly distributed, indicating the predominance of a single species of nanoparticle. AgPEG nanoparticles around 15 nm in diameter observed in the histogram were most likely remaining unfunctionalised nanoparticles. Capping with gold to create the Ag-Au nanoshells (Figure 3.6c) resulted in particles with an increased and more narrowly distributed diameter and circularity, again indicating the tendency towards a single species. A small presence of rods was observed, expected in the gold functionalisation step as by-products of pure gold rod formation. Finally, AgCr alloy nanoparticles (Figure 3.6d) were the most narrowly distributed in size, with no particle diameters above 40 nm. Circular objects were predominant, although the circularity metric is compromised as particle diameters tend to zero, explaining the broad range of circularities measured in the case of the smaller AgCr nanoparticles.

3.3.7 Bootstrapping TEM and AFM

Finally, particle shape in three dimensions was investigated by bootstrapping TEM diameters and AFM heights using statistical bootstrapping and the eccentricity statistic ε (Figure 3.7A - see Materials and Methods and full results in Appendix A).

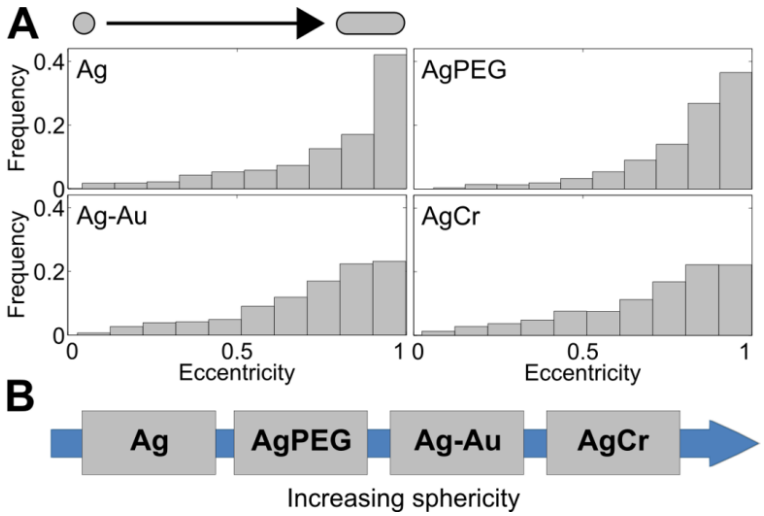

Figure 3.7 Statistical analysis of nanoparticle shape from combining TEM (diameter) and AFM (height) data distributions. (**A**) Eccentricity bootstrap distributions obtained for each nanoparticle type. High frequencies to the left x-axes (low eccentricity values) indicate a spherical nanoparticle. (**B**) Results of non-parametric Kruskal-Wallis hypothesis testing on particle eccentricity (a low eccentricity corresponds to a high sphericity).

Eccentricity and particle sphericity are inversely proportional: a lower eccentricity corresponds to a higher particle sphericity. A higher particle sphericity indicates a more stable, homogenous growth process. Non-parametric ANOVA found significant ($p < 0.05$) differences between nanoparticle types. Nanoparticle sphericities were found to increase with each stabilisation strategy, i.e. unfunctionalised nanoparticles were the least spherical, followed by PEG-functionalised, silver-gold nanoshells and silver-chromium alloy nanoparticles (Figure 3.7B). This supports the hypothesis that higher valence metals present on the surface of the nanoparticles exert a stabilising effect.

3.4 Conclusions

Through a combination of UV-Vis spectroscopy, TEM and AFM characterisation and statistical analysis, the stabilities of four different silver-based nanoparticles were

investigated. 14 nm quasi-spherical silver nanoparticles were synthesised directly in water without organic solvents. After 100 days in solution, the nanoparticles exhibited increased heterogeneity due to their inherent instability. PEG and gold were used as organic and inorganic capping agents respectively. In both cases further growth and stabilisation of the resultant nanoparticles were effectively controlled. The addition of PEG not only stabilises the nanoparticles by steric repulsion, but also allows controlled further growth of nanoparticles, improving homogeneity in nanoparticle size, shape and stability. In the case of Ag-Au nanoshells, the higher electron affinity of gold may lead to a stronger gold-citrate interaction at the nanoparticle surface compared to the pure silver nanoparticles, consequently improving size and shape homogeneity and long-term stability. The higher valence of chromium than gold may lead to an even stronger chromium-citrate interaction at the nanoparticle surface. This results in smaller nanoparticle diameters as nanoparticles are stabilised earlier in their growth process due to the increased citrate bonding at their surfaces. The alloying process also enables the production of stable silver-based nanoparticles without the need for additional functionalisation/capping.

For nanomedical applications, a stable, homogenous nanoparticle is essential. Silver-chromium nanoparticles were the most stable and homogenous and would be the preferred candidates for further investigation.

With an understanding of the complexity of nanoparticle stability, and a multi-technique approach to nanomaterial characterisation, a standard methodology for examining the interaction of such nanoparticles with living matter is developed in the next chapter.

Chapter 4

A standard methodology to study the interactions of nanoparticles with cells

This chapter describes the development of a standard methodology to study nanoparticle-cell interactions. The gram-negative bacterium E. coli *is used as a model organism, and in the next chapter silver nanoparticles are used as a test nanomaterial.*

4.1 Introduction

The need for a standard methodology to study nanoparticle-cell interactions is pressing (Hunt, Lynch et al. 2013). To date a variety of protocols have been used to probe the interactions of a number of nanomaterials with cells from human, plant, fish, animal, bacterial and fungal organisms (Fischer and Chan 2007, Fadeel and Garcia-Bennett 2010, Farkas, Christian et al. 2011, Krug and Wick 2011, Arora, Rajwade et al. 2012, Poynton, Lazorchak et al. 2012, Suresh, Pelletier et al. 2013). Current protocols are specific for the nanomaterials and cells in question, and without a standardised approach to studying nanomaterial-cell interactions the growing body of research into nanotoxicity cannot be easily compared across nanomaterials for different cell types. Further, to the best of the author's knowledge, none of the current protocols available make use of the existing toxicological knowledge of established drugs. The behaviour of existing drugs may help understand nanoparticle interactions by comparison. For example, a nanoparticle may exert similar effects to e.g. antibiotics or anti-cancer drugs with specific, well-known mechanisms of action.

4.2 Methodology

The proposed approach to overcoming these limitations is shown in Figure 4.1. The methodology begins with the characterisation of the cells in question with a variety of existing drugs with known mechanisms of actions and effects. By carefully selecting the drugs and characterisation techniques used, a comparative “atlas” is constructed for each cell type. This atlas serves as a quantitative reference for comparing further experiments, characterising the interactions of nanoparticles with the cells. Through statistical testing, similarities between known mechanisms of actions of drugs and nanoparticle effects can suggest or eliminate specific nanoparticle-cell interactions and highlight additional mechanisms to investigate. Once the reference atlases are created, they can be compared repeatedly as new nanomaterials are developed.

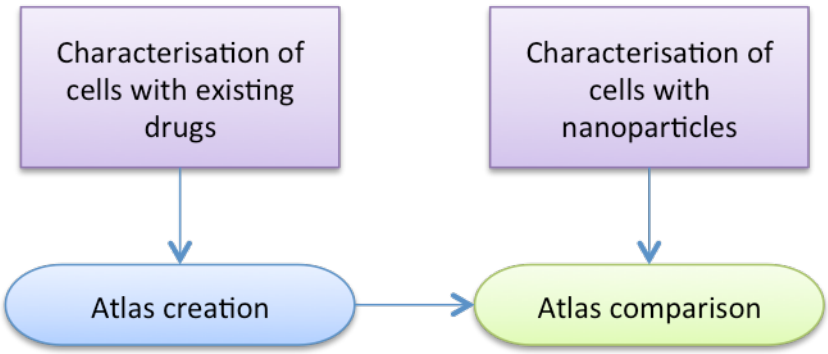

Figure 4.1 Overview of the proposed methodology to study nanoparticle-cell interactions. The methodology involves the creation of an "atlas" of the effects of known drugs for each cell type of interest, followed by the comparison of the effects of the nanoparticle of interest. An understanding of nanoparticle-cell interactions is obtained by statistically comparing the characterised effects of known mechanisms of action with the unknown mechanism(s) of action of a nanoparticle.

In this chapter a model organism, suitable drugs and characterisation techniques are chosen to create a reference atlas. In the next chapter, the interactions of a number of nanoparticles with cells are compared and contrasted.

4.2.1 *Escherichia coli* (E. coli) as a model organism

Bacteria, single celled organisms without organelles or a nuclear structure, are ubiquitous, even in the most hostile environments on the planet (Edwards 1990). They

are responsible for the nitrogen cycle, a large proportion of the carbon cycle, the conversion of food into nutrients in the digestive tracts of animals, waste water treatment, bioremediation, food production, drug production and genetic engineering (as vectors) as well as infection and disease (Postgate 2000, Mitchell and Gu 2010). Their often rapid duplication times, driven by binary fission, have enabled their wide study and manipulation in the laboratory (Murray 2007). Understanding the effects of nanomaterials on these organisms is of double importance: unintended toxicity from the increasing presence of nanomaterials must be mitigated to preserve the roles of bacteria in the ecosystem, and any discovered toxicity could be put to use in a medical context as the traditional antibiotic production pipeline diminishes (Spellberg, Guidos et al. 2008).

Two major groups of bacteria are gram-negative and gram-positive, distinguished by the structure of their cell walls and subsequent differences in staining under the peptidoglycan-specific Gram stain (Beveridge 2001). Gram-negative bacteria include a large number of organisms in the clinically important genera *Salmonella*, *Shigella*, and *Legionella* and the species *Escherichia coli (E. coli)*, *Haemophilus influenza* and *Klebsiella pneumoniae*.

E. coli DH5α is a widely used and well-studied gram-negative strain that was selected as a model cell for the development of the methodology (Grant, Jessee et al. 1990, Neidhardt 1996). The general anatomy of gram-negative cells is discussed before relevant drugs and characterisation techniques are selected for atlas creation.

4.2.2 Gram-negative structure and drug candidates

An examination of the gram-negative cell wall reveals four broad targets for drug or nanoparticle interactions (Figure 4.2):

1. The outer membrane, including lipopolysaccharides;

2. the peptidoglycan cell wall located in the periplasmic space;

3. the inner membrane;

4. processes within the cytosol (e.g. protein synthesis, DNA replication).

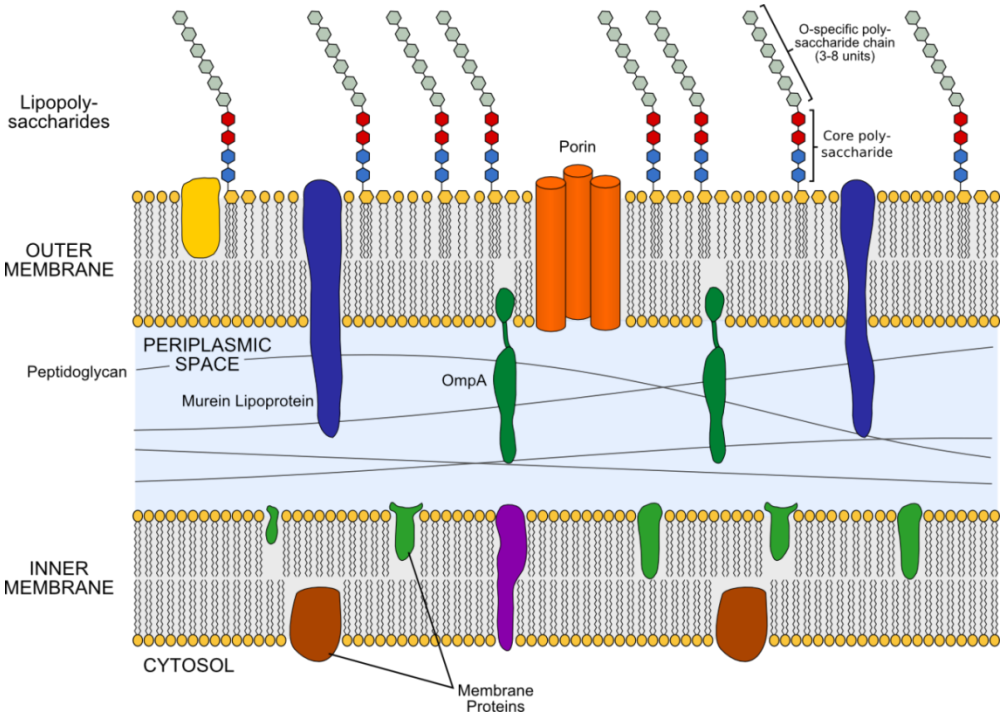

Figure 4.2 Schematic of a gram negative bacterium cell wall, adapted from Dahl (2012). Four possible targets are illustrated: lipopolysaccharides and outer membrane, peptidoglycan in the periplasmic space, the inner membrane and internal processes in the cytosol.

For the creation of the atlas, four antibiotics with distinct mechanisms of actions were selected based on the targets above (Table 4.1):

Antibiotic	Target	Mechanism	Reference
Ampicillin	Peptidoglycan *via* penicillin binding proteins	Binds to peptidoglycan transpeptidases, inhibiting their ability to cross-link newly synthesised peptidoglycan.	(Spratt 1983, Waxman and Strominger 1983)
Kanamycin	Cytosol	Binds irreversibly to the 30S subunit of the ribosome, causing protein mistranslation.	(Davis 1987, Ramirez and Tolmasky 2010)
Polymyxin B	Outer/inner membrane	Binds and destabilises lipopolysaccharides in the outer membrane, leading to self-promoted uptake and destabilisation of the inner membrane.	(Zavascki, Goldani et al. 2007)

Lysozyme	Peptidoglycan	Cleaves the glycosidic bond between N-acetylmuramic acid and N-acetylglucosamine in existing peptidoglycan, weakening the cell wall.	(Jollès and Jollès 1984, Ellison and Giehl 1991)

Table 4.1 A selection of effective antibiotics against gram-negative bacteria, summarising their targets and mechanisms of action.

These four antibiotics were chosen to reflect possible targets for nanoparticles: the lipopolysaccharides and outer membrane as first point of contact (polymyxin B), disruption of the peptidoglycan cell wall (ampicillin and lysozyme), and internal processes (kanamycin). To create the atlas the effects of these drugs with *E. coli* must be characterised.

4.2.3 Characterising bacteria/antibiotic interactions

The first step in studying the interactions of drugs with bacteria is in ascertaining whether cell viability, the ability of a cell to grow and divide, is affected. If a drug or nanoparticle affects the viability of a bacterium this can be measured using a number of established protocols (Table 4.2).

Protocol	Mechanism	References
MIC/MBC	Determines the minimum inhibitory/bactericidal concentration of a drug by optically determining bacterial growth over a range of drug concentrations in solid/liquid media.	(Andrews 2001, Murray 2007)
Kirby-Bauer disk diffusion	Measures the zone of inhibition of bacterial growth on solid media caused by a disk impregnated with a drug on the growth surface.	(Murray 2007)
Membrane leakage assay e.g. LIVE/DEAD® *Bac*Light™	A staining technique testing for damaged cell membranes due to leakage of cytoplasmic components or the presence of stains only internalised through compromised cell membranes.	(Boulos, Prévost et al. 1999, Riccardi and Nicoletti 2006)

Table 4.2 Common protocols used to measure bacterial susceptibility to a drug.

These protocols have been used both for drug and nanoparticle toxicological studies. Kim, Lee et al. (2006) synthesised 88 ± 10 nm diameter silicon dioxide nanoparticles coated with < 10 nm diameter copper nanoparticles, and tested the susceptibility of *Staphylococcus aureus* (*S. aureus*), *E. coli*, *Enterobacter cloacae* (*E. cloacae*), *Penicillium citrinium* and *Candida albicans* using the disk diffusion method. They reported measurable antibacterial activity against *E. coli*, which decreased as the copper nanoparticles aggregated at higher copper concentrations.

Ping, Huimin et al. (2007) fabricated 60 ± 30 nm diameter iron oxide core-silver shell nanoparticles and measured their antibacterial properties on *Staphyloccus epidermidis* (*S. epidermidis*), *Bacillus subtilis* (*B. subtilis*) and *E. coli via* MIC and flow cytometry (FCM). MIC values for all species were obtained above 60-70 μg/ml, and FCM using the propidium iodide (PI) dye suggested that the nanoparticles affected cell permeability.

Jones, Ray et al. (2008) investigated the antibacterial activity of ZnO nanoparticles on *S. aureus*, *S. epidermidis*, *Streptococcus pyogenes* (*S. pyogenes*), *Eneterococcus faecalis* (*E. faecalis*), *B. subtilis* and *E. coli* using growth curves measured with UV-Vis spectroscopy. They found that smaller nanoparticles (8 nm diameter) inhibited growth more than larger nanoparticles (50-70 nm), and that ambient UV light photoactivated the ZnO nanoparticles in particular.

Ruparelia, Chatterjee et al. (2008) reported the toxicity of silver (3 ± 1 nm diameter) and copper (9nm ± 1 diameter) nanoparticles on *E. coli*, *B. subtilis* and *S. aureus*. They obtained MIC, MBC, growth curves and disk diffusion zones of inhibition for each microorganism and nanoparticle, reporting strain-specific sensitivities.

Sondi and Salopek-Sondi (2004) combined CFU counts and growth curves showing the antibacterial action of 12 nm diameter silver nanoparticles against *E. coli* with TEM, SEM

and EDX. They reported the incorporation and penetration of the nanoparticles into the bacteria cell membranes by imaging washed and fixed cells.

Pal, Tak et al. (2007) studied the shape-dependent effect of silver nanoparticles against *E. coli.* Growth rates and CFU counts of cultures exposed to rod, spherical and triangular shaped nanoparticles were obtained and cell samples were stained and examined with energy-filtering TEM. The authors observed damage to cell membranes.

Siddhartha, Tanmay et al. (2007) reported antibacterial effects of 10-15 nm diameter silver nanoparticles on *E. coli, S. aureus,* and *Salmonella typhus (S. typhus)* using CFU counts, growth curves and TEM. They reported perforation of the cell wall and profiles of tyrosine phosphorylated proteins were also obtained to investigate any effects on bacterial signal transduction. *E. coli* underexpressed these proteins, which may have led to the inhibition of cytoplasmic enzymes such as RNA polymerase, key for bacterial growth.

Liu, Wei et al. (2009) described the antibacterial activity of single-walled carbon nanotubes on *E. coli, Pseudomonas aeruginosa (P. aeruginosa), S. aureus and B. subtilis* using CFU counts, LIVE/DEAD® *Bac*Light™, SEM and AFM. They visualised the carbon nanotubes acting as “nano darts”, piercing the cell membranes and affecting softer bacteria to a greater degree. A year later they used AFM to ascertain that the accumulation of nanotubes on the cell surface rather than individual nanotubes was responsible for the reported antibacterial action, with the stiffness of the cells reducing over time as a result of damage to the cell wall complex (Liu, Ng et al. 2010).

Lee, Kim et al. (2008) examined the effects of 10-80 nm diameter zero-valent iron nanoparticles on *E. coli* in the presence and absence of air using CFU counts and TEM. Morphological changes in cells which had been fixed, dehydrated, embedded, cured,

sectioned and stained included membrane damage leading to leakage of intracellular contents.

Lok, Ho et al. (2006) undertook proteomic analysis of *E. coli* exposed to 9 nm diameter silver nanoparticles after confirming antibacterial effects *via* growth curves. Two-dimensional electrophoresis and mass spectroscopy revealed an accumulation of membrane protein precursors and dissipation of proton motive force after treatment with silver nanoparticles, suggesting a membrane-targeting antibacterial mechanism.

Hwang, Lee et al. (2008) used recombinant stress-specific bioluminescent *E. coli* to monitor oxidative, membrane and DNA damage caused by 10 nm diameter silver and gold nanoparticles. No effects were measured for gold nanoparticles, but silver nanoparticles induced membrane and oxidative damage.

None of these techniques are readily comparable, and none refer to the established body of knowledge concerning the interactions of antibiotic drugs to bacteria. TEM and SEM studies require substantial sample manipulation (Sondi and Salopek-Sondi 2004, Pal, Tak et al. 2007, Siddhartha, Tanmay et al. 2007). Differences in cell cultures, growth media and ultimately the techniques themselves (e.g. requiring fluorescent staining or recombinant plasmids) make it impossible to extract comparative data (Ping, Huimin et al. 2007, Hwang, Lee et al. 2008).

The approach presented in this thesis is the creation and use of a comparative atlas of the effects of known drugs on cells. Using *E. coli,* three characterisation techniques were selected to measure these effects:

1. Kirby-Bauer disk diffusion assays to establish antibacterial effect;
2. Cell population growth curves of *E. coli* response to the antibiotic in question, and
3. Morphological characterisation by AFM.

Disk diffusion assays and growth curves are well established techniques in microbiology for assessing susceptibility and monitoring growth kinetics of bacterial cultures (Murray 2007). AFM is well suited to imaging changes to cell surfaces without the sample manipulation required in TEM/SEM (Müller and Dufrêne 2011). The overall details for these techniques and specific considerations for the atlas are now described.

4.3 Materials and methods

4.3.1 Disk diffusion assays

Establishing a bactericidal effect is the first characterisation step. Disk diffusion assays were conducted as described in Section 2.3.2.3. If no susceptibility was measured (no zone of inhibition) at the highest concentration of drug available, the process was terminated.

4.3.2 Cell population growth curves

Having established a bactericidal effect, growth curves of cell cultures were obtained following Protocol 2.1 (Section 2.3.2.1). Any deviations from control curves measured in triplicates were recorded, and samples drawn for characterisation with AFM.

4.3.3 Morphological characterisation with AFM

Imaging individual bacteria from growth curve samples with AFM provides not just a qualitative image of cell topography, but also the acquisition of quantitative metrics due to the three-dimensionality (XYZ) of data obtained. Amplitude modulation AFM using Olympus AC240 ($k = 2\ Nm^{-1}$) silicon cantilever tips in air was conducted for all samples. The size of the scan area was usually 256x256 pixels at a scan rate of 2 Hz. Sample preparation for AFM is described in detail in the following section.

4.4 Results and discussion

4.4.1 Development of the methodology

The comparative nature of the proposed atlas required careful implementation of the characterisation techniques used, so that future experiments could replicate the experimental conditions used and allow for robust comparison.

4.4.1.1 Cell population growth curves

Two experimental parameters in particular were kept constant during growth curve experiments:

1. Stoichiometry: the initial number of cells present when the drug is added;
2. Growth phase of the cells when the drug is added: at different growth phases (i.e. lag, exponential, stationary or death) bacteria will be in different metabolic states and respond distinctly to the presence of a drug (Rolfe, Rice et al. 2012).

$\boldsymbol{t_0}$ (min) was defined as the time point when a drug is added to a culture, at a turbidity of 0.2 (A.U.) (equal to 3.4×10^7 CFU/ml). This corresponded to the beginning of the exponential growth phase, when bacteria are doubling at a constant rate.

The following information was then obtained from the growth curve:

1. Incubation time: how rapidly any effect on the cell culture occurs compared to a control culture. This was defined as the time between $\boldsymbol{t_0}$ and the first noticeable deviation from the control growth at $\boldsymbol{t_1}$. When additional or multiple effects occur they are assigned a value of $\boldsymbol{t_2}, \boldsymbol{t_3}$ …
2. Recovery time: the time taken for bacteria to recover, if applicable, from the addition of a drug;

3. Cell lysis: whether the number of bacteria decreases compared to a control culture;
4. Cell growth arrest: whether the number of bacteria remains stationary over a sustained period of time compared to the control culture.

Samples were drawn for any significant deviation observed from control cultures and imaged under AFM.

4.4.1.2 Sample preparation for AFM

Initial attempts at characterising cell morphology with AFM involved the aliquoting of *E. coli* samples in Luria-Bertani (LB) growth medium directly from cell cultures onto glass slides. The slides were dried under a laminar flow hood and imaged. The complexity of LB, which contains derivatives of casein, yeast extract and ≈170 mM sodium chloride, frustrated the identification and measurement of the *E. coli* cells (Figure 4.3).

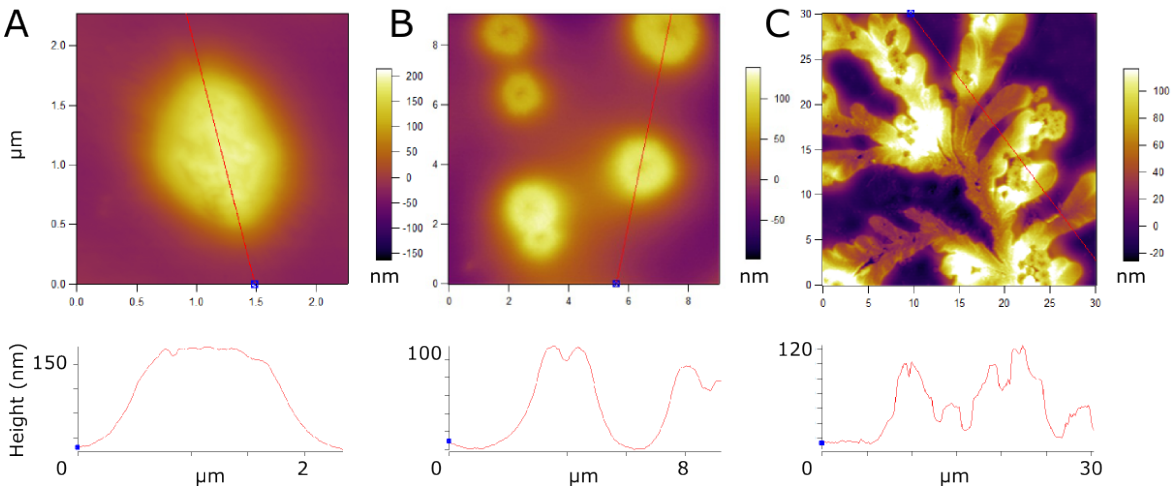

Figure 4.3 AFM topography images obtained of **(A)** an *E. coli* bacterium in LB and **(B,C)** LB-only dried on glass. Corresponding Z profiles of height cross-sections are displayed underneath. Cell morphology was affected by the presence of high concentration of salts, and LB itself contained micro-scaled matter which dried in a fractal formation making the identification of bacteria non-trivial.

A large proportion of *E. coli* imaged appeared as in Figure 4.3A: the characteristic rod shape of the bacteria was distorted, most likely due to the high concentration of salts contained in the medium, affecting the osmotic turgor pressure responsible for the shape

of the cells (Slonczewski and Foster 2009). Components of casein derivatives and yeast extract were also visible on a micro-scale, making it hard to easily distinguish between any cells that had been affected and the background noise of the medium (Figure 4.3B,C).

A number of approaches to optimise sample preparation for AFM were undertaken, with the aim of maximising the number of identifiable cells while minimising sample manipulation. Washing bacteria three times in ddH_20 and drying on glass removed the LB artefacts, with rod-shaped cells clearly visible, and a lack of large non-bacterial components (Figure 4.4). This common approach improved imaging conditions for the bacteria, but risks removing any cells that are damaged and of interest in this study.

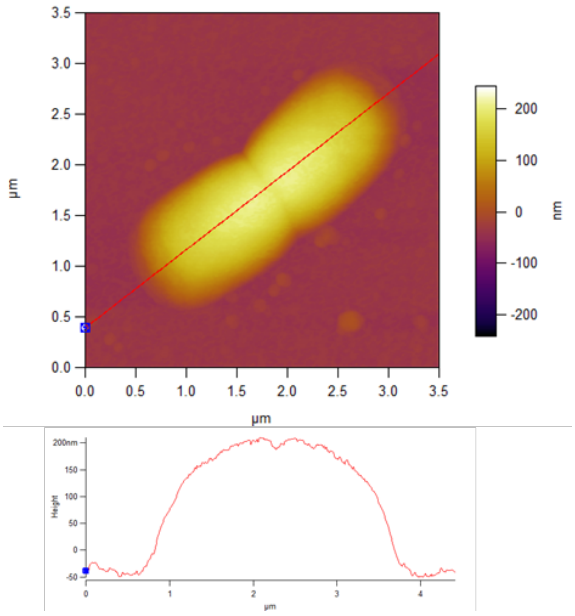

Figure 4.4 AFM topography image of *E. coli* dried on glass after washing in ddH_20, with corresponding Z profile cross-section displayed underneath.

To overcome this problem, Dr. Sonia Trigueros experimented with substrates of agarose on glass. Agarose is a hydrogel commonly used in gel electrophoresis as its pore size (which varies with concentration) allows the diffusion of small to medium sized molecules (e.g. DNA or casein extracts) passively or under an electric potential (Serwer 1983). When aliquots of *E. coli* were deposited on agarose, the superfluous structures from LB were

effectively filtered by absorption, leaving the much larger bacterial cells unaffected (Figure 4.5) (Bolshakova, Kiselyova et al. 2004).

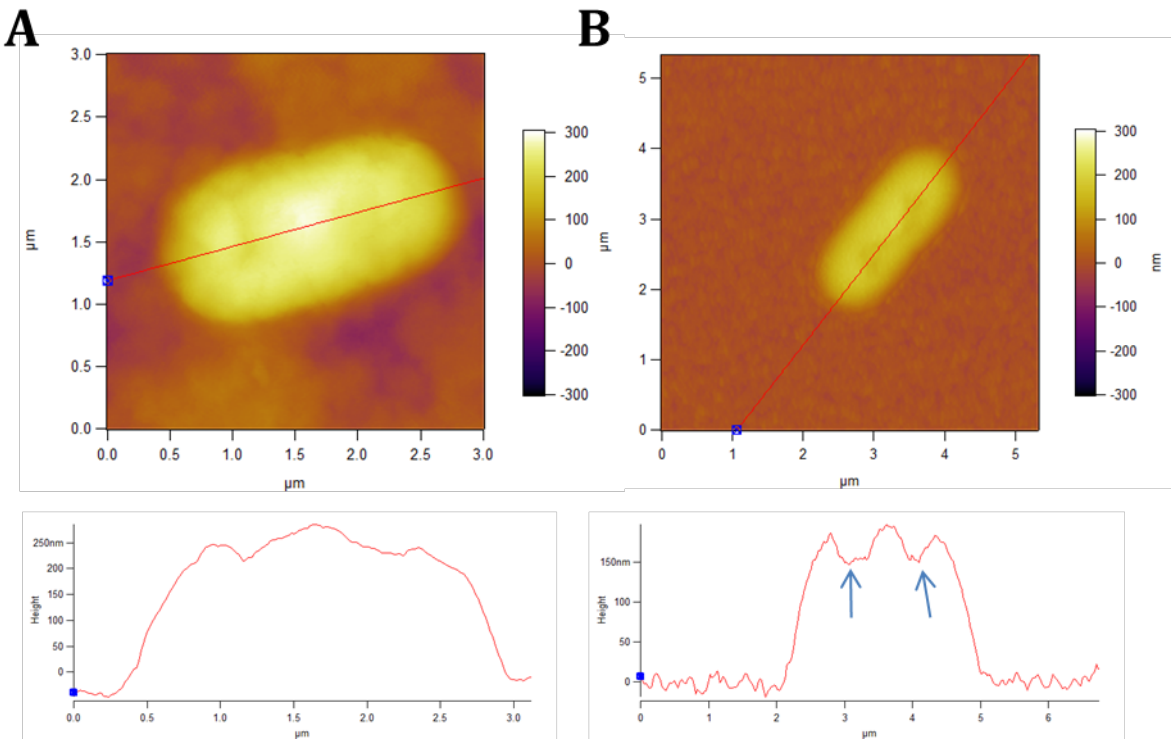

Figure 4.5 AFM topography images and height cross-sections of *E. coli* dried on **(A)** 1% and **(B)** 4% agarose substrates improved cell morphology and minimised extracellular debris. Higher percentages of agarose qualitatively decreased cell heights, in some cases introducing depressed areas on the cell surface, visible in the centre of the bacterium in (B), and highlighted in the corresponding cross section.

We developed the following protocol to image bacteria via AFM on freshly prepared agarose slides (Protocol 4.1).

Protocol 4.1 – Agarose slide preparation for AFM imaging

1. Prepare glass slides with 125 µl ABgene Gene Frame (GEN-100-030C, Fisher Scientific, Leicestershire, UK).
2. Prepare (molten) agarose solution to required concentration (1,2,4% w/v).
3. Pour 500 µl per frame, and cover quickly, expelling excess agarose.
4. Leave to set.
5. When sample is ready, pipette 50 µl cell culture sample onto agarose, tilting at 45° to spread evenly.

6. Leave to dry overnight, covered at room temperature (21 °C).
7. Image the next day.

Varying the concentration of agarose used from 1% to 4% qualitatively affected cell heights, and is discussed in detail in the following sections.

4.4.1.3 **Metrics**

The first two characterisation techniques used for *E. coli* interactions with a drug or nanomaterial provide quantitative ensemble metrics: zones of inhibition (in mm) from disk diffusion assays and incubation times and recovery times (in minutes) from cell population growth curves. In order to quantitatively compare AFM images of individual bacteria, the following metrics describing cell morphology (size and shape) were defined:

a. Average height of an individual bacterium, summed over the whole cell;
b. Width of an individual bacterium, measured across a representative cross-section;
c. Length of an individual bacterium, measured across a representative cross-section;
d. Volume of an individual bacterium, measured over the whole cell;

The most important step in calculating these metrics was in correctly setting the $\mathrm{Z} = 0$ plane (see Section 2.4.4), the plane which defines where the substrate ends and the cell begins. Once this plane is established, the next step is to *mask* the bacterium in question. The mask is the defining two-dimensional area which contains the bacterium, and must not extend onto the substrate as this will skew subsequent metrics calculated (by lowering the average height for example).

As an initial approximation, an iterative mask was available in the manufacturers' software which automatically masked "high" features (Ridler and Calvard 1978). This was

then refined by dilating or eroding the mask a pixel at a time until the mask contour reached $Z = 0$, indicating the end of the bacterium and the beginning of the substrate.

If there were artefacts present in the images, these were removed from the mask manually (Figure 4.6).

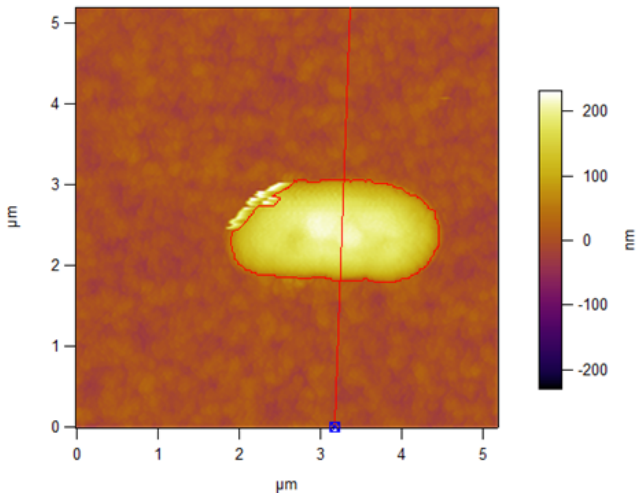

Figure 4.6 AFM topography image of an *E. coli* bacterium on agarose substrate. The red mask defines the cell, with a cross-section defining where the width of the cell is measured. An series of imaging artefacts are visible in the top left corner of the bacterium and have been manually removed from the mask.

Small amounts of noise visible in the top left corner of the bacterium shown in Figure 4.6 were removed by manually drawing and subtracting the area from the mask using the manufacturer's software. Noise at the edge of a feature can be caused by a variety of imaging malfunctions, including feedback errors (the controller fails to stabilise the Z piezo at the correct height due to the abrupt edge) or tip-sample adhesion (if not completely dry, liquid can accumulate at the bottom of features, causing the tip to stick momentarily, affecting the feedback process). If the area affected is small, the effect on metrics in removing it is negligible.

Once the mask was defined, the following quantities were calculated using the masked image:

1. Average height:

$$\bar{z} = \frac{1}{n}\sum_{n} z_n \tag{4.1}$$

where n is the number of data points (pixels) inside the mask and z is the height of each pixel relative to the base plane.

2. Minimum height – the lowest z value in the mask. Useful for checking if the mask extended onto the substrate.
3. Volume – calculated by summing the heights of the masked area and multiplying by the XY area.

To obtain the length and width of a bacterium, a representative cross-section was applied to each mask and measured. The length was obtained by measuring the length of the masked image in a cross-section across the longitudinal part of the bacterium. The width was defined as the perpendicular cross-section, measured across the middle of the cell (Figure 4.7).

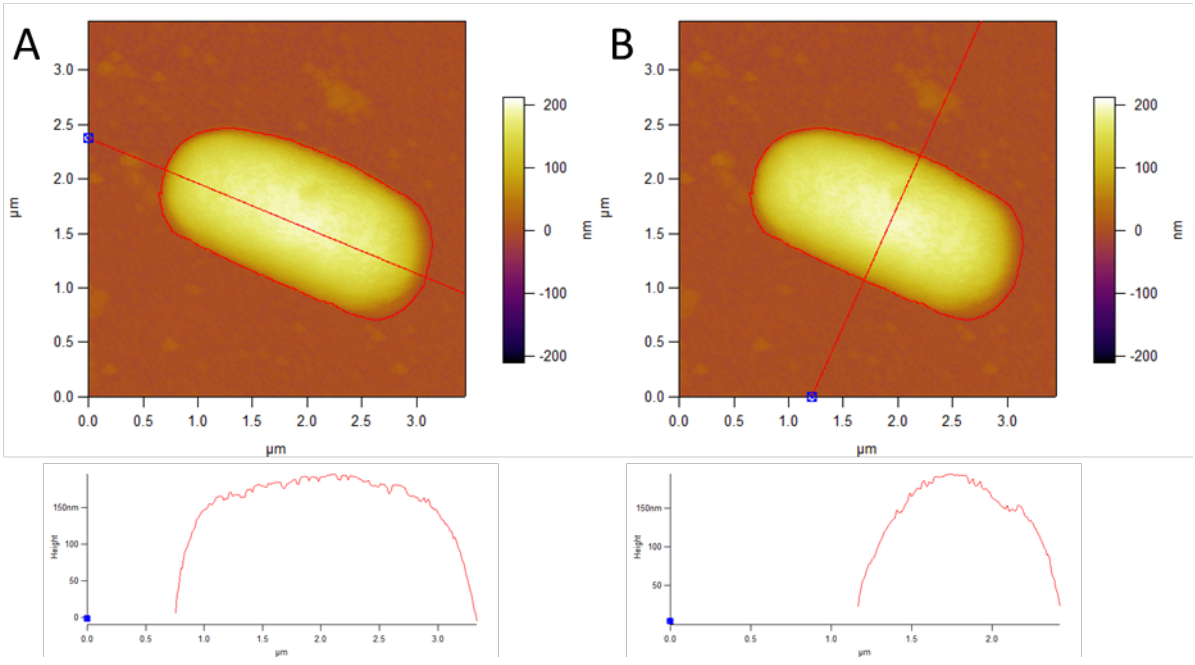

Figure 4.7 AFM topography images of an *E. coli* bacterium on glass. Manually placed cross-sections defining the length **(A)** and width **(B)** are shown. Cell width was determined across the centre of the bacterium.

Cells imaged at the point of, or just after binary division presented an additional challenge, as it was difficult to differentiate two entities from one if they were juxtaposed. To resolve this issue the following was assumed: two cells that have just divided would tend to move away from each other, and have either a measurable distance between each other or a different orientation (Figure 4.8).

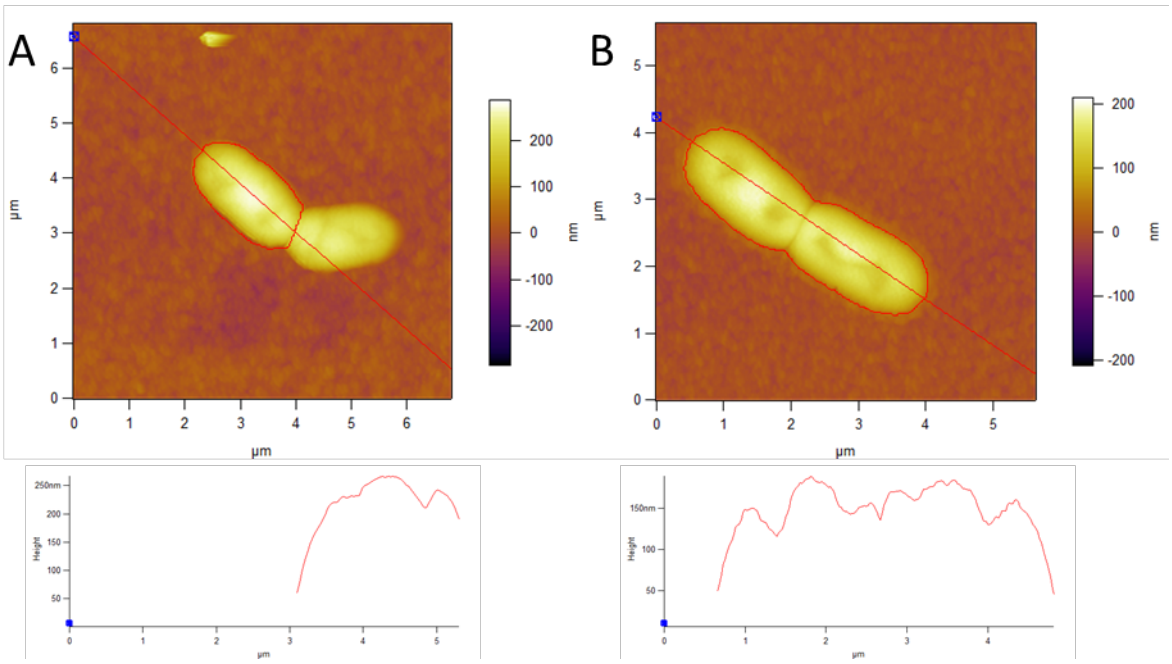

Figure 4.8 AFM topography images of *E. coli* on agarose substrate, with cross-sections defining length below. **(A)** two individual bacteria after division, **(B)** one bacterium very close to completing cell division.

The height, length, width and volume of each cell were defined as the quantitative metrics used for morphological characterisation by AFM for control cells and cells affected by a drug or nanomaterial.

4.4.1.4 **Control cells**

Before characterising the effect of the selected antibiotics on *E. coli*, the effects of sample preparation, in particular the concentration of the agarose substrate used, were investigated on control cells.

4.4.1.4.1 Cell morphology

E. coli control cells in exponential growth phase were aliquoted directly onto 1%, 2% and 4% agarose slides as in Protocol 4.1, and onto glass after washing in ddH_20. A qualitative discussion of cell morphology is conducted before applying the quantitative metrics defined in the previous section.

4.4.1.4.1.1 Glass, washed

E. coli cells which had been washed of their medium and dried on glass appeared rod-shaped as in Figure 4.9. The substrate had a root mean squared (RMS) roughness of approximately 2 nm. This low value of roughness reflects the smooth surface of the glass.

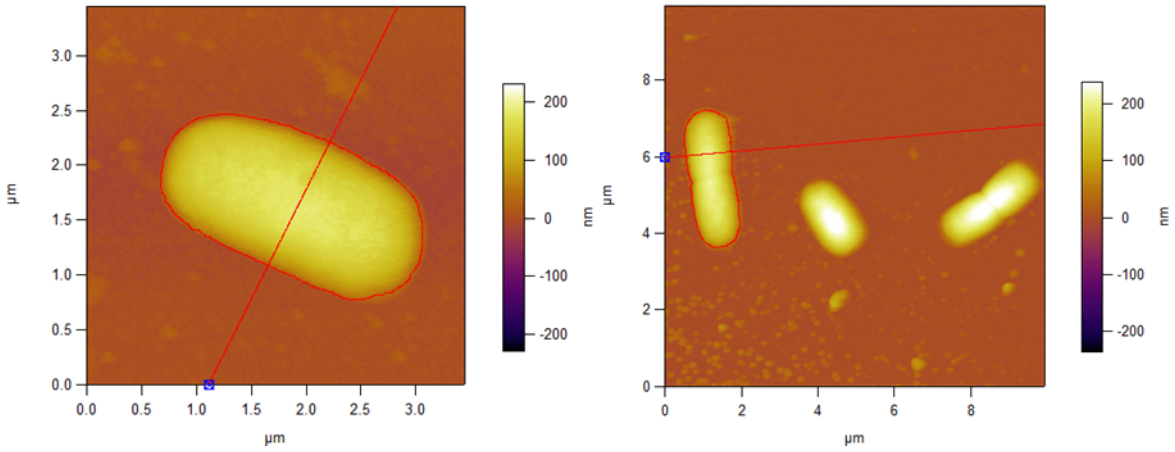

Figure 4.9 Representative AFM topography images of *E. coli* washed three times with ddH_2O and dried on glass. Cross-sections indicate where cell widths were determined.

4.4.1.4.1.2 Agarose 1%

E. coli cells on 1% agarose slides were rod-shaped, exhibiting small depressions on the cell surface (Figure 4.10). The substrate had an RMS roughness of approximately 15 nm, reflecting the cross-linked polysaccharide structure of the hydrogel (Serwer 1983).

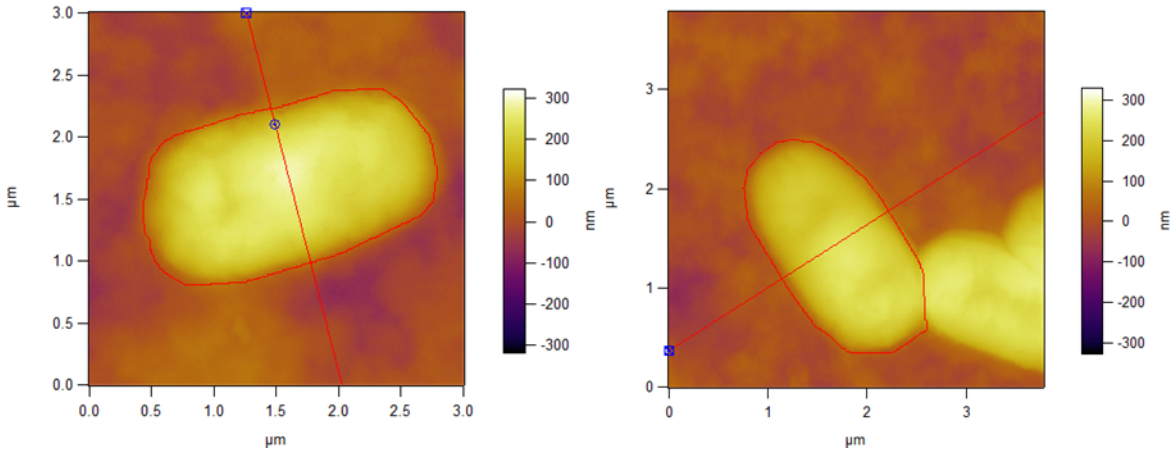

Figure 4.10 Representative AFM topography images of *E. coli* on a 1% agarose substrate. Cross-sections indicate where cell widths were determined. Small depressions in the cell surface are visible.

4.4.1.4.1.3 Agarose 2%

Cells sampled on 2% agarose slides were noticeably lower in height than samples on 1% agarose, with an increase in the depressed areas on cell surfaces (Figure 4.11). The substrate had an RMS roughness of approximately 10 nm.

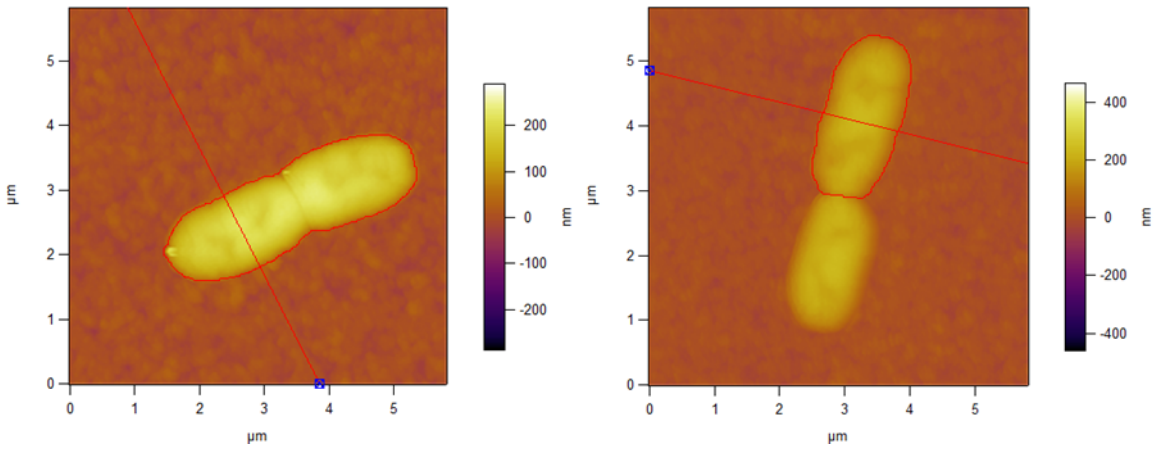

Figure 4.11 Representative topography images of *E. coli* on a 2% agarose substrate. Cross-sections indicate where cell widths were determined. More prominent depressions on the cell surface were observed compared to 1% agarose substrates.

4.4.1.4.1.4 Agarose 4%

Finally, cells sampled on 4% agarose slides exhibited marked areas of depression, probably due to the absorption of water by the higher concentration agarose substrate (Figure 4.12). The substrate had an RMS roughness of approximately 6 nm.

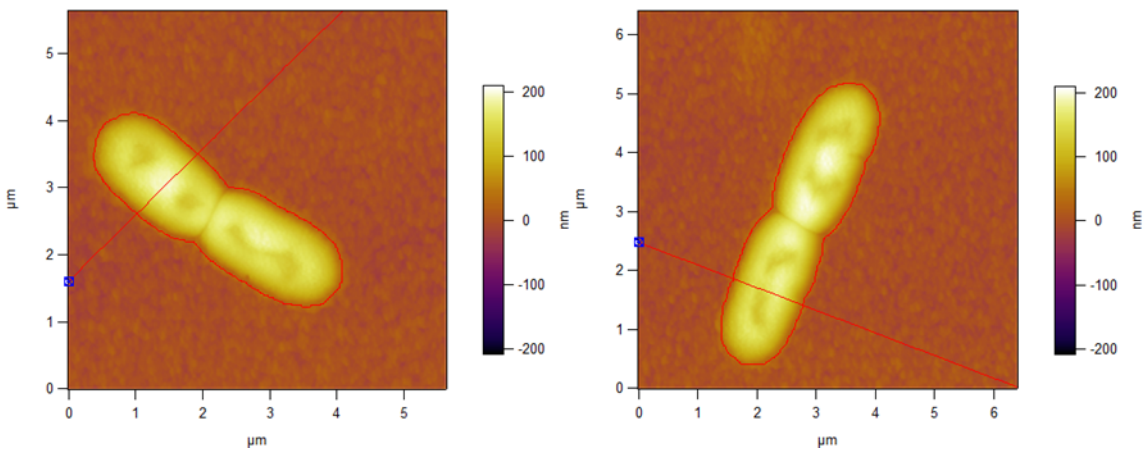

Figure 4.12 Representative topography images of *E. coli* on a 4% agarose substrate. Cross-sections indicate where cell widths were determined. More prominent depressions on the cell surface were observed compared to 1% and 2% agarose substrates.

Higher concentrations of agarose resulted in smoother, more rigid substrates and greater absorption of material from the medium and the cells themselves. An increase in depressions on the cell surface was observed as a function of agarose concentration. A quantitative analysis of cell morphology was conducted to select the final concentration used for characterisation experiments.

4.4.1.4.2 Quantitative AFM characterisation

To quantify the observed morphological changes for different substrates, the metrics defined in Section 4.4.1.3 were calculated. Figure 4.13 shows boxplot summaries of height, width, length and volume distributions for the four control samples: *E. coli* on glass (washed in ddH_20), 1%, 2% and 4% agarose substrates.

The heights of representative cells dried on glass were distributed evenly between 127 and 146 nm, with a median of 136 nm and mean of 136 ± 2 nm (one standard error of the mean). Widths were distributed between 1.19 and 1.34 µm, with a median of 1.30 µm and mean of 1.28 ± 0.01 µm. Lengths were distributed between 2.2 and 3.8 µm, with a median of 3.3 µm and mean of 3.1 ± 0.2 µm. Cell volumes ranged from 0.34 to 0.67 μm^3, with a median of 0.51 μm^3 and mean of 0.50 ± 0.03 μm^3.

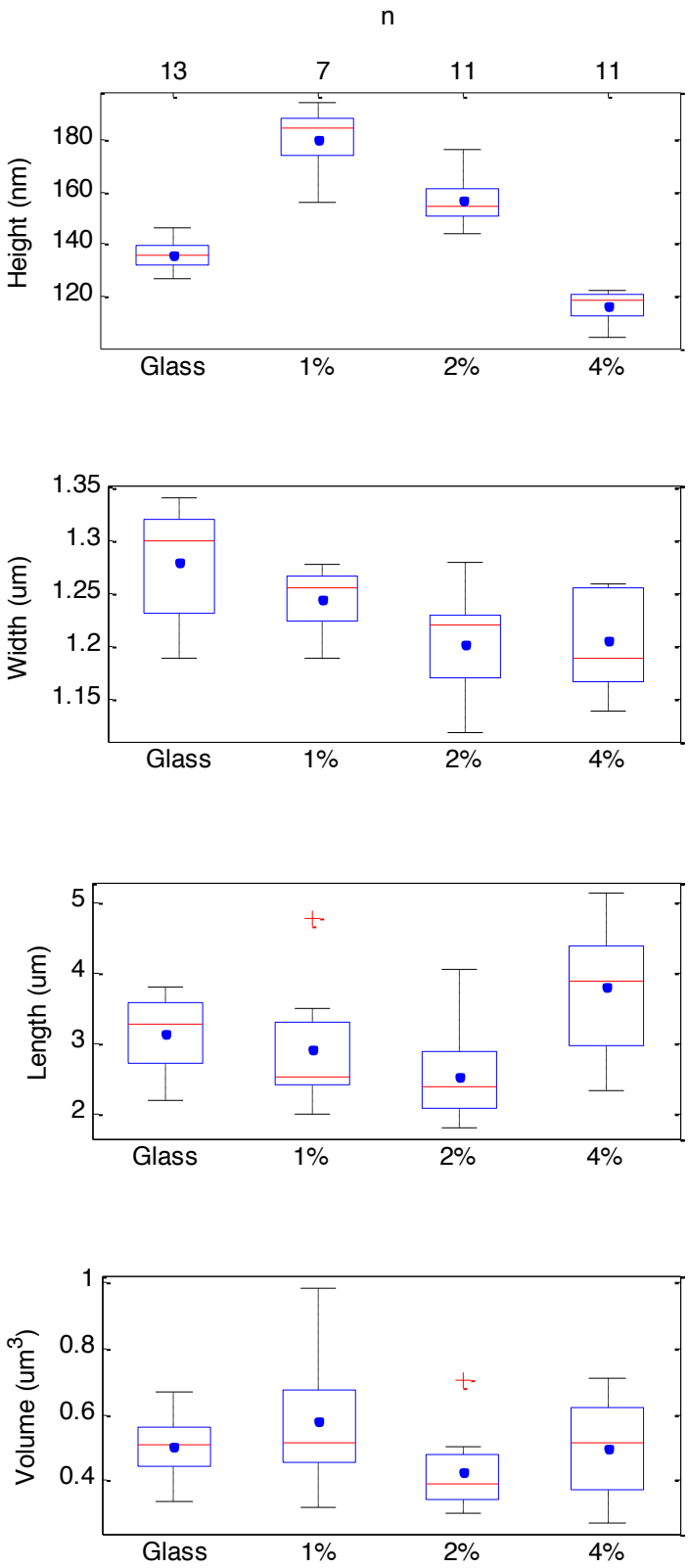

Figure 4.13 Boxplot representation of AFM metrics of control cells. For each control, height, width, length and volume distributions are displayed. Boxplots display mean as dot, median as red horizontal line, and the interquartile range (25th to 75th percentile) as a box. Whiskers extending up to a maximum of 1.5*IQR beyond or beneath the 75th & 25th quartiles respectively reflect the range of the data. Outliers outside this range are represented as red crosses. At the top of the figure the sample size n is displayed.

Cells dried on 1% agarose had heights distributed between 156 and 194 nm, with a median of 184 nm and mean of 180 ± 5 nm. Cell widths ranged between 1.19 and 1.28 μm with a median of 1.26 μm and mean of 1.24 ± 0.01 μm. Lengths were distributed between 2.0 and 3.5 μm (with a single outlier at 4.8 μm), with a median of 2.5 μm and a mean of 2.9 ± 0.4 μm. Cell volumes varied between 0.32 and 0.98 μm^3, with a median of 0.52 μm^3 and mean of 0.58 ± 0.08 μm^3.

2% agarose samples had cell heights between 144 and 176 nm, with a median of 155 nm and a mean of 157 ± 3 nm. Cell widths ranged from 1.12 to 1.28 μm, with a median of 1.22 μm and mean of 1.20 ± 0.02 μm. Cell lengths ranged from 1.8 to 4.1 μm, with a median of 2.4 μm and mean of 2.5 ± 0.2 μm. Cell volumes were distributed between 0.30 and 0.50 μm^3 (with a single outlier at 0.71 μm^3), with a median of 0.39 μm^3 and mean 0.42 ± 0.03 μm^3.

4% agarose samples contained cells with heights distributed between 105 and 122 nm, with a median of 119 nm and mean of 117 ± 2 nm. Cell widths ranged from 1.14 to 1.26 μm, with a median of 1.19 μm and mean of 1.21 ± 0.01 μm. Lengths were distributed between 2.3 and 5.1 μm, with a median of 3.9 μm and mean of 3.8 ± 0.3 μm. Cell volumes ranged from 0.28 to 0.71 μm^3, with a median of 0.52 μm^3 and mean of 0.50 ± 0.04 μm^3.

Pair-wise post-hoc analysis of variance (ANOVA, full results in Appendix B) found significant ($p < 0.05$) differences between heights for each pair of samples analysed. Within agarose samples, cell height decreased as a function of increasing agarose percentage. Cells imaged on glass were lower than those imaged on 1% and 2% agarose, and higher than those imaged on 4% agarose. These observations reflect the complex absorption properties of the agarose substrate: at low concentrations, the agarose

hydrogel hydrates cells more than the dry glass surface, and at high concentrations agarose absorbs more liquid from the cells than drying on glass.

For cell widths ANOVA revealed significant differences between 2% and glass, and 4% and glass substrates, which both saw reductions compared to glass. The higher concentrations of agarose reduced cell widths, most likely due to increased absorption at the substrate surface.

ANOVA revealed significant differences between the lengths of 2% and 4% agarose samples. Cell length is a function of the cell cycle of the bacteria, which was not synchronised in the cultures studied in this work, and these differences could be due to inherent sampling variability.

Finally, no significant differences between cell volumes were observed. As the volume depends on the length, width and height of the cell, sampling variability in cell lengths may have counterbalanced changes in height and/or widths.

Table 4.3 summarises the metrics obtained for the four control groups.

	n	Height (nm)	±	Width (µm)	±	Length (µm)	±	Volume (µm^3)	±
Glass	13	136	2	1.28	0.01	3.15	0.15	0.50	0.03
1%	7	180	5	1.24	0.01	2.91	0.36	0.58	0.08
2%	11	157	3	1.20	0.02	2.52	0.20	0.42	0.03
4%	11	117	2	1.21	0.01	3.79	0.28	0.50	0.04

Table 4.3 Controls summary. Data shown as mean values ± standard error of mean.

Washing cells in ddH_20 and imaging on glass represented an unacceptable level of sample manipulation as previously discussed. Agarose was chosen as a substrate that allowed aliquoting of cells directly from cell cultures in the LB growth medium. Amongst the agarose samples, the 2% concentration resulted in the least extreme cell heights and widths across all the agarose concentrations tested, and was selected as the optimum substrate for experiments with *E. coli* cells in LB.

4.4.2 Characterisation of *E. coli* with antibiotics

Having selected a 2% agarose concentration for *E. coli* in LB, and gathered data on the morphological metrics for control cells, the effects of the antibiotics previously selected were examined. Disk diffusion assays, cell growth curves and cell morphology characterisation by AFM were conducted according to the methodology.

4.4.2.1 Disk diffusion assays

Disk diffusion tests were conducted for each of the antibiotics selected, apart from lysozyme, which was stored in 50% glycerol and unlikely to diffuse in the agar medium (Table 4.4).

Species	Concentration (μg)	Zone of inhibition (mm)	± (mm)
Kanamycin	10.0	14.8	0.3
Ampicillin	10.0	28.4	0.5
Polymyxin B	8.0	15.8	0.3

Table 4.4 Zone of inhibitions as a function of antibiotic concentration. Errors represent one standard error of the mean for triplicate experiments.

The zone of inhibition reflects the antibiotic strength of a drug. The areas nearest the disks have highest concentrations of drug, and as the drugs diffuse out the concentration decreases. The point when the concentration is too low to exert an antibacterial effect marks the border of the zone of inhibition: a larger zone of inhibition represents a more powerful antibiotic (see Section 2.3.2.3). The ability of a drug to diffuse will also affect the zone of inhibition – larger drug molecules will diffuse less leading to smaller zones of inhibition. In this case all drugs tested were small molecules which easily diffused. Ampicillin exhibited the largest zone of inhibition, followed by polymyxin B and kanamycin.

4.4.2.2 Cell population growth response

Growth curves of *E .coli* DH5α in LB were obtained in triplicate for each of the antibiotics selected. The concentration of antibiotic used was typically 5-10 times the reported minimum inhibitory concentrations, to ensure a visible effect. The growth curves were labelled at characteristic time points $\boldsymbol{t_0}, \boldsymbol{t_1}, \boldsymbol{t_2}$ corresponding to features observed, with $\boldsymbol{t_0}$ marking the point when the drug was added to the culture as described in Section 4.3.2. Samples were then selected at the relevant time points for AFM imaging.

4.4.2.2.1 Kanamycin

Kanamycin causes mistranslation during protein synthesis in the cytosol, after passing through the outer and inner cell membranes in an energy-dependent mechanism affecting membrane permeability (Table 4.1). Cell population growth response to kanamycin is shown in (Figure 4.14). At $\boldsymbol{t_1}$ (30 minutes after $\boldsymbol{t_0}$), the number of cells remained similar to those at the previous sampling point, while the control cells continued to grow exponentially. Prolonged incubation ($\boldsymbol{t_2}$) did not result in recovery or a significant decrease in cell numbers.

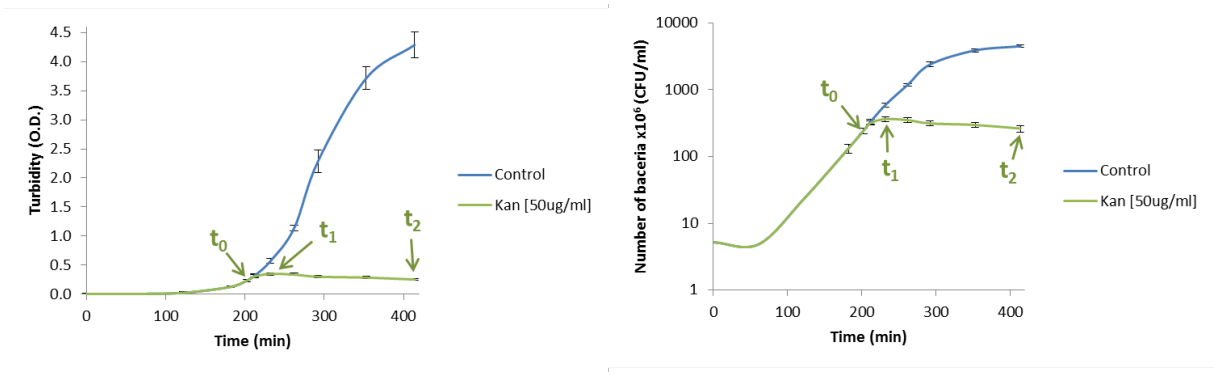

Figure 4.14 Triplicate growth curves for kanamycin at a concentration of 50 µg/ml. The left hand graph plots turbidity (optical density) values as a function of time, and the right hand graph plots the equivalent number of cells on a log scale as a function of time. Error bars represent compound experimental (equipment) errors and random (triplicate) errors. For low values of turbidity (and number of cells) equipment errors dominate. $\boldsymbol{t_0}$ and $\boldsymbol{t_1}$ correspond to the initial addition of kanamycin and the first measured effect respectively. $\boldsymbol{t_2}$corresponds to the final experimental point. At $\boldsymbol{t_1}$ the growth of cells was effectively inhibited compared to the control sample.

Kanamycin exhibited the following characteristics:

- Incubation time of at least 10 minutes;
- Stationary phase (no significant reduction in number of cells);
- No recovery.

These results confirm the internal mechanism of kanamycin as a disruptor of protein synthesis: the incubation time reflects the time taken to traverse the outer and inner membranes and bind to the target ribosomes. The stationary phase arises from the inability of the bacteria to grow effectively once proteins are mistranslated. The lack of lysis indicates that increased cell membrane permeability was not a predominant cause of cell death: over time it is expected that cell membrane proteins would also be affected causing a breakdown in the cell membrane and lysis, though this was not observed in the timescales used in this study.

4.4.2.2.2 Ampicillin

Ampicillin targets penicillin-binding proteins (PBP) responsible for cross-linking newly synthesised peptidoglycan in the cell wall (Table 4.1). Cell population response to ampicillin was rapid and significant (Figure 4.15). At $\boldsymbol{t_1}$ (30 minutes after $\boldsymbol{t_0}$), the number of cells decreased substantially to below the number of cells at $\boldsymbol{t_0}$. Prolonged incubation did not result in recovery or a further significant decrease in cell numbers. At the end of the experiment ($\boldsymbol{t_2}$) cell debris was visible in the culture flasks.

Ampicillin exhibited the following characteristics:

- Rapid effect (cells were affected almost immediately after $\boldsymbol{t_0}$).
- Bacteriolytic effect (number of cells at $\boldsymbol{t_1}$ less than the number of cells at $\boldsymbol{t_0}$).
- No recovery.

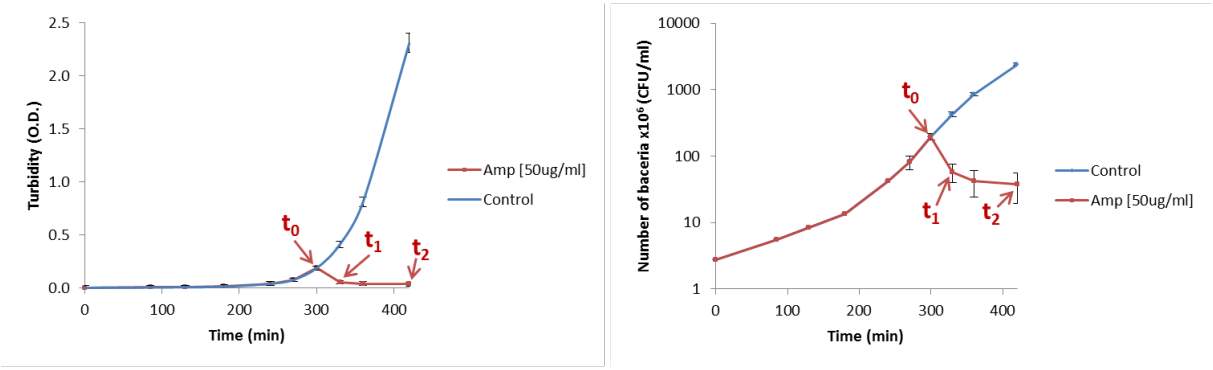

Figure 4.15 Triplicate growth curves for ampicillin 50 µg/ml. Turbidity and number of bacterial cells are represented on the left and right hand graphs respectively. t_0 and t_1 correspond to the initial addition of ampicillin and the first measured effect respectively. t_2 indicates the point where no further effects are measured. At t_1 a rapid reduction in cell numbers was observed corresponding to cell lysis.

These results demonstrate that ampicillin was able to rapidly traverse the outer membrane and reach its target. Cells at t_0 were in exponential growth phase, inserting large amounts of newly synthesised peptidoglycan into the cell wall to sustain growth. Ampicillin interferes with penicillin-binding proteins responsible for peptidoglycan synthesis, preventing the cross-linking of new peptidoglycan strands and triggering cell wall degradation (Kitano and Tomasz 1979).

4.4.2.2.3 Polymyxin B

Polymyxin B targets the lipopolysaccharides (LPS) attached to the outer membrane of the bacteria, resulting in a destabilisation of the membrane, self-promoted uptake and a destabilisation of the inner membrane (Table 4.1). Cell population response to polymyxin B is shown in Figure 4.16. t_1 occurred rapidly (10 minutes) after drug addition, and resulted in a lytic phase lasting until t_2 after which the number of cells remained similar to those at the previous sampling points. Cells did not recover.

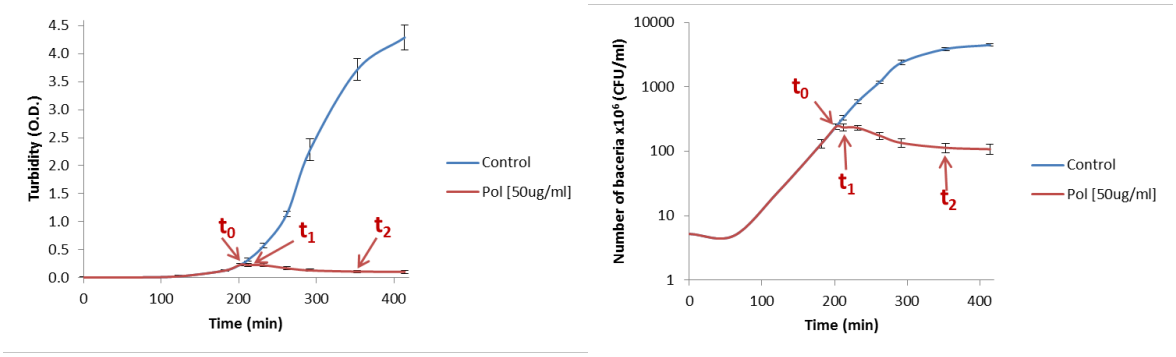

Figure 4.16 Triplicate growth curves for polymyxin B 50 µg/ml. Turbidity and number of bacterial cells are represented on the left and right hand sides respectively. Error bars are as previously described. $\boldsymbol{t_0}$ is when the drug was added to the cultures. $\boldsymbol{t_1}$ corresponds to the first measured effect (10 minutes after $\boldsymbol{t_0}$). $\boldsymbol{t_2}$ (90 minutes after $\boldsymbol{t_0}$) corresponds to the end of the initial lytic effect, and the beginning of a stationary phase.

Polymyxin B exhibited the following characteristics:

- Rapid effect (low $\boldsymbol{t_1}$).
- Lytic effect from $\boldsymbol{t_1}$ to $\boldsymbol{t_2}$ (reduction in number of cells).
- Stationary phase after $\boldsymbol{t_2}$ (no further significant reduction in cells).
- No recovery.

The rapid effect of polymyxin B can be attributed to its detergent-like nature: it disrupted the outer membrane non-specifically, resulting in a rapid effect on cell viability. The lytic effect was less dramatic than ampicillin, indicating that once bound to its target more time was needed to cause cell lysis. This is likely because polymyxin B does not directly affect peptidoglycan, and the lysis observed was a result of the destabilised membranes of the cell and cell leakage. The stationary phase after $\boldsymbol{t_2}$ supports this theory, as the remaining peptidoglycan structures would still result in UV-Vis scattering at 600 nm, unlike in ampicillin where absorbance was decreased by a factor of 10.

4.4.2.2.4 Lysozyme

Lysozyme directly targets the peptidoglycan cell wall, weakening its existing structure (Table 4.1). Cell population response to lysozyme is shown in Figure 4.17. At $\boldsymbol{t_1}$, there was a momentary “shock” as the number of cells did not increase at the same rate as the

control. This "shock" resulted in an offset to the number of cells compared to the control which was not overcome by the end of the experiment. The eponymous lysis was not observed most likely due to the lack of a chelating agent such as EDTA (Jollès and Jollès 1984) which is required to destabilise the outer membrane and allow the penetration of lysozyme into the periplasmic space where its target is located. The small effect observed has been reported previously for gram negative cells without chelating agents (Ellison and Giehl 1991).

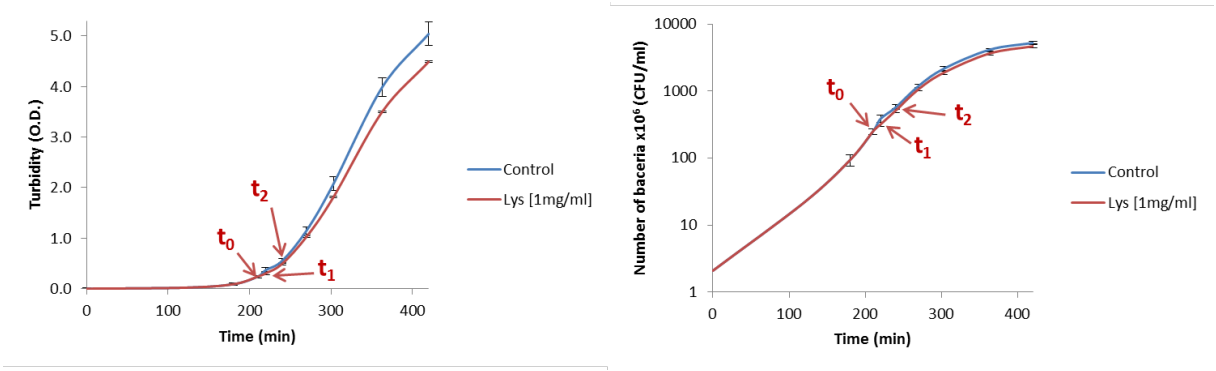

Figure 4.17 Triplicate growth curves for lysozyme 1 mg/ml. Turbidity and number of bacterial cells are represented on the left and right hand sides respectively. Error bars are as previously described. $\boldsymbol{t_0}$ is when the drug was added to the cultures. $\boldsymbol{t_1}$ corresponds to the first measured effect (10 minutes after $\boldsymbol{t_0}$). Recovery is rapid at $\boldsymbol{t_2}$ (20 minutes after $\boldsymbol{t_1}$).

Lysozyme exhibited the following characteristics:

- Rapid initial effect (low $\boldsymbol{t_1}$).
- Small effect (small number of cells affected).
- Quick recovery at $\boldsymbol{t_2}$ (20 minutes after $\boldsymbol{t_1}$).

The initial rapid effect of lysozyme indicates a rapid entry into affected cells, though the number of cells affected was small, with cells recovering rapidly. This is most likely due to the lack of chelating agents such as EDTA, which bind to and destabilise LPS and the outer membrane, but does indicate that lysozyme was able to pass through the outer membrane and affect cells to a limited extent.

The four antibiotics characterised resulted in distinct cell population growth responses according to their targets and mechanisms of action. Immediate effects were observed for non-specific binding of polymyxin B, and delayed effects for ampicillin and kanamycin, which required incubation before binding to their targets. Bacteriolysis was observed where cell integrity was disrupted either due to a breakdown in the cell wall (ampicillin) or the cell membranes (polymyxin). The internal effect of kanamycin resulted in a stationary phase without visible lysis.

Cell population growth curves show ensemble effects: absorbance measurements represent millions of cells. To probe the effect of the antibiotics down to a single bacterium, cell morphology was established with AFM.

4.4.2.3 **Cell morphology**

Cell morphology was characterised by drawing samples from the appropriate cell population growth time points, direct aliquoting onto freshly prepared 2% agarose substrates, drying and imaging under AFM. A qualitative analysis of the resulting images is discussed, before the metrics defined in Section 4.4.1.3 are applied and statistical comparisons made.

4.4.2.3.1 Kanamycin (t_2)

Cells affected by kanamycin were sampled at t_2 (Figure 4.14) and imaged. AFM images of affected cells did not on the whole reveal significant alterations to cell morphology compared to control cells (Figure 4.18). Cells retained their rod shape, with some cells (Figure 4.18B) exhibiting raised poles, possibly inclusion bodies formed due to the aggregation of mis-folded protein synthesised by affected ribosomes (Kopito 2000).

The lack of observed cell wall damage supports the stationary phase observed in Figure 4.14.

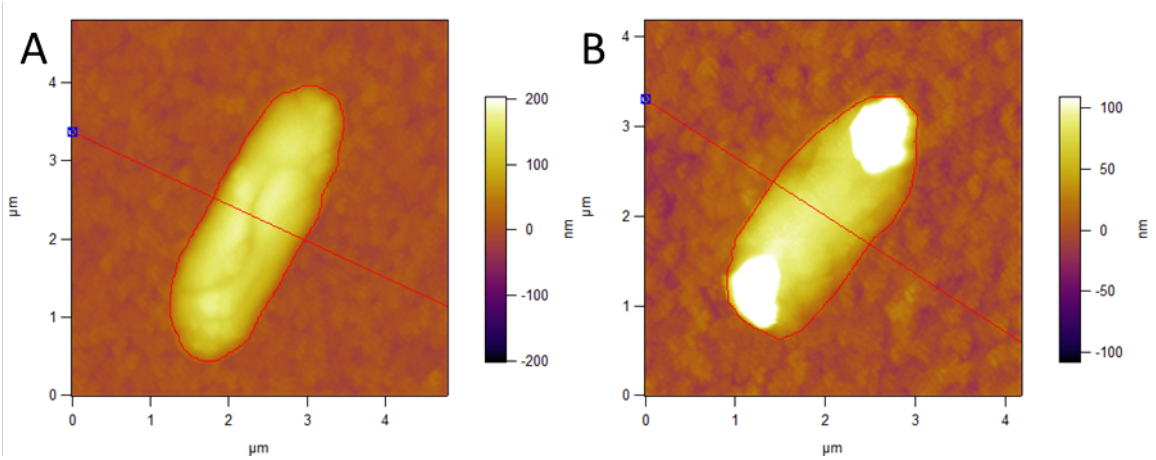

Figure 4.18 Representative AFM topography images for kanamycin affected cells on 2% agarose substrates at t_2. Cells maintained their rod shape **(A)**, with prominent raised poles **(B)** present in ~ 30% of cells imaged. Width measurements were made where cross-sections are shown.

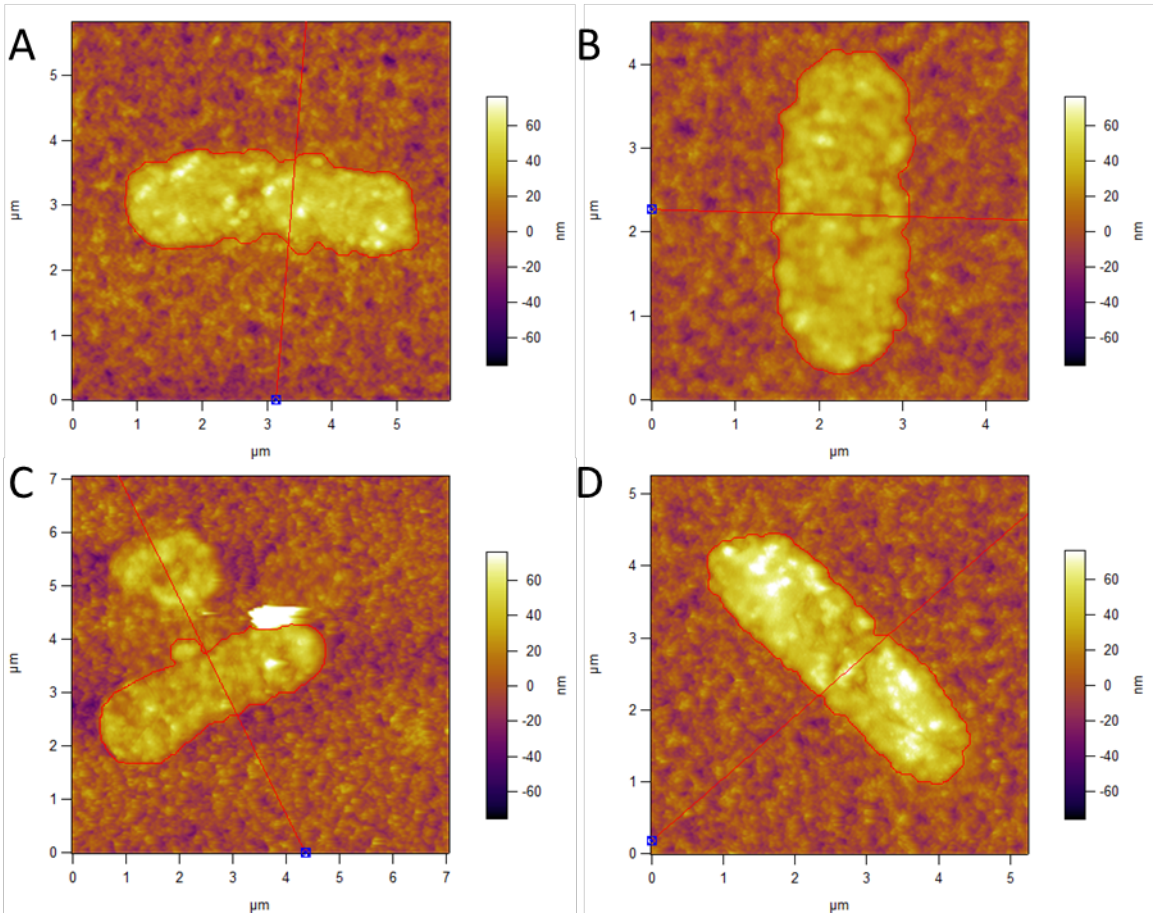

Figure 4.19 Representative AFM topography images for ampicillin-affected cells at t_1**(A,B)** and t_2**(C,D)**. At $t_1$cells had reduced heights and surfaces with large heterogeneity. At $t_2$cells were similarly affected. A small number of spheroplasts were observed (C). Cross-sections indicate where width measurements were taken.

4.4.2.3.2 Ampicillin t_1 and t_2

Cells affected by ampicillin were sampled and imaged at t_1 and t_2 (Figure 4.19). They retained their rod shape but were clearly disrupted, with an apparent decrease in cell height and increase in surface heterogeneity compared to control cells. A number of spheroplasts (Figure 4.19C), bacteria without outer membrane or cell wall, were observed due to the lack of a cell wall to maintain their rod shape (Witholt, Boekhout et al. 1976).

4.4.2.3.3 Polymyxin B t_1 and t_2

Cells affected by polymyxin B were sampled and imaged at t_1 and t_2 (Figure 4.20). At the beginning of lysis (t_1), both affected and unaffected cells were observed. By the end of lysis (t_2) only affected cells were observed. Cells retained their rod-shape, though cell surfaces were more heterogeneous than those observed with ampicillin. Heights appeared greater than with ampicillin, indicating that less cell contents were lost during lysis.

4.4.2.3.4 Lysozyme t_1

Due to the short-lived effect of lysozyme and glycerol medium provided, affected cells were only observed in phase contrast AFM images on glass substrates (Figure 4.21). Phase contrast can be used to visualise differences in material contrast of a sample, and is useful when topography and/or amplitude images are unclear (Cleveland 1998, Paulo and García 2001).

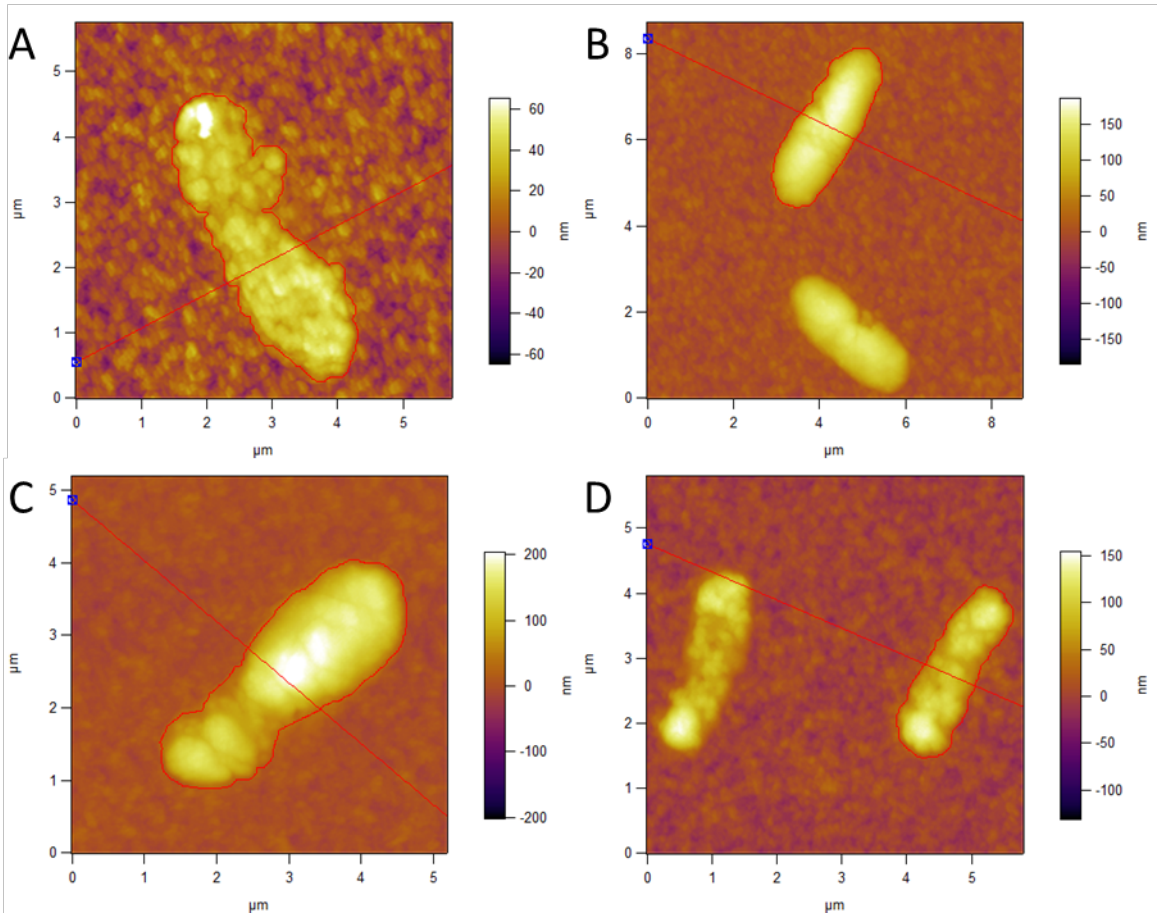

Figure 4.20 Representative AFM topography images for polymyxin B affected cells at t_1(**A,B**) and t_2(**C,D**). At t_1 a mixture of lysed cells and unaffected cells was observed. At t_2 only clearly affected cells were observed. Cross-sections indicate where width measurements were taken.

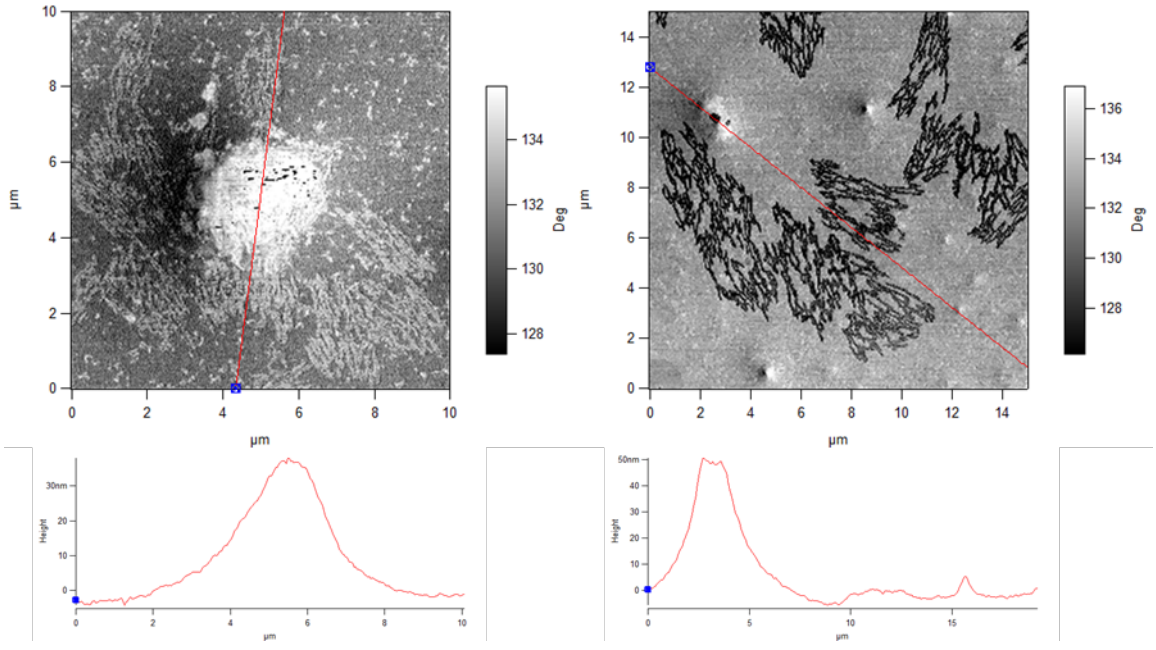

Figure 4.21 Representative AFM phase images of lysozyme 1mg/ml on glass at t_1(ten minutes after addition of the drug). The color scale corresponds to phase (degrees) and not height as previously seen. Cross-sections' heights are displayed underneath phase images.

Topography contrast was reduced due to the low (30 – 50 nm) heights of the cells. Phase images revealed a high contrast (compared to the hard glass substrate) polymeric-like substance, possibly DNA, radiating from the centre of bacterial remains. No rod-shaped cells were observed. Due to the limited number of samples available and the reduced height of cells, further metrics were not obtained for lysozyme. The dramatic images support the eponymous lysis due to non-specific cleavage of peptidoglycan bonds by the enzyme. Unlike ampicillin, which affected newly synthesised peptidoglycan and retained cell shape, lysozyme caused significant ruptures making it hard to identify individual bacteria.

Qualitative analysis of cell morphology is valuable in identifying behaviour such as the formation of spheroplasts (ampicillin), complete lysis (lysozyme) and stationary phases without lysis (kanamycin), but the main benefit of AFM characterisation is the availability of quantitative metrics such as height, width, length and volume.

4.4.2.4 **Quantitative AFM characterisation**

The metrics developed in Section 4.4.1.3 were applied to the AFM images of cells affected by antibiotics, with the exception of lysozyme. Figure 4.22 shows boxplots for all the AFM images recorded and analysed, including the 2% agarose control.

As previously described, the control cells on 2% agarose had cell heights between 144 and 176 nm, with a median of 155 nm and a mean of 157 ± 3 nm (one standard error). Cell widths ranged from 1.12 to 1.28 µm, with a median of 1.22 µm and mean of 1.20 ± 0.02 µm. Cell lengths ranged from 1.8 to 4.1 µm, with a median of 2.4 µm and mean of 2.5 ± 0.2 µm. Cell volumes were distributed between 0.30 and 0.50 μm^3 (with a single outlier at 0.71 μm^3), with a median of 0.39 μm^3 and mean 0.42 ± 0.03 μm^3.

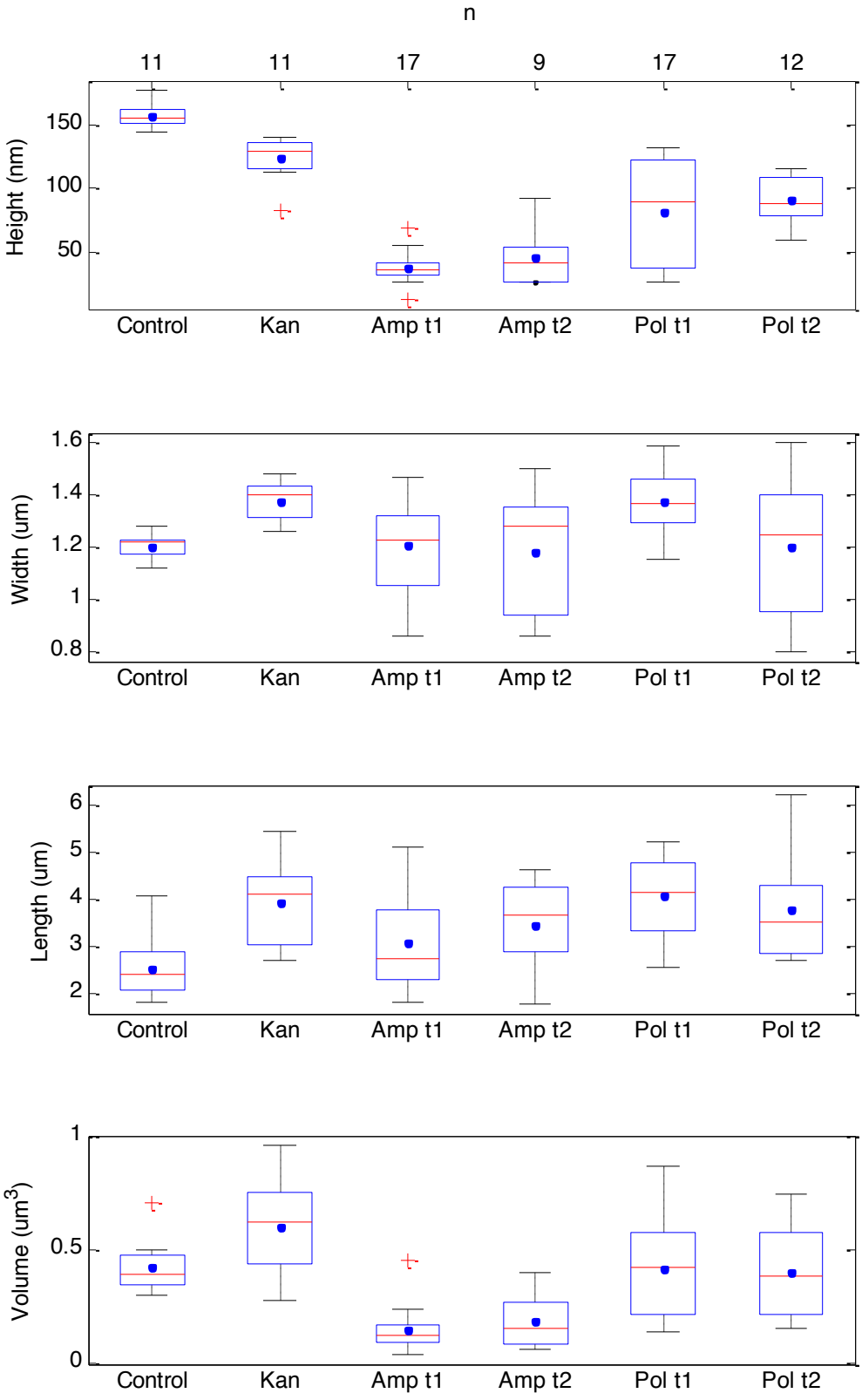

Figure 4.22 Boxplot representation of AFM metrics of antibiotics. For each sample height, width, length and volume distributions are plotted. Boxplots display mean as dot, median as red horizontal line, and the interquartile range (25th to 75th percentile) as a box. Whiskers extending up to a maximum of 1.5*IQR beyond or beneath the 75th & 25th quartiles respectively reflect the range of the data. Outliers outside this range are represented as red crosses. Control cells are 2% Agarose. At the top of the figure the sample size n is displayed.

Kanamycin affected cells exhibited heights between 115 and 140 nm (with a single outlier at 83 nm), with a median of 130 nm and mean of 124 ± 5 nm. Cell widths were between 1.26 and 1.48 µm, with a median of 1.40 µm and a mean of 1.37 ± 0.02 µm. Lengths varied between 2.71 and 5.45 µm, with a median of 0.62 µm and mean of 0.60 ± 0.06 µm. Cell volumes were broadly distributed between 0.28 and 0.96 μm^3, with a median of 0.62 μm^3 and mean of 0.60 μm^3.

Cells affected by ampicillin sampled at t_1 had narrowly distributed heights between 26 and 58 nm (with two outliers at 14 nm and 70 nm), with a median of 37 nm and mean of 39 ± 3 nm. Cell widths ranged from 0.86 to 1.47 µm, with a median of 1.23 µm and mean of 1.20 ± 0.05 µm. Lengths were distributed between 1.82 and 5.10 µm, with a median of 2.74 µm and mean of 3.06 ± 0.24 µm. Cell volumes ranged between 0.04 and 0.24 μm^3 (with an outlier at 0.45 μm^3), with a median of 0.12 μm^3 and mean of 0.15 ± 0.02 μm^3.

Cells affected by ampicillin sampled at t_2 had heights between 27 and 92 nm, with a median of 42 nm and mean of 46 ± 7 nm. Cell widths ranged between 0.86 and 1.50 µm, with a median of 1.28 µm and mean of 1.18 ± 0.08 µm. Lengths were between 1.79 and 4.62 µm, with a median of 3.68 µm and mean of 3.44 ± 0.34 µm. Cell volumes were distributed between 0.06 and 0.40 μm^3, with a median of 0.15 μm^3 and a mean of 0.19 ± 0.04 μm^3.

Polymyxin B affected cells at t_1 had heights between 27 and 132 nm, with a median of 90 nm and mean of 82 ± 10 nm. Cell widths ranged between 1.15 and 1.59 µm, with a median of 1.37 µm and mean of 1.37 ± 0.03 µm. Lengths were between 2.54 and 5.23 µm, with a median of 4.15 µm and mean of 4.06 ± 0.20 µm. Cell volumes were distributed between 0.14 and 0.87 μm^3, with a median of 0.42 μm^3 and mean of 0.41 ± 0.06 μm^3.

Polymyxin B affected cells at t_2 included heights between 60 and 116 nm, with a median of 89 nm and mean of 91 ± 5 nm. Cell widths were between 0.82 and 1.59 µm, with a median of 1.22 µm and mean 1.19 ± 0.08 µm. Lengths varied between 2.74 and 6.23 µm, with median 3.53 µm and mean 3.78 ± 0.32 µm. Cell volumes were distributed from 0.16 to 0.55 μm^3, with a median of 3.53 μm^3 and mean of 0.36 ± 0.04 μm^3.

Cell heights were reduced for each antibiotic, most dramatically for ampicillin followed by polymyxin B. Non-parametric post-hoc ANOVA tests revealed no significant difference ($p<0.05$) between the heights of control cells and kanamycin. This supports the stationary effect observed in cell growth curves and qualitatively in AFM images: cell heights were indistinguishable from control cells as lysis did not occur.

Ampicillin drastically reduced cell heights and volumes at both time points sampled, reflecting the lysed morphologies witnessed in the previous section. While the bacterial shape was retained, cell contents were not, indicating a strong lysis. Non-parametric statistical testing found no significant ($p < 0.05$) differences between t_1 and t_2.

Polymyxin B exhibited a range of phenotypes, as described in the previous section. At t_1 cell heights were lower, and broadly distributed down to 27 nm, caused by cells lysed rapidly after the addition of the drug. The presence of higher cells and a broad distribution in volume indicates that not all cells were lysed at t_1, supporting the qualitative analysis of images in the previous section. Cells were higher than ampicillin reflecting a reduction in cell lysis due to the distinct mechanism of action: polymyxin B affected membrane integrity resulting in cell leakage, whereas ampicillin affected cell wall integrity leading to larger ruptures and cell leakage.

The effects of three antibiotics which acted on different cell targets were quantitatively imaged on 2% agarose substrates in air. The internal effect of kanamycin resulted in a

small reduction in cell height and an increase in cell width, length and volume. Ampicillin, acting on newly formed peptidoglycan, significantly affected cell heights, widths and volumes of cells. Polymyxin B affected cell heights and widths, though not as substantially as ampicillin. The metrics for all the drugs are summarised below:

	n	Height (nm)	±	Width (μm)	±	Length (μm)	±	Volume (μm^3)	±
Control	11	157	3	1.20	0.02	2.52	0.20	0.42	0.03
Kan	11	124	5	1.37	0.02	3.94	0.27	0.60	0.06
Amp t_1	17	39	3	1.20	0.05	3.06	0.24	0.15	0.02
Amp t_2	9	46	7	1.18	0.08	3.44	0.34	0.19	0.04
Pol t_1	17	82	10	1.37	0.03	4.06	0.20	0.41	0.06
Pol t_2	12	91	5	1.19	0.08	3.78	0.32	0.40	0.06

Table 4.5 Summary of metrics for the control and three antibiotics on 2% agarose substrates. Data shown as mean values ± standard error of mean. n refers to the number of bacteria characterised per sample.

4.4.3 Atlas

The characterisations of the effects of selected antibiotics on *E. coli* DH5α are collated and shown in a reference atlas in Figure 4.23. This visualisation summarises the disk diffusion susceptibility assays, cell population growth curves and AFM characterisation for control cells, kanamycin, ampicillin, polymyxin B and lysozyme. An understanding of nanoparticle-cell interactions is now possible through the additional characterisation of the interactions of *E. coli* DH5α with a nanoparticle and comparison with this atlas, both visually in the first instance, and quantitatively through statistical testing of AFM metrics.

Target	Disk Diffusion	Cell population response	AFM	Height (nm)	Width (µm)	Length (µm)	Volume (µm³)
Control	**0**	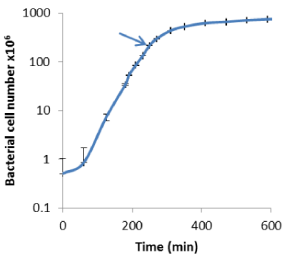	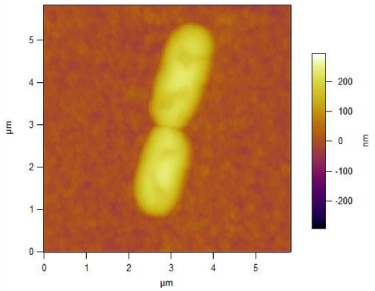	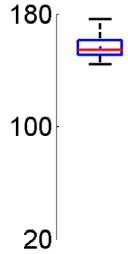	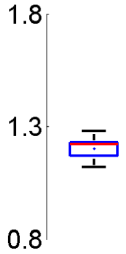	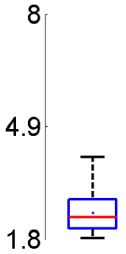	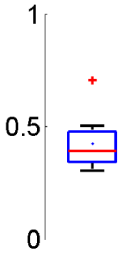
Internal *Kanamycin*	**14.8**	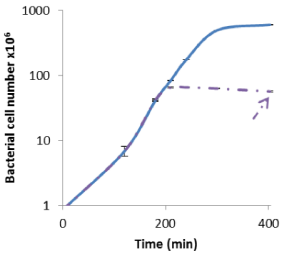	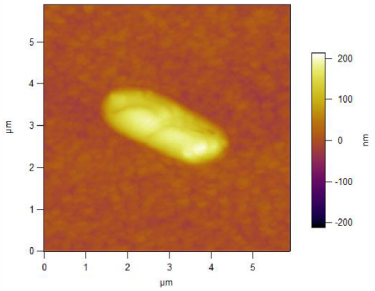	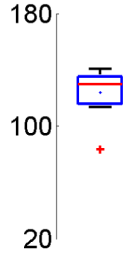	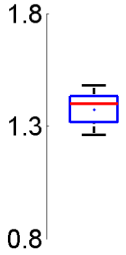	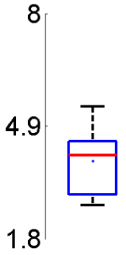	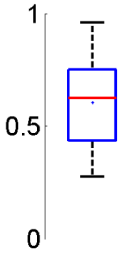
Peptidoglycan Synthesis t_1 *Ampicillin*	**28.4**	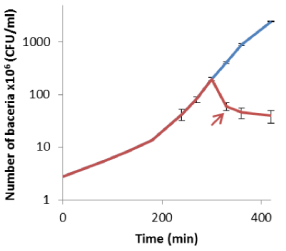	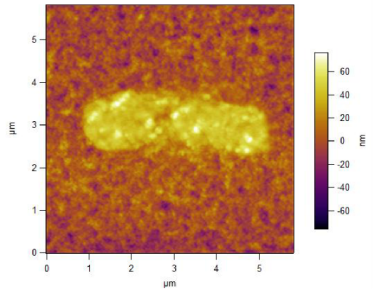	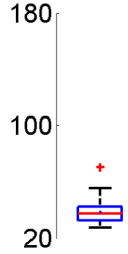	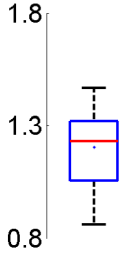	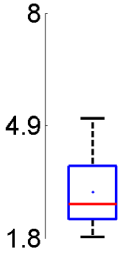	
Peptidoglycan Synthesis t_2 *Ampicillin*		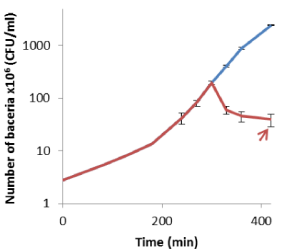	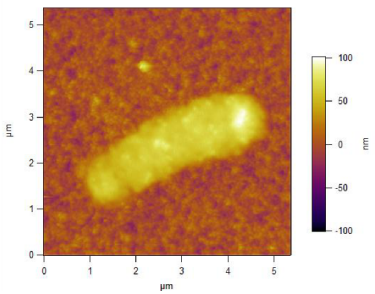	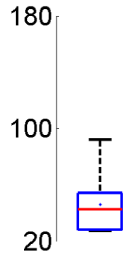	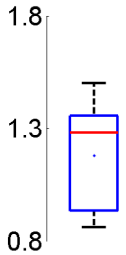	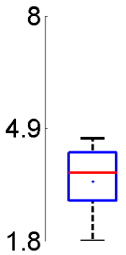	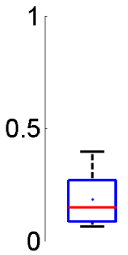

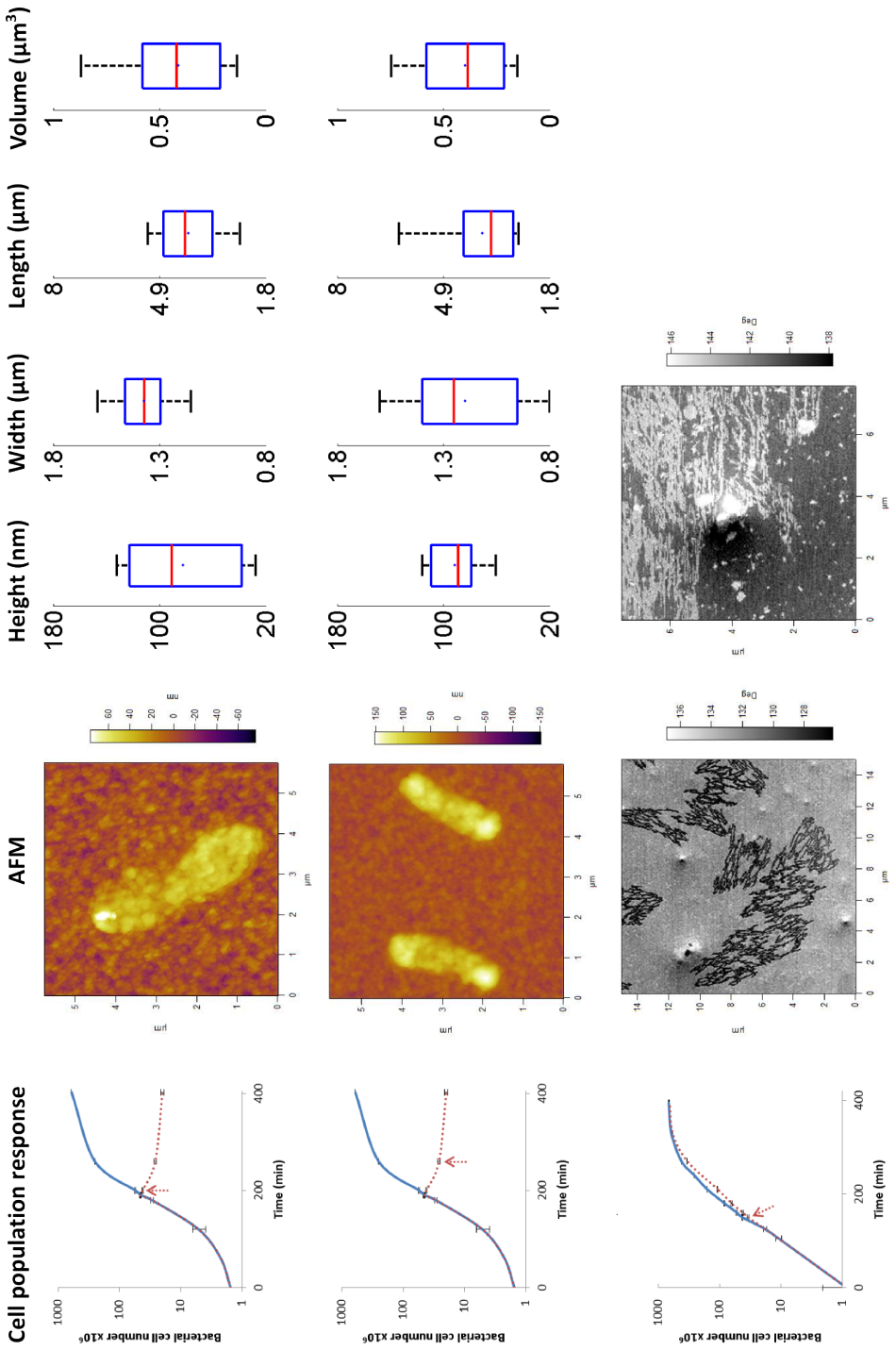

Figure 4.23 Reference atlas of antibiotic effects on *E. coli* DH5α. Disk diffusion zones of inhibitions are displayed in mm, for concentrations specified in the text. Cell population response is shown next to representative AFM topography images and metrics for each time point. Antibiotics selected act internally (kanamycin), on peptidoglycan synthesis (ampicillin), on the outer/inner membrane (polymyxin B) or on existing peptidoglycan (lysozyme). All images are representative and on 2% agarose substrates in air. For lysozyme phase images of cells are displayed, showing dramatic lysis.

4.5 Conclusions

A standard methodology to study the interactions of nanoparticles with cells has been proposed: generate an "atlas" of the effects of well-known drugs on a cell of interest, and compare with the effects of a nanoparticle. In this chapter the model organism *E. coli* DH5α was chosen, and four different antibiotics with distinct mechanisms of action selected as proof of principle. Kanamycin for its internal mechanism of action, ampicillin for targeting newly synthesised peptidoglycan in the cell wall, polymyxin B for destabilising the outer and inner membranes and lysozyme for its non-specific disruption of peptidoglycan. The resulting effects were characterised through disk diffusion assays, cell population growth curves and AFM, and summarised in a reference atlas. A novel method of sample preparation was developed and optimised for imaging bacteria from LB cultures under AFM with minimal sample manipulation using 2% agarose substrates in air. Quantitative metrics and a procedure to extract these from AFM images was developed.

The next chapter seeks to compare this atlas with the effects of silver nanoparticles, studied in Chapter 3.

Chapter 5

Silver nanoparticle interactions with bacterial cells

In the previous chapter the development of a methodology to study the effects of nanoparticles and cells was described and implemented for E. coli *DH5α. The methodology culminated in the characterisation of a range of antibiotics to build a comparative atlas of antibacterial effects. In this chapter the interactions of 10 and 30 nm citrate coated silver nanoparticles with* E. coli *are assessed in light of the atlas.*

5.1 Introduction

Chapter 4 described a methodology to study the interaction of nanoparticles with cells, implemented using the model organism *E. coli* DH5α. Combining disk diffusion assays, cell population growth curves and AFM a comparative atlas of the effects of a range of antibiotics on *E. coli* was produced (Figure 4.23). Using the same characterisation techniques on *E. coli* and a target nanoparticle will enable a quantitative comparison between the nanoparticle effects and those of the selected antibiotics, whose target and mechanism of action is well understood.

This chapter tests the methodology for 10 and 30 nm diameter silver nanoparticles. Silver nanoparticles have been extensively studied in Chapter 3 and are widely marketed commercially for their antibacterial properties in products such as anti-odour socks, air purifiers, hair dryers and washing machines (Nanotechnologies 2014).

Many studies on the antibacterial mechanism of action of silver nanoparticles point to nanoparticle-specific interactions with bacteria, whereas other studies propose a silver

ion-mediated mechanism (Amato, Diaz-Fernandez et al. 2011, Xiu, Zhang et al. 2012). This chapter aims to understand which mechanism is dominant, beginning with a review of our current understanding of antibacterial effects of silver ions and silver nanoparticles.

5.1.1 **Silver ions**

The antibacterial nature of silver has been utilised for centuries; from ancient Egyptian water purification to medieval surgical sutures to modern day wounds dressings (Lansdown 2010). Bulk metallic silver is inert, but in the presence of moisture slowly ionises, producing biologically active Ag^+. It is these silver ions which are responsible for the antibacterial effects of bulk silver. Historically, silver salts such as silver nitrate were used to treat infections, providing a readily available source of antibacterial silver ions until the discovery of penicillin and modern antibiotics (Klasen 2000). Only relatively recently have the mechanism(s) of action of Ag^+ been proposed.

Bragg and Rainnie (1974) reported that Ag^+ inhibited the oxidation of glucose and other respiratory substrates by *E. coli,* affecting cell viability. They recalled similar effects with mercurial compounds which bound to sulfhydryl groups (-SH thiol groups). Schreurs (1982) reported an inhibition in phosphate uptake and exchange in *E. coli* in the presence of silver ions, an effect that was mitigated by the addition of thiols. Liau, Read et al. (1997) reported that the addition of thiol-containing compounds such as cysteine to silver nitrate reduced its antibacterial efficacy against *E. coli*. Feng, Wu et al. (2000) reported the detachment of the cytoplasmic cell membrane from *E. coli* cell walls, formation of electron-dense silver/sulphur clusters externally and internally and condensation of DNA inside the cell when examined with electron microscopy. Jung, Koo et al. (2008) also reported the detachment of the cytoplasmic cell membrane from *E. coli* cell walls after treatment with Ag+, leading to the release of cell contents. Park, Kim et al. (2009)

reported an enhanced antibacterial action of Ag+ on *E. coli* in the presence of oxygen due to an internal production of reactive oxygen species. They suggested an Ag+/thiol interaction led inhibition of superoxide dismutases as responsible for the measured generation of toxic superoxide radicals and enhanced bactericidal effect. Yang, Yang et al. (2010) reported vesicle formation and damage to the outer membrane of *E. coli* after treatment with Ag+.

While the mechanism of action of silver ions is not fully understood, the literature supports a strong interaction with phosphate and thiol groups which are ubiquitous in cells. Internal effects on the respiratory chain or DNA necessitate entry of Ag+ into the cytoplasm of the cell. The reported disruption to the cell membrane is likely due to the presence of thiol-rich proteins in the outer membrane.

5.1.2 **Silver nanoparticles**

Silver nanoparticles have more recently been applied as antibacterial agents, and their mechanism of action is still under debate. There are various methods to synthesising silver nanoparticles, and many different coatings are used in the literature.

Sondi and Salopek-Sondi (2004) studied the effect of Daxad- (a formaldehyde based dispersant) coated ~ 15 nm diameter silver nanoparticles on *E. coli.* They reported damage to cell membranes and the formation of pits, leading to cell death. Morones, Elechiguerra et al. (2005) studied the effect of carbon matrix dispersed ~ 16 nm silver nanoparticles on *E. coli*, reporting deposition of nanoparticles on the cell membrane and internally, suggested that nanoparticles bound to sulphur and phosphate rich compounds affecting cell viability. Lok, Ho et al. (2006) conducted proteomic analysis of ~ 9 nm borohydride/citrate coated silver nanoparticle affected *E. coli*, reporting a depletion in the proton motive force, destabilisation of the outer cell membrane and reduction in

available ATP to the cell. These effects were similar to those exerted by silver ions, with the authors suggesting the same mechanism of action for both, varying only in the concentration of silver ions/nanoparticles required for an antibacterial effect (less nanoparticles were required than silver ions by number for a minimum antibacterial activity). The authors later reported that only partially oxidised silver nanoparticles exhibited an antibacterial effect, which was size dependent. Smaller, oxidised nanoparticles (with higher proportions of chemisorbed Ag^+) were found to be more toxic than larger oxidised nanoparticles or reduced nanoparticles (Lok, Ho et al. 2007). The authors suggested that the antibacterial nature of silver nanoparticles was as a result of Ag^+ release. Pal, Tak et al. (2007) reported a shape dependent bactericidal effect of citrate/CTAB (a disinfectant) coated silver nanoparticles, finding triangular nanoparticles (with a higher number of more reactive [111] facets) more bactericidal than spherical nanoparticles. They suggested this higher reactivity led to a faster release of Ag^+ which formed the mechanism of antibacterial action (they also observed damage to cell membranes). Hwang, Lee et al. (2008) used stress-specific bioluminescent *E. coli* to study the antibacterial effect of formaldehyde coated 10 nm silver nanoparticles. They reported a combined effect of protein/membrane damage by nanoparticles and superoxide radical formation by Ag^+ released by nanoparticles. Choi, Deng et al. (2008) studied the effect of ~ 14 nm diameter PVA coated silver nanoparticles on *E. coli*, finding *more* nanoparticles by number were required to attain an antibacterial effect compared to silver ions. They reported cell membrane pitting, but no found evidence of cell membrane leakage. Sotiriou and Pratsinis (2010) studied size-specific antibacterial effects of silver nanoparticles dispersed in a silica matrix on *E. coli*. They found that smaller (< 10 nm) nanoparticles released more Ag^+ ions and had a larger antibacterial effect, but that larger nanoparticles also exhibited an antibacterial effect that was not dependent on the

presence of Ag^+. Liu and Hurt (2010) measured Ag^+ ion release from 2-8 nm citrate coated silver nanoparticles in deionised water. They found that the process was temperature, pH and oxygen dependent, and that complete dissolution took 2-6 days. Kittler, Greulich et al. (2010) similarly reported dissolution of 50 nm citrate and PVP coated nanoparticles in distilled water. "Older" solutions of nanoparticles, which had had more time for dissolution, were more bactericidal due to the higher concentration of Ag^+ present. Liu, Sonshine et al. (2010) reported techniques to fine tune the release rate of silver ions from silver nanoparticles through the addition of different capping agents. Xiu, Ma et al. (2011) reported a reduction, though not elimination, of the antibacterial activity of ~ 35 nm diameter silver nanoparticles coated in amorphous carbon in the absence of oxygen. They also reported an antibacterial effect of Ag+ in the absence of oxygen, quenched by the addition of cysteine or sodium sulphide, ruling out a purely ROS (reactive oxygen species) mediated mechanism of action. Amato, Diaz-Fernandez et al. (2011) synthesised cysteine and glutathione coated ~ 7 nm silver nanoparticles. Their measured Ag^+ release was below a minimum inhibitory concentration, and the authors concluded that the bactericidal effects found were as a result of the direct interaction of the silver nanoparticles with *E. coli*, and not due to the release of Ag^+. Xiu, Zhang et al. (2012) synthesised and tested PEG-coated silver nanoparticles on *E. coli* under aerobic and anaerobic conditions. In the absence of oxygen no release of silver ions or toxic effects were measured, whereas in the presence of oxygen silver ion release was measured and a toxic effect established, leading to the conclusion of a purely aerobic, ion-mediated antibacterial effect of the silver nanoparticles.

Silver ions are toxic to bacteria and to humans in large doses, and silver nanoparticles release silver ions through a size, shape, temperature and pH dependent oxidative dissolution process (Berman 1980). The extent to which ions as opposed to nanoparticles

are toxic is still debated, and this chapter aims to apply the methodology previously presented to answer the question: how do 10 and 30 nm diameter citrate coated silver nanoparticles act on *E. coli*? How does their mechanism of action compare to silver ions (in the form of silver nitrate)?

5.2 Materials and methods

The methodology presented in the previous chapter was applied to establish the bactericidal effect and mechanism of action of silver nanoparticles and ions. 10 (9 ± 1.8) nm and 30 (32 ± 2.1) nm commercially available silver nanoparticles were obtained due to the effects of nanoparticle stability over time observed in Chapter 3: nanoparticles must be freshly synthesised to minimise aggregation and uncontrolled release of ions (Nanocomposix, San Diego, USA). Additionally, for nanotoxicological assays a precise mass concentration is required, which was unavailable for the nanoparticles synthesised in Chapter 3. Nanoparticles were obtained at a concentration of 1 mg/ml and characterised by the manufacturer. They were stored at 4°C in nitrogen in the absence of light to prevent aggregation/dissolution over time.

5.3 Results and discussion

In the previous chapter, well studied antibiotics were used to build a comparative atlas of morphological effects on *E. coli*. To compare the effect of silver nanoparticle to this atlas, the three characterisation techniques used were applied.

5.3.1 Disk diffusion assay

Figure 5.1, summarised in Table 5.1, shows the resulting zones of inhibition measured for 10 μg Ag+, 10 nm and 30 nm silver nanoparticles.

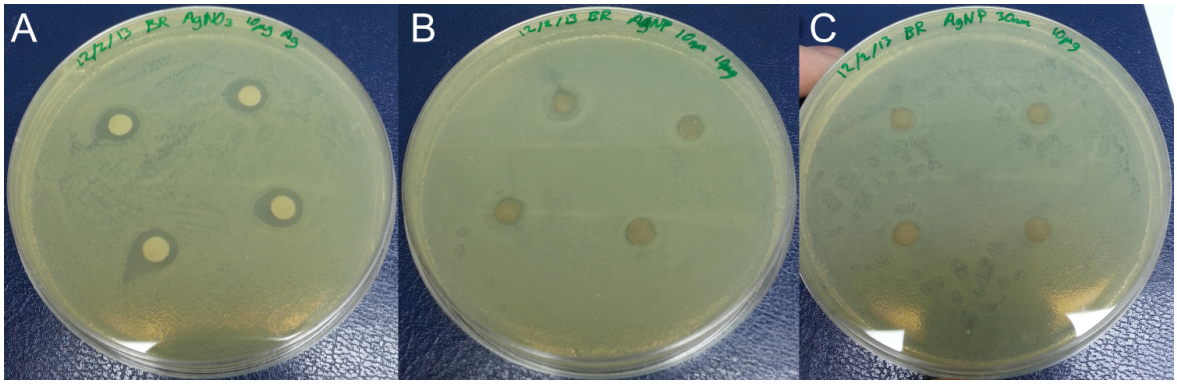

Figure 5.1 Disk diffusion assays for 10 µg Ag+ (**A**), 10 nm (**B**) and 30 nm (**C**) silver nanoparticles. Nanoparticles precipitated visibly on the filter paper and showed no visible inhibition. Ag+ showed visible inhibition, with one anomalous reading in the bottom left quadrant, likely due to an excess of surface liquid on the plate at the time of incubation.

No zone of inhibition was measured for 10 or 30 nm nanoparticles at the maximum concentration available, indicating a lack of bacterial susceptibility in contrast to the large body of academic work reviewed. Silver ions at the same concentration exhibited a 9.6 ± 0.3 mm zone of inhibition. The lack of susceptibility of *E. coli* to silver nanoparticles was attributed to the precipitation upon contact of the nanoparticles with the filter paper. This prevented the diffusion and activity of the silver nanoparticles. To verify this was indeed the case and that the silver nanoparticles were toxic, cell population response of *E. coli* to silver nanoparticles was pursued.

Species	Concentration (µg)	Zone of inhibition (mm)	± (mm)
Ag+	10	9.6	0.3
AgNP 10nm	10	0.0	0.0
AgNP 30nm	10	0.0	0.0

Table 5.1 Disk diffusion inhibition zones, ± represents one standard error of the mean for triplicate measurements.

5.3.2 Cell population response

To examine the antibacterial effect of nanoparticles directly in LB, *E. coli* DH5α cell cultures were grown and inoculated as previously described with 2 µg/ml 10 nm silver nanoparticles and silver ions (silver nitrate) (Figure 5.2).

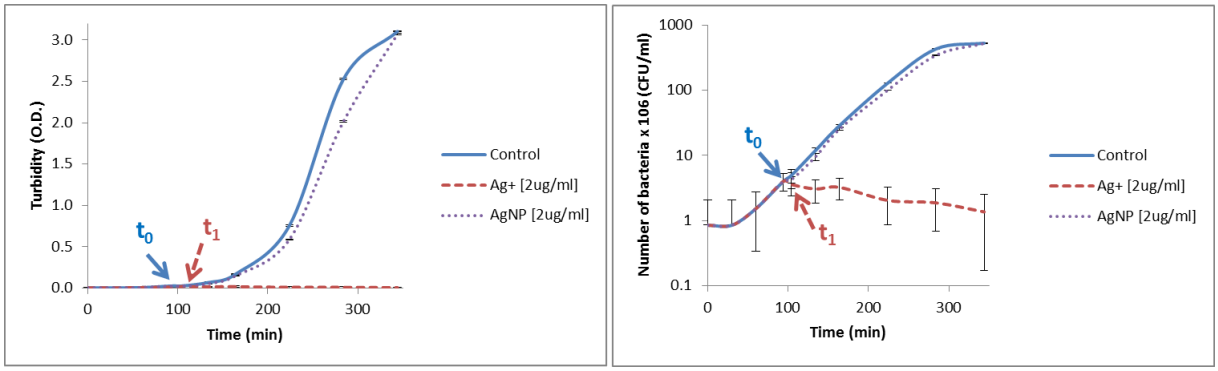

Figure 5.2 Triplicate growth curves for 10 nm silver nanoparticles (AgNP) and silver ions (Ag+) 2 µg/ml adjusted for nanoparticle/ion absorption at 600 nm. The left hand graph plots turbidity (optical density) values as a function of time, and the right hand graph plots the equivalent number of cells on a log scale as a function of time. $\boldsymbol{t_0}$and $\boldsymbol{t_1}$ correspond to the initial addition of the AgNP/Ag+ and first measured effect respectively. Error bars represent compound experimental (equipment) and random (triplicate) errors.

Silver ions showed a rapid antibacterial effect with a reduction in bacterial number compared to the control after 10 minutes (t_1). 10 nm silver nanoparticles showed minimal inhibition of bacterial growth after inoculation.

At the moment of inoculation of the silver nanoparticles, a white precipitate was observed in solution. Additional experiments were conducted to measure the absorbance of nanoparticles in LB, revealing a time and concentration dependent interaction (Figure 5.3). This was used to calibrate the absorbance measurements in Figure 5.2, but poses an additional problem: if nanoparticles are interacting with the medium, then the concentration of nanoparticles available to interact with any bacteria is unknown, and explains the lack of toxicity observed in both disk diffusion tests and cell population growth curves.

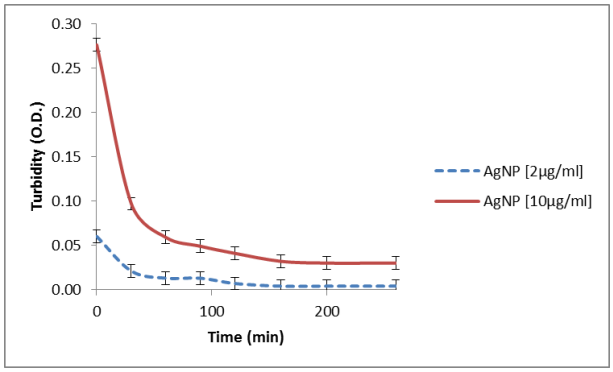

Figure 5.3 Optical **a**bsorbance of 10 nm nanoparticle solutions in LB over time. An initial high absorbance gives way to lower absorbances as the nanoparticles interact with the medium. For a concentration of 10 µg/ml (five times higher than 2 µg/ml), the initial absorbance was also approximately five times higher, indicating an linear absorption related to number of nanoparticles present.

Recent work reported at the time of this study confirmed the interaction of Ag+ and AgNP with Cl^-, PO_4^{3-}, S^{2-} and SO_4^{2-}, which mitigated the number of Ag+/AgNP particles free to interact with the bacteria (Xiu, Ma et al. 2011). LB is a medium designed to promote and sustain bacterial growth - components include ~ 170 mM sodium chloride, casein digest (amino acids) and yeast extract, rich in phosphates and sulphide compounds. Any interaction of the silver nanoparticles with the medium will reduce the number of biologically available nanoparticles that can interact with cells, necessitating a change in medium.

5.3.3 Sodium bicarbonate (SB) buffer

To overcome the issue of nanoparticle sequestration by the culture medium, a sodium bicarbonate buffer was used to study the effects of Ag+/AgNP on *E. coli* (Xiu, Ma et al. 2011). The protocol to transfer cells from LB to sodium bicarbonate (SB) buffer is as follows:

Protocol 5.1 Transferring *E. coli* cells from LB to SB

1. Grow up cells in LB to an optical density of 0.5 A.U.
2. Spin down @ 3krpm for 15 minutes.
3. Resuspend in 2mM sodium bicarbonate buffer, pH ~ 8.

4. Repeat steps 2 & 3 twice.

5.3.3.1 Control cells

To establish the effect of the new buffer on cell susceptibility, growth and morphology, the characterisation techniques were applied to control cells.

5.3.3.1.1 Disk diffusion assays

Disk diffusion assays were not possible in the SB buffer due to the lack of cell growth nutrients in SB – plating would not have induced the cell growth required for susceptibility assays.

5.3.3.1.2 Cell population response

The viability of the cells in SB was first tested by measuring cell density over time in SB while incubating at 37°C (Figure 5.4). Cell numbers declined initially, as the cells adapted to their new environment, but were fairly stable after 3 hours of incubation. Colony counting after plating cells incubated for 6 hours ($\boldsymbol{t_1}$) confirmed that cells were viable (data not shown).

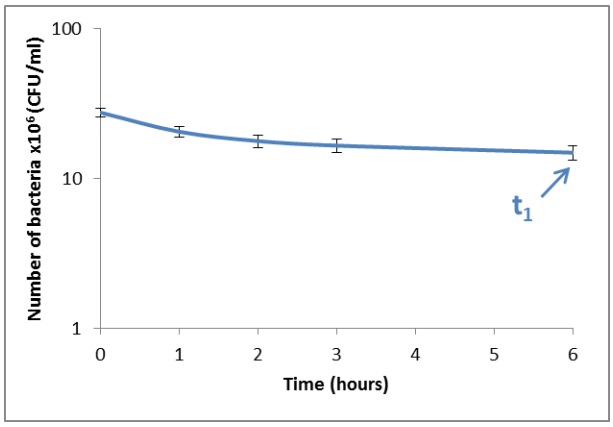

Figure 5.4 Cell population response in sodium bicarbonate buffer. An initial decrease in cell number was observed, followed by a stationary period. No cell growth was observed due to a lack of nutrients in SB.

5.3.3.1.3 Cell morphology

Control cells at t_1 were aliquoted onto agarose substrates and imaged with AFM (Figure 5.5). The change in medium required a re-optimisation of sample preparation: due to a

large decrease in cell height observed and lack of extraneous matter in SB, cells were imaged on 1% agarose substrates to minimise absorption from the cells. Cells retained their rod-shape and did not exhibit any morphological changes, other than a decrease in cell height and an increase in cell length in cells sampled. Any decrease in cell height would be expected as the bacteria are unable to maintain the volumes they established in LB due to the lack of available nutrients. A quantitative analysis of this theory follows.

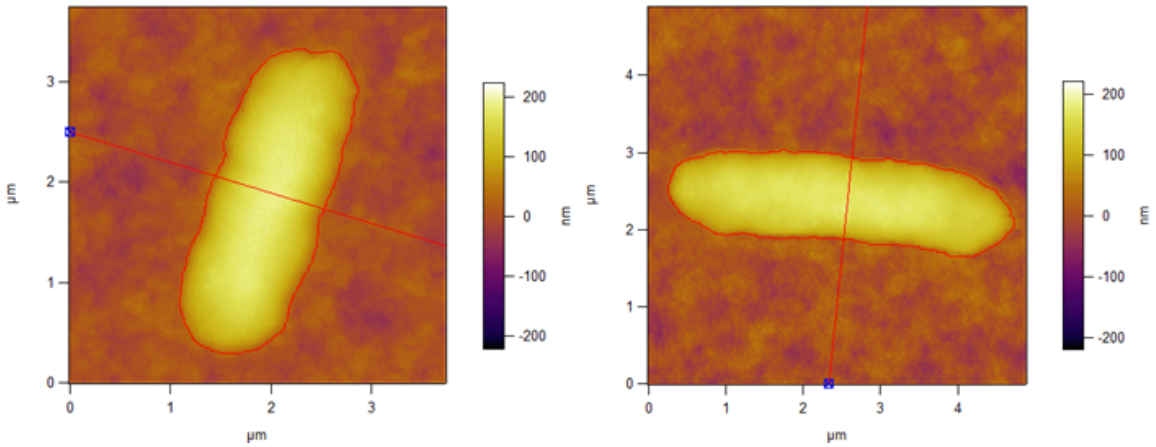

Figure 5.5 Representative AFM topography images of *E. coli* DH5α transferred to sodium bicarbonate buffer (SB) on 1% agarose substrates. Image masks used to define the boundaries for bacteria are indicated in red. The cross section used to measure bacterial width is also shown in red.

5.3.3.1.4 Quantitative AFM characterisation

Figure 5.6 shows boxplot comparisons for *E. coli* in LB and SB on 1% agarose substrates.

As previously described, cells grown in LB and imaged on 1% agarose had heights distributed between 156 and 194 nm, with a median of 184 nm and mean of 180 ± 5 nm (one standard error of the mean). Cell widths ranged between 1.19 and 1.28 µm with a median of 1.26 µm and mean of 1.24 ± 0.01 µm. Lengths were distributed between 2.0 and 3.5 µm (with a single outlier at 4.8 µm), with a median of 2.5 µm and a mean of 2.9 ± 0.4 µm. Cell volumes varied between 0.32 and 0.98 μm^3, with a median of 0.52 μm^3 and mean of 0.58 ± 0.08 μm^3.

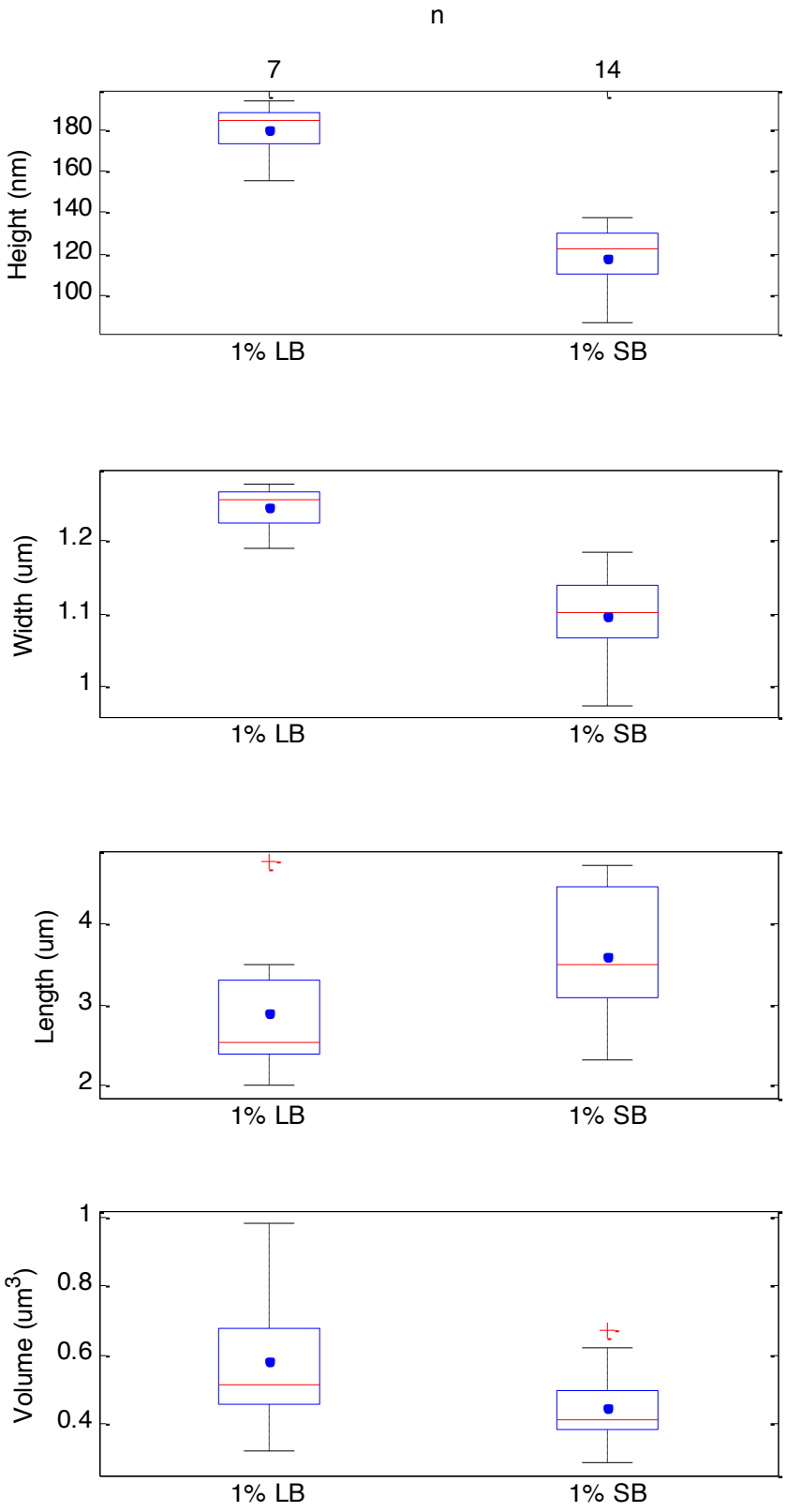

Figure 5.6 Boxplot comparison of LB and SB media for *E. coli* on 1% agarose substrates. Height, width, length and volume distributions are plotted. Boxplots display mean as dot, median as red horizontal line, and the interquartile range (25^{th} to 75^{th} percentile) as a box. Whiskers extending up to a maximum of 1.5*IQR beyond or beneath the 75^{th} & 25^{th} quartiles respectively reflect the range of the data. Outliers outside this range are represented as red crosses. At the top of the figure the number of bacterium n is displayed.

Cells transferred to SB had heights distributed between 87 and 138 nm, with a median of 123 nm and mean of 118 ± 4 nm. Widths were between 0.98 and 1.18 μm, with a median of 1.10 μm and mean of 1.10 ± 0.01 μm. Lengths ranged between 2.32 and 4.73 μm, with median 3.51 μm and mean 3.59 ± 0.20 μm. Cell volumes were between 0.29 and 0.62 μm^3 (with a single outlier at 0.67 μm^3), with a median of 0.41 μm^3 and mean of 0.45 ± 0.03 μm^3.

The reduction in cell heights and widths in SB can be explained by the lack of available nutrients for the cells. Without nutrients cells are unable to maintain the same cell volumes as in LB. An increase in cell length was observed, and was also attributed to the lack of nutrients: cells will take longer to replicate the chromosome and divide with fewer nutrients available, resulting in elongated cells before division is completed.

Having established and characterised *E. coli* in the new SB medium, any interactions between silver ions or nanoparticles and SB were investigated.

5.3.4 Interactions of silver ions and nanoparticles with SB

Interactions of silver ions and nanoparticles with the new medium were investigated optically by measuring absorbance changes and by monitoring precipitation formation on the addition of nanoparticles and ions to SB both immediately and over time. No absorbance changes or precipitation were observed, indicating negligible interactions between the nanoparticles and medium.

5.3.4.1 Minimum bactericidal concentrations (MBC)

SB does not allow for growth of cell cultures, so an additional assay was established to measure bacterial susceptibility. A protocol was developed to measure the minimum bactericidal concentration, defined as the concentration of drug (nanoparticles or ions) required to completely inhibit bacterial growth after sub-culture onto drug free LB plates:

Protocol 5.2 Determining minimum bactericidal concentration in SB

1. Transfer cells to SB (Protocol 5.1)
2. Adjust optical density of culture to 0.2 A.U.
3. Add 1 ml to 15ml falcon.
4. Add 1 ml (2x) drug to falcon (final composition: 1x drug + 0.1 A.U. cells).
5. Incubate @ 37°C 152rpm shaking for 2 hours.
6. Perform 10^4 serial dilution.
7. Plate 50 µl on LB-Agar for CFU counts (control should give ~100 cells).

The protocol was used to determine the percentage of live cells as a function of concentration, with the MBC defined as the lowest concentration required to achieve 0% live cells, extrapolated from Figure 5.7.

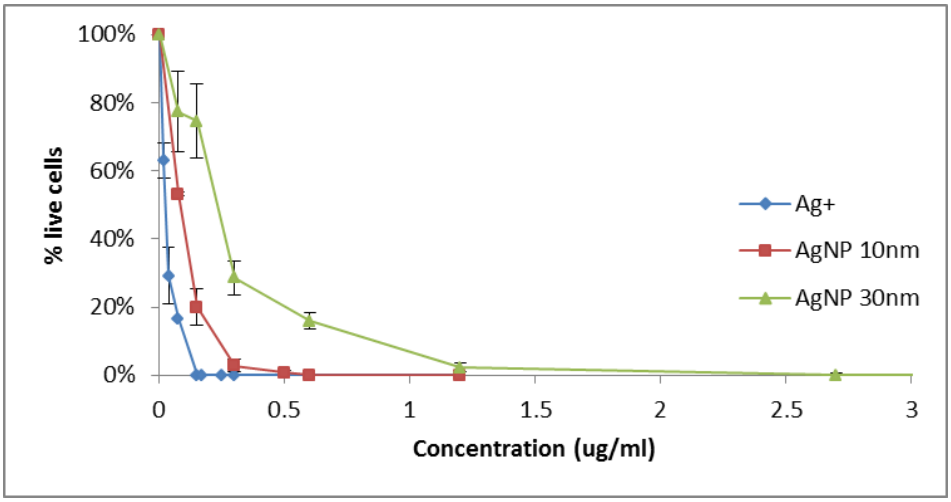

Figure 5.7 Determining the minimum bactericidal concentrations of Ag+, AgNP 10 nm and 30 nm in sodium bicarbonate buffer. Percentage of live cells were measured relative to a control with no antibacterial agent. Error bars represent one standard error of the mean for triplicate samples. All species exhibited an antibacterial effect. Minimum bactericidal concentrations correspond to the x-intercepts for each curve (0% live cells).

Silver ions required 0.15 µg/ml to establish 100% cell death, AgNP 10nm 0.5 µg/ml and AgNP 30nm 3 µg/ml. These values are considerably lower than the 10 µg/ml tested in LB which had no effect, highlighting the extent of LB-nanoparticle interaction. Silver ions had the lowest MBC by mass, followed by 10 nm and 30 nm silver nanoparticles respectively.

This concentration dependence is related to the stoichiometry of ions/nanoparticles involved: free ions are more toxic than structured ions (in bulk or nano form).

Having established a susceptibility of *E. coli* to silver ions, 10nm and 30 nm nanoparticles, cell population response and morphological effects were studied.

5.3.4.2 Cell population response

The response of cells in SB to Ag+ and AgNP 10nm is shown in Figure 5.8. Neither species caused cell lysis or any visible difference from control cells. Control cells were viable after 6 hours, but no viable cells were found after treatment with Ag+, AgNP 10 nm or 30 nm (data not shown).

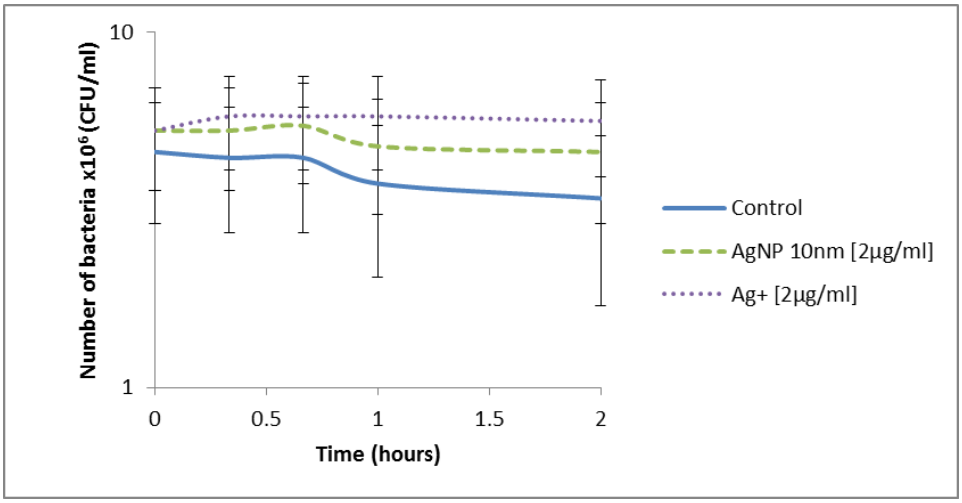

Figure 5.8 Cell population response of above MBC concentrations of Ag+ and AgNP 10 nm in SB. Error bars represent experimental uncertainty in turbidity measurements. No significant differences between datasets were observed.

5.3.4.3 Cell morphology

Cells drawn directly from 2 hour incubations as per Protocol 5.2 with 0.25 µg/ml Ag+, 1 µg/ml 10 AgNP and 8 µg/ml 30 nm AgNP (all concentrations above the MBC determined previously) were imaged with AFM on 1% agarose substrates in air.

5.3.4.3.1 Ag+

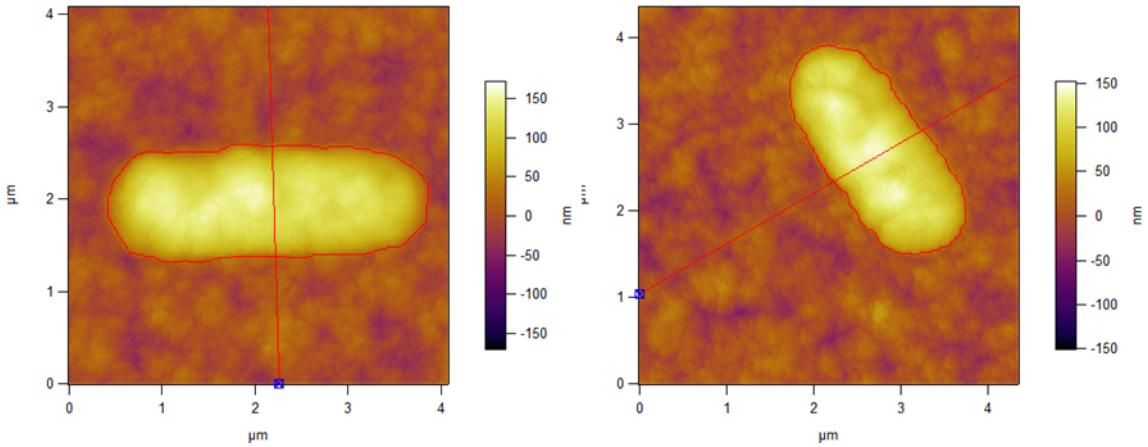

Figure 5.9 Representative AFM topography images of *E. coli* affected by Ag+ in sodium bicarbonate buffer (SB) on 1% agarose substrates.

No qualitative difference in cell morphology was observed for cells affected by silver ions, supporting the internal effect of Ag+ proposed in the literature and the lack of cell lysis observed in cell population studies over time.

5.3.4.3.2 AgNP 10nm

Cells affected by 10 nm AgNP (Figure 5.10) did not reveal significant morphological differences compared to control cells or cells killed by Ag+. No evidence for nanoparticle/cell wall attachment or pitting was found, supporting those studies citing an internal mechanism of action for silver nanoparticles and the lack of cell lysis observed in cell population studies.

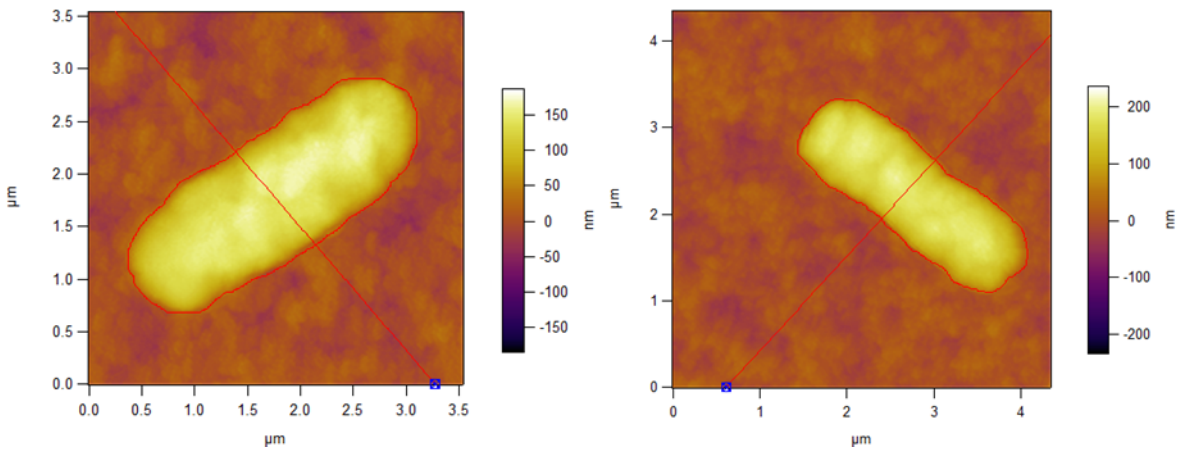

Figure 5.10 Representative AFM topography images of *E. coli* affected by 10 nm AgNP in sodium bicarbonate buffer (SB) on 1% agarose substrates. No significant differences with the control cells (Figure 5.5) were visible.

5.3.4.3.3 AgNP 30nm

Cells affected by 30 nm AgNP (Figure 5.11) did not demonstrate significant morphological differences compared to control cells, cells killed by Ag+ or cells killed by 10 nm AgNP. 30 nm nanoparticles were observed non-specifically bound to the substrate and the edges of the bacteria. No evidence for nanoparticle/cell wall attachment or pitting was found. This again supports the hypothesis that silver nanoparticles affect cells internally and not through disruption of the cell membrane or cell wall.

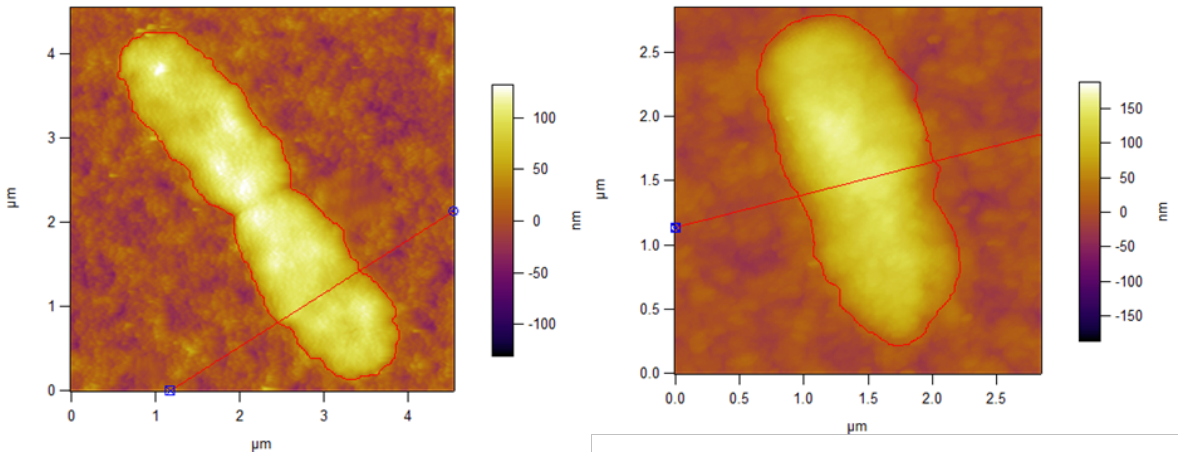

Figure 5.11 Representative AFM topography images of *E. coli* killed by 30 nm AgNP in sodium bicarbonate buffer (SB) on 1% agarose substrates. 30 nm nanoparticles were visible on the substrate.

5.3.4.4 Quantitative analysis of AFM characterisation

To quantify the qualitative observation on cell morphology discussed, the metrics defined in Section 4.4.1.3 were applied and obtained for cells affected by silver ions, 10 nm and 30 nm silver nanoparticles.

Control cells were as described previously: heights ranged between 87 and 138 nm, with a median of 123 nm and mean of 118 ± 4 nm. Widths were between 0.98 and 1.18 µm, with a median of 1.10 µm and mean of 1.10 ± 0.01 µm. Lengths were distributed between 2.32 and 4.73 µm, with median 3.51 µm and mean 3.59 ± 0.20 µm. Cell volumes were between 0.29 and 0.62 μm^3 (with a single outlier at 0.67 μm^3), with a median of 0.41 μm^3 and mean of 0.45 ± 0.03 μm^3.

Cells affected by Ag+ had heights distributed between 77 and 100 nm, with a median of 93 nm and mean of 91 ± 3 nm (one standard error of the mean). Widths were between 1.15 and 1.29 µm, with a median of 1.19 µm and mean of 1.20 ± 0.02 µm. Lengths ranged between 2.20 and 4.23 µm, with median 3.20 µm and mean 3.27 ± 0.20 µm. Cell volumes were between 0.20 and 0.41 μm^3, with a median of 0.35 μm^3 and mean of 0.33 ± 0.02 μm^3.

10 nm silver nanoparticle affected cells had heights ranging from 90 and 147 nm, with median 114 nm and mean 118 ± 3 nm. Cell widths were between 1.00 and 1.26 µm (with a single outlier at 0.91 µm), with a median of 1.09 µm and mean of 1.09 ± 0.02 µm. Lengths varied between 1.87 µm and 4.58 µm, with median 3.12 µm and mean 3.18 ± 0.15 µm. Volumes ranged from 0.19 to 0.62 μm^3, with median 0.38 μm^3 and mean 0.38 ± 0.02 μm^3.

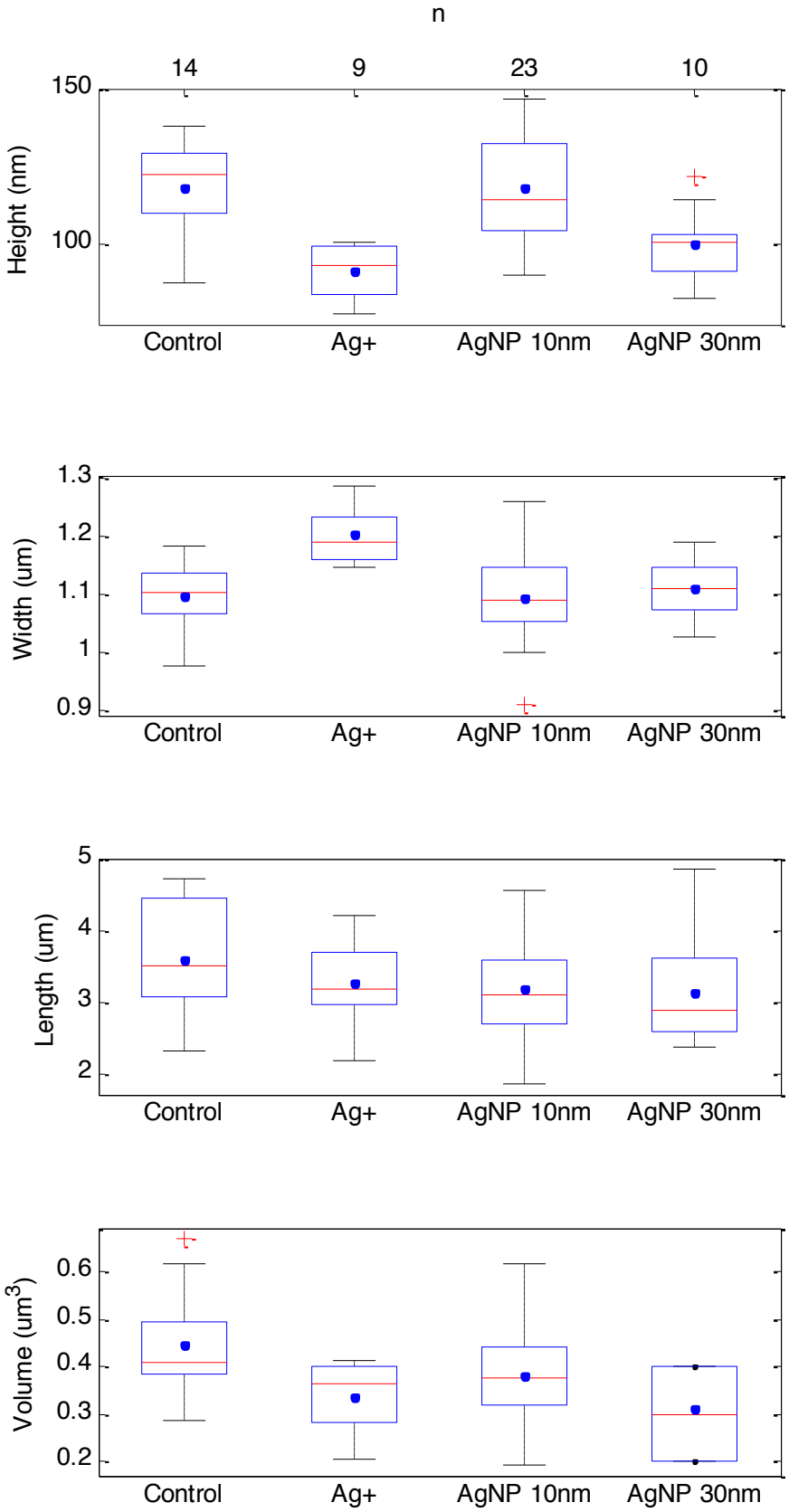

Figure 5.12 Boxplot representation of AFM metrics of cells killed by Ag+, AgNP 10nm and 30nm in SB. For each sample height, width, length and volume distributions are plotted as before. Control cells are unaffected cells in SB. At the top of the figure the number of bacteria n is displayed.

Cells affected by 30 nm silver nanoparticles had heights distributed between 82 and 114 nm (with a single outlier at 122 nm), with median 101 nm and mean 100 ± 4 nm. Widths ranged between 1.03 and 1.19 μm, with median 1.11 μm and mean 1.11 ± 0.02 μm. Cell lengths were between 2.37 and 4.86 μm, with median 2.89 μm and mean 3.14 ± 0.24 μm. Volumes varied between 0.20 and 0.40 μm^3, with median 0.30 μm^3 and mean 0.31 ± 0.03 μm^3.

ANOVA analysis (Appendix B) revealed significant ($p < 0.05$) differences between the heights of control cells and those affected by silver ions and 30 nm nanoparticles, which both had means approximately 20% lower than the control. For reference, kanamycin-affected cells (Chapter 4) had mean heights 21% lower than their control. No significant differences where observed between the heights of cells affected by 10 nm nanoparticles and the control.

In all cases, no significant changes to cell morphology were observed qualitatively, although a significant reduction in cell height was obtained for silver ions and 30 nm nanoparticles. Despite the size-dependent differences between 10 nm and 30 nm nanoparticles, the lack of cell lysis observed by cell population studies and AFM characterisation most closely matched that of kanamycin in Chapter 4 – known to affect internal processes. This supports the body of literature that silver ions and nanoparticles affect bacteria internally through a ROS-mediated mechanism, and not through disruption of the cell membrane or wall complex. A quantitative comparison between the results in this chapter and Chapter 4 was not possible due to the different medium and percentage agarose substrate used.

5.4 Conclusions and future work

A modified protocol was required to study the bactericidal effect of silver ions and silver nanoparticles due to a strong complexation with the growth medium used. Ions and nanoparticles exerted an internal bactericidal effect most similar to that seen in kanamycin in the previous chapter. Cell population response excluded a bateriolytic effect, and no lysis was observed with AFM. AFM analysis indicated that cell morphology was unaffected, though further investigation is warranted to explore the size-dependent affect on bacterial height between 10 nm and 30 nm silver nanoparticles.

A direct comparison with the atlas presented in the previous chapter was not possible with silver nanoparticles due to the complex interactions of silver species with the media, however similarities between the effects of kanamycin and its control were observed in a sodium bicarbonate buffer, suggested an internal mechanism. Further, the lack of observed differences between silver ions and nanoparticles supports an ion-mediated killing mechanism: nanoparticles release silver ions which are toxic and lead to cell death.

AFM is an excellent tool for studying morphological changes in cells with disrupted cell walls and membranes, as seen in the previous chapter. For drugs not resulting in cell membrane damage and/or cell lysis however, the amount of additional information compared to the control is minimal.

In the light of these observations, an alteration to the methodology presented in Chapter 4 to accommodate the two previous issues is proposed (Figure 5.13). The first step in studying any nanomaterial interaction with a host organism is to establish a bactericidal effect. The growth medium may affect the availability of the nanomaterial, requiring alternative media minimising this effect. If any bacteriolytic effects are found from cell population response studies, these can be studied with AFM or suitable EM. Otherwise,

internal characterisation technique such as proteomic analysis or another biochemical technique would be more suitable. Overall this schema allows the comprehensive characterisation of nanoparticle/cell interactions, which when combined with an atlas of the effects of antibiotics, gives valuable quantitative insight into nanomaterial toxicity.

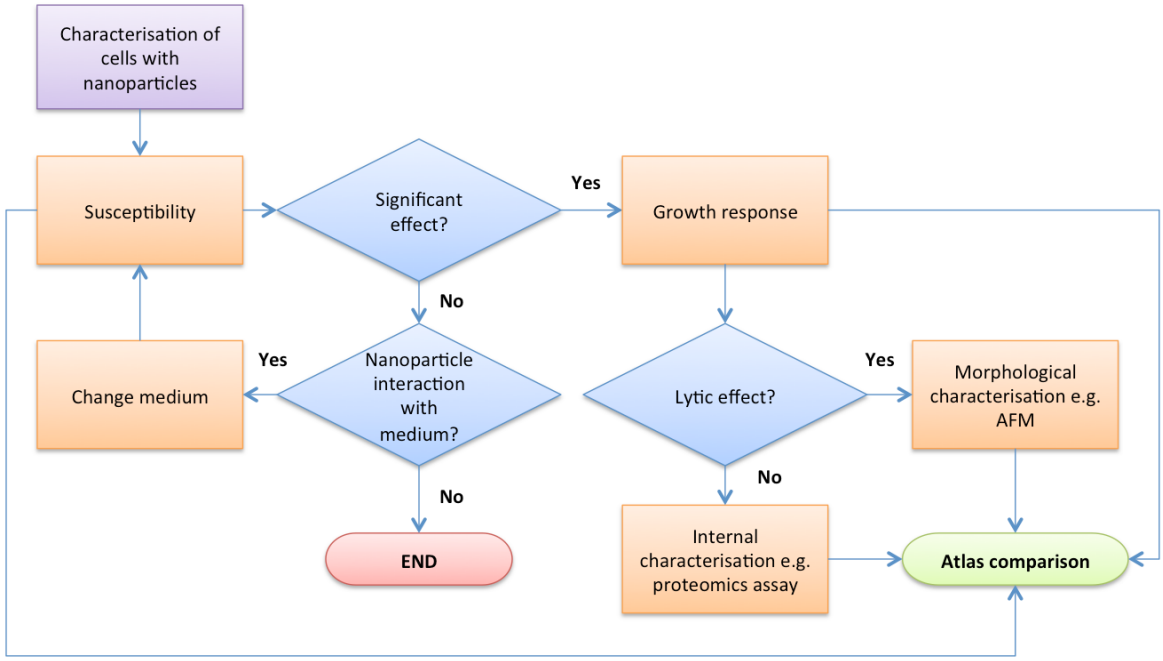

Figure 5.13 Flowchart for an updated methodology taking into account any interaction of a nanoparticle with the growth medium used and other characterisation techniques for internally affected bacteria.

While it was not possible to directly use the results of Chapter 4 for silver nanoparticles, other nanoparticles which may not interact with LB such as carbon fullerenes, nanotubes or dendrimeric nanostructures would present good candidates for quantitative comparison without the need for the SB medium.

Bacterial cells studied in this and the previous chapter were examined in air. The next chapter presents a novel AFM methodology to study the mechanical properties of live cells (bacteria and human red blood cells) in physiological conditions (liquid). This provides both an extension to the current work on bacteria (by imaging in liquid), opens up additional metrics for the atlas (mechanical properties) and marks the beginning of the examination of human cells (red blood cells) for nanomedical applications.

Chapter 6

Mechanical mapping of live cells

In the previous chapters a method to study the interactions of bacteria with nanomaterials and its application to E. coli *and silver nanoparticles were described. This chapter describes the collaborative work undertaken during this thesis to develop a means of measuring the mechanical properties of* live *cells at unprecedented spatial and temporal resolution using atomic force microscopy. This work was published in* Nature Nanotechnology *(Trigueros, Raman et al. 2011).*

Contributions: *Prof. Arvind Raman from the University of Purdue and Dr. Sonia Trigueros were lead authors and contributed equally to this work. Prof. Raman discovered the important experimental channels for material contrast. Dr. Trigueros, Alexander Cartagena (Purdue), the author and Prof. Raman developed experimental protocols for sample preparation. Prof. Raman, Dr. Trigueros and Dr. Sonia Contera conceived and designed the experiments. Prof. Raman developed the theory and A. Cartagena developed the code to implement the theory on the acquired AFM images. Prof. Raman, A. Cartagena, the author and Dr. Trigueros performed the experiments. Prof. Raman and Dr. Trigueros co-wrote the paper. All authors discussed the results and commented on the manuscript.*

6.1 Introduction

The previous chapters have described the development of a standard methodology to study nanoparticle/cell interactions, applied to *E. coli* and silver nanoparticles, where bacteria were dried and imaged in air. Biological systems are dynamic, complex and ultimately liquid systems. This chapter aims to extend the characterisation techniques used in previous chapters by studying cells in their natural, physiological state. The result of a collaboration between the Universities of Purdue and Oxford, this brief chapter outlines a new technique to measure the mechanical properties of live cells at the nanoscale. The mechanical properties of living cells at the nanoscale influence cellular

processes such as morphogenesis, metastasis and drug delivery and are of great interest for nanomedical applications (Nelson, Jean et al. 2005, Suresh 2007, McKendry 2012).

6.1.1 Measuring mechanical properties of cells

In addition to image acquisition, AFM can be used to acquire quantitative material properties of samples *via* force spectroscopy (Butt, Cappella et al. 2005). After calibration, the deflection (nN), amplitude (nm) and phase (degrees) of a probe can be recorded as a force curve, as the probe approaches (statically or dynamically), contacts and indents a sample. Calibration proceeds as follows:

1. The cantilever is tuned to its resonance frequency, thermally, acoustically and/or magnetically by measuring amplitude as a function of frequency until resonance is observed.
2. The inverse optical lever sensisibility (nm/V) to calibrate the measured cantilever deflection (V) with the deflection distance (nm) is calculated from a force curve on hard substrate, where the two quantities are linearly related.
3. The spring constant of the cantilever is calculated using e.g. the thermal noise method (Hutter and Bechhoefer 1993).

Through the choice of an appropriate contact model (e.g. Hertz, Sneddon, Chadwick) and probe parameters (e.g. tip radius and half cone angle, Poisson's ratio) the indentation of the probe can be related to the elastic modulus of the sample (Voïtchovsky, Antoranz Contera et al. 2006). By measuring force curves across a sample on a pixel-by-pixel basis a rudimentary force-volume map of sample mechanical properties can be obtained (Alsteens, Dupres et al. 2008). Due to the time taken to obtain a force curve at each point in the image, image resolution is typically on the order of 64 x 64 pixels, compared to imaging resolution of 256 x 256 pixels.

This use of single or multiple force curves to measure the elastic response of cells is slow and has limited spatial resolution (Radmacher, Fritz et al. 1996, Cross, Jin et al. 2007, Müller and Dufrêne 2011). A number of techniques which overcome these limitations to provide high temporal and/or spatial resolution mechanical mapping of cells require additional hardware or specialised data processing (Shekhawat and Dravid 2005, Jesse, Kalinin et al. 2007, Sahin and Erina 2008, Tetard, Passian et al. 2008). The method presented in this chapter is applicable to a standard commercial AFM and requires minimal data processing.

6.2 Materials and methods

The development of this novel multi-harmonic method relied on a number of key observations. During amplitude modulation atomic force microscopy imaging of soft samples in liquid, as the cantilever probe approaches the sample A_1 (the first harmonic amplitude, used as the setpoint channel) decreases as expected, and A_0 (the zeroth harmonic signal) increased significantly. For *E. coli* cells A_2 first increased and then decreases as a function of (decreasing) z (Trigueros, Raman et al. 2011). The presence of the harmonics A_0 and A_2 indicates non-linearity in the tip-sample interaction. The sample indentation δ_0 required for imaging is also greater than A_1, meaning that the probe is not tapping intermittently on the sample, but is in full contact for the duration of its cycle. Experimentally, A_0 and φ_1 were observed to correlate strongly with material contrast. Additionally, the cantilever dynamics near the sample in liquid were found to be distinct from those far away from the sample due to a hydrodynamic squeeze film effect (Arora, Rajwade et al. 2012).

Combining all these observations Prof. Raman developed a theory linking the Fourier coefficients of a tip-sample interaction force consisting of additively decomposed

conservative and dissipative tip-sample interactions with the experimentally observed quantities A_0, A_1, φ_1, A_2 and φ_2 to obtain the local stiffness k_{sample} (N/m), damping c_{sample} (Ns/m) and second order force gradient (N/m^2), in realtime. With an appropriate contact mechanics model (e.g. Hertz) the dynamic (storage and loss) elastic modulus can be obtained (Pa). A complete description of the methodology is available in the published work (Trigueros, Raman et al. 2011), and in particular its supplement which derives in detail the theoretical framework and assumptions made.

The method can be used using a conventional AFM with magnetically excited cantilevers, on live cells under physiological conditions at a temporal and spatial resolution far superior to current techniques (Table 6.1).

Reference	Sample	Resolution (pixels)	Acquisition time (min)
This work	*E. coli* DH5α	**65536**	**4**
This work	Human red blood cells	**65536**	**9**
(Plodinec, Loparic et al. 2011)	Rat fibroblasts	8192	150
(Alsteens, Dupres et al. 2008)	*S. cerevisiae*	1024	N/A
(Dupres, Menozzi et al. 2005)	*M. bovis*	1024	N/A
(Rotsch and Radmacher 2000)	Rat fibroblasts	4096	20
(Heinz and Hoh 1999)	Generic	4096	10-600

Table 6.1 Comparison of resolution and speed of alternative techniques used to map mechanical properties of live cells with the method developed here.

Experimentally, the procedure is as follows:

1. Tune and calibrate the cantilever to obtain the cantilever stiffness k.

2. Engage the sample and withdraw a short distance (a few μm). Ensure the resonance frequency is chosen so that $\varphi_{far} = 90°$ to validate the assumptions used for the forced steady state solution. Record Q_{far} and $A_{1,far}$.
3. Image the sample, recording A_0, φ_1, A_2 and φ_2.
4. After imaging, perform dynamic force curve on sample and a hard substrate, recording A_1 and A_0 as a function of z.
5. Mechanical maps can be obtained by processing the data in Matlab (scripts provided by Alexander Cartagena).

6.3 Results

6.3.1 Heterogeneity in *E. coli* cells imaged in PBS 1x

E. coli DH5α were imaged live by attaching cells to poly-l-lysine substrates in PBS 1x. Figure 6.1 shows the images and maps generated for a typical cell, highlighting heterogeneity in the stiffness and damping across the cell. This contrasts with the often smooth cell surface observed purely by topography – traditional AFM is limited in that the rich mechanical properties in additional to topography are unavailable in real time while scanning.

Differences in stiffness and damping on the cell surface across the cell have implications for studying the interactions of nanoparticles with cells: nanoparticles with mechanical mechanisms of actions such as carbon nanotubes will interact distinctly with different areas of cells (Liu, Wei et al. 2009).

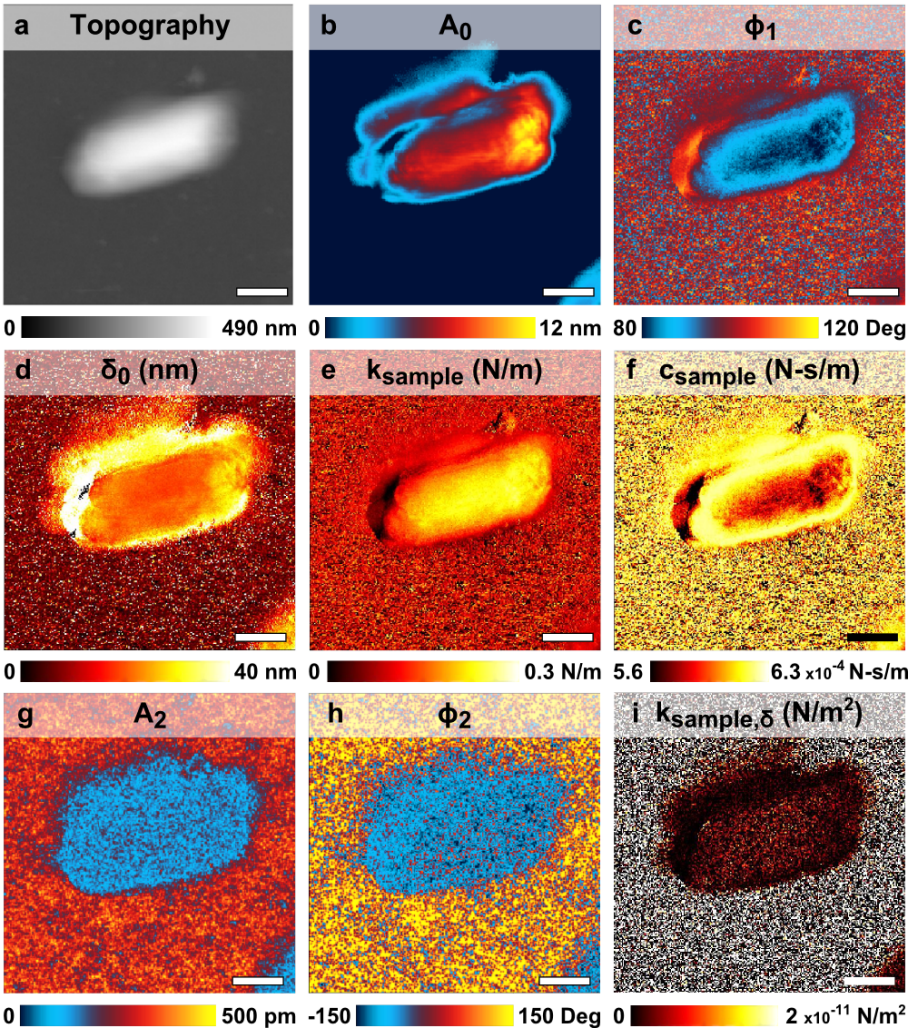

Figure 6.1 Multiharmonic images of *E. coli* bacteria. (**a**) Topography image of a live *E. coli* cell. (**b,c,g,h**) Maps of the multi-harmonic data $A_0, \varphi_1, A_2, \varphi_2$ acquired simultaneously with the topography, showing heterogeneities in local mechanical properties. (**d,e,f**) Maps of the mean indentation (nm), local dynamic stiffness (N/m) and damping (Ns/m). (**i**) Map of the local second order force gradient (N/m^2), which measures the extent of nonlinearity in the local tip–sample forces. Scale bar: 500 nm; 256 x 256 pixel image. The extracted property maps are only valid on the cell where the tip oscillation is small compared to the average indentation and not on the substrate where the tip intermittently taps on the sample.

6.3.2 Human red blood cells (RBC)

Human red blood cells have intrinsic mechanical properties that allow them to navigate the narrow capillaries of the body to deliver oxygen where needed (Dao, Lim et al. 2003). They are the also first point of contact for any nanomedical product inserted into the blood stream and thus a clinically important cell to study.

HRBC were soft compared to *E. coli* cells and required fresh preparation before imaging. Using poly-l-lysine coated slides in PBS 1x led to a non-biconcave morphology in AFM (Figure 6.2a). An increased stiffness at the core of the RBC compared to its periphery is in

line with its function in the human body, transporting oxygen through narrow capillaries where flexibility is required at its extremities.

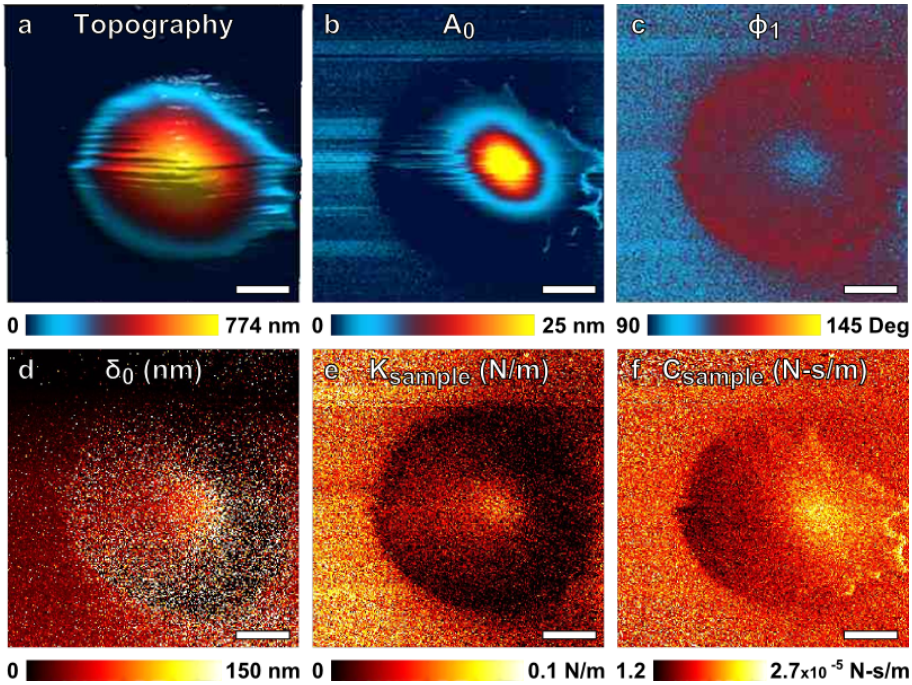

Figure 6.2 Multi-harmonic images of a human red blood cell. (**a**), Topography image of a live human red blood cell. (**b,c**) Maps of $\boldsymbol{A_0}$ and $\boldsymbol{\varphi_1}$, showing strong contrasts in local properties between the core and the periphery of the cell. (**d,e,f**) Maps of mean indentation, local dynamic spring constant and damping. Scale bar: 10 μm.

To explore why the cells lost their biconcave morphology, the effect of the imaging buffer was explored optically (Figure 6.3). RBC in serum (a) exhibited the expected biconcave shape, while cells in PBS 0.5x were swollen (b), due to the hypotonic conditions. Cells in PBS 1x (c) exhibited a predominantly crenate morphology as a result of hypertonic conditions, however cells with a biconcave morphology can also be observed. PBS 10x (d) induced a higher level of hypertonicity with all cells severely crenate, expected given the much higher salt concentration. Imaging in PBS 1x therefore precluded the biconcave morphology in the majority of cells. The morphology observed under AFM is likely due to the combined effects of buffer hypertonicity and adhesion between RBC and the polylysine surface (e).

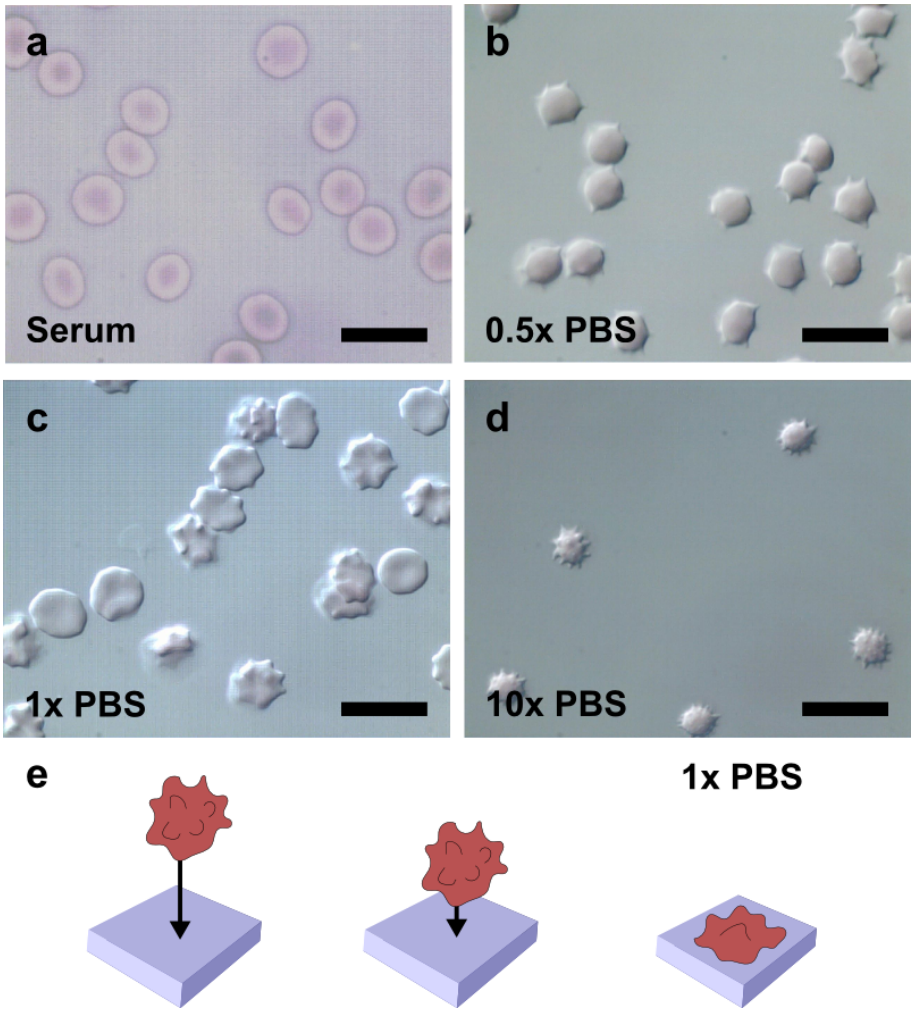

Figure 6.3 Optical investigation into effect of buffer medium isotonicity on RBC morphology. (**a**) Optical bright field image of red blood cells acquired with 100x oil immersion objective in Fetal Bovine Serum (Sigma-Aldrich, Dorset, UK) show the typical biconcave morphology of the cells. (**b,c,d**) Dark field images with differential interference contrast (DIC) of the red blood cells in 0.5x PBS, and 1x PBS, and 10x PBS buffers show different cell morphologies. (**e**) A model of red blood cell morphology when landing on glass in 1x PBS solution. Scale bar: 15 μm.

6.4 Conclusions and future directions

The method presented here is a powerful technique to quantitatively measure changes in mechanical properties in cells under physiological conditions in real time. It complements previous characterisation by AFM in that it provides quantitative measures for cells in aqueous conditions. The heterogeneities observed in *E. coli* are relevant to the work conducted in Chapter 4 – the cell wall is a mechanical structure and any effects by nanoparticles or drugs such as ampicillin, lysozyme and polymyxin B would be quickly visualised using this technique.

Chapter 7

Conclusions

A standard methodology to study the interaction of nanoparticles with cells was developed and tested. This involved characterising a range of silver based nanoparticles, developing the methodology, testing the methodology with silver nanoparticles and participating in the development of a novel characterisation technique for mapping the mechanical properties of live cells in liquid.

This thesis marks the beginning of the establishment of quantitative atlases to enable researchers to understand nanoparticle-cell interactions across a range of organisms, strains, cell culture mediums and nanoparticles – as long as adequate controls are established for each strain and medium used, and the protocols for the characterisation techniques followed precisely.

7.1 Stability of silver nanoparticles

In Chapter 3 the effects of three stabilising strategies on 14 nm diameter spherical silver nanoparticles synthesised using the citrate reduction method were reported. Silver nanoparticles capped with citrate alone were unstable over time due to aggregation. Their stability was enhanced through the addition of the polymer PEG due to a combination of steric repulsion between nanoparticles and the trapping of smaller seed

particles responsible for uncontrolled growth. The presence of the higher valence metals gold and chromium on the surface of the silver nanoparticles also improved their stability and heterogeneity in size and shape, due to the increased electrostatic affinity between citrate and gold/chromium as a function of valence. Silver-chromium were the most stable and homogenous nanoparticles due to the role of hexavalent Cr^{6+} ions in the growth and capping of the nanoparticles.

7.2 A standard methodology for nanoparticle/cell interactions

In Chapter 4 a comparative methodology to study nanoparticle/cell interactions was proposed and developed. The methodology involves the characterisation of the effects of well-known drugs on the cell of interest, resulting in a reference atlas. This atlas can then be compared against the effects of the cell with nanoparticles. *E. coli* DH5α were chosen as model cells, and the effects of kanamycin, ampicillin, polymyxin B and lysozyme were studied. Characterisation techniques included measuring susceptibility, population cell growth response, and morphology of cells by AFM. A protocol for imaging bacteria in air with minimal sample preparation was developed using agarose substrates. An optimal agarose concentration of 2% was selected for cells in the rich Luria-Bertani (LB) growth medium. Quantitative AFM analysis provided heights, widths, lengths and volumes of individual bacteria which could were compared via statistical testing.

Cells affected by kanamycin underwent a stationary phase in cell population response, with AFM analysis excluding damage to cell membranes highlighting the internal mechanism of action of the drug. No significant ($p < 0.05$) difference in heights was observed between cells affected by kanamycin and the control, indicated that no cell lysis occurred. Cells affected by ampicillin underwent cell lysis with the largest loss of volume observed. Cells affected by polymxyin B also underwent lysis but to a lesser extent than

ampicillin, due to the difference in their mechanisms of action: ampicillin ruptures peptidoglycan in the cell wall, whereas polymyxin B destabilises the outer and inner membranes resulting in leakage of cell contents. Finally lysozyme was studied, but only a small effect was observed in cell population growth response due to the lack of chelating agents added to aid the passage of lysozyme through the outer membrane. The high viscosity of affected cells observed prevented the collection of quantitative AFM data.

7.3 Interactions of silver nanoparticles with *E. coli*

Chapter 5 studied the interactions of silver ions, 10 nm and 30 nm silver nanoparticles using the methodology derived in Chapter 4. Initial susceptibility assays and cell population studies indicated that silver nanoparticles were non-toxic to bacteria, but it was found that silver interacted strongly with the bacterial growth medium LB, reducing available silver for interaction with the cells causing a false-negative result. An alteration to the characterisation techniques used for cells affected by silver nanoparticles was developed where a sodium bicarbonate (SB) buffer, which did not bind to silver, was used instead of LB (Xiu, Ma et al. 2011). Due to the lack of (silver-binding) nutrients in the new buffer, disk diffusion assays were not possible. Minimum bactericidal concentrations (MBC) for each nanoparticle were instead determined: silver ions, 10 nm and 30 nm silver nanoparticles required 0.15 μg/ml, 0.5 μg/ml and 3 μg/ml respectively to establish 100% cell death. Higher mass concentrations of nanoparticles were required compared to ions indicating an important role for free silver ions: when less ions were available (e.g. structured in a nanoparticle), bactericidal effects were reduced.

The absence of nutrients in the buffer required re-optimisation of the sample substrate: cell volumes were decreased compared to LB, and a concentration of 1% agarose (as opposed to 2%) was selected to minimise this effect. Qualitative AFM analysis did not

reveal dramatic alterations to cell morphology of cells affected by any of the silver treatments, although quantitative analysis revealed a significant ($p < 0.05$) decrease in heights of cells affected by silver ions and 30 nm silver nanoparticles, indicating loss of cell contents. Heights of cells were not significantly affected by 10 nm nanoparticles. These results indicate a size-specific interaction of silver nanoparticles: 10 nm nanoparticles did not affect cell heights, whereas silver ions and 30 nm nanoparticles reduced cell heights due to cell leakage. A quantitative comparison with the atlas of antibiotics in Chapter 4 was not possible due to the difference in medium and substrate used, although qualitatively silver nanoparticles were most similar in behaviour to kanamycin, which has an internal mechanism of action. This supports the literature for an ion-mediated internal mechanism of action of the nanoparticles as opposed to a nanoparticle-mediated external mechanism of disrupting the outer membrane and cell wall complex.

7.4 Mechanical mapping of live cells

Chapter 6 described a multi-harmonic AFM technique to map the mechanical properties of live cells under physiological conditions. This technique extends the work in Chapter 4 and 5 by imaging bacteria in liquid, and provides additional metrics for atlas characterisation such as stiffness and damping. This is particularly valuable for measuring nanoparticle-cell interactions where a mechanical mechanism of action is suspected such as with carbon nanotubes – changes to the mechanical properties of cells is available in real-time (Liu, Wei et al. 2009). The mechanical effect of drugs such as ampicillin and polymyxin B which destabilise the cell wall complex would also be measurable on live cells for the first time.

Finally, human red blood cells were investigated as a first step towards nanomedical applications on human cells.

7.5 Future work

7.5.1 Extending the atlas

The antibiotics used in developing the atlas in Chapter 4 targeted specific processes in the cytosol (kanamycin), periplasm (ampicillin and lysozyme) and outer and inner membranes (polymyxin B). Many other targets for antibiotics exist, and their characterisation would expand the current atlas to include other possible targets for nanomaterials, such as DNA and RNA transcription and replication (rifampicin, quinolones, metronidazole).

Including additional characterisation techniques to the methodology summarised at the end of Chapter 5 such as scanning electron microscopy, more specialised biochemical assays and the mechanical mapping technique from Chapter 6 would generate a wealth of additional information. Such information could be stored in a database accessible to other researchers who could access and submit their own characterisation datasets for the community at large.

7.5.2 Beyond silver

Silver nanoparticles frustrated the quantitative comparison of the reference atlas due to their interaction with growth medium used. Nanoparticles which do not interact with LB (potential candidates including carbon fullerenes, nanotubes, gold- and silica- based nanoparticles and quantum dots) could be promising candidates for reference with the specific atlas generated with *E. coli* DH5α.

7.5.3 Beyond *E. coli*

E. coli was studied in this thesis as a model gram negative organism. Additional atlases can now be created for other organisms such as the model gram positive bacterium *Staphylococcus aureus*, and pathological bacteria such as *Vibrio cholerae*, *Salmonella enterica*, *Mycobacterium tuberculosis* and many more. The inclusion of nitrifying bacteria would help assess the ecological impact of commercially produced nanoparticles entering the wastewater treatment system.

In Chapter 6 human red blood cells were imaged and quantitatively mapped. With the corresponding alterations to cell viability and population response assays other eukaryotic cell lines could be studied with the methodologies developed here, presenting an improved understanding of current nanoparticle exposure risks, but also testing new nanomedical treatments.

7.5.4 Establishing a database of atlases

With the establishment of a number of atlases, or a database of effects that can be statistically compared, a wide range of nanomaterials or drugs could be characterised and compared to the relevant atlas in a standardised way. Reproducibility would require use of exactly the same strains and media, but comparative differences measured as percentage differences between local controls and nanoparticle effects could be compared to the atlases where environmental factors such as temperature, humidity and media content differ.

As the number of cells, strains, targets and mechanisms of actions available in the atlases increase, so will the possibilities for testing new materials, which would be of great value to the scientific community.

Publications and conferences

Publications

S. Trigueros*, A. Raman*, A. Cartagena, A. P. Z. Stevenson, M. Susilo, E. Nauman, S. Antoranz Contera (2011) Mapping nanomechanical properties of live cells using multi-harmonic atomic force microscopy. *Nature Nanotechnology* **6**, 809;

A. P. Z. Stevenson, D. Blanco Bea, S. Civit, S. Antoranz Contera, A. Iglesias Cerveto, S. Trigueros (2012) Three strategies to stabilise nearly monodisperse silver nanoparticles in aqueous solution. *Nanoscale Research Letters* **7**,151.

Invited talks

A. P. Z. Stevenson, D. Blanco Bea, S. Trigueros (September 2012) A multidisciplinary approach for studying nanostructure/cell structures. *4th International Seminar of Nanoscience and Nanotechnology, Havana, Cuba*.

Conferences

A. P. Z. Stevenson, D. Blanco Bea, S. Antoranz Contera, A. Iglesias Cerveto, S. Trigueros (2010) Monodisperse silver nanoparticles of controlled size for biomedical applications. *2010 International Conference on Solid State Devices and Materials, Tokyo, Japan.*

Appendix A

Bootstrap analysis

This chapter includes additional information on the bootstrap analysis of nanoparticle heights and diameters, provided by Dr. Sergi Civit at the University of Barcelona.

A.1 Introduction

Bootstrapping is a very useful tool in statistics in cases when there is doubt that distributional assumptions and asymptotic results are valid and accurate (Efron and Tibshirani 1993). The fundamental concept in bootstrapping is in building a sampling distribution for a particular statistic by resampling from the data at hand. Based on the two independent samples obtained by TEM and AFM, nanoparticle sphericity was modelled by constructing an ellipse with diameter from TEM and height from AFM, and calculate the corresponding statistic eccentricity (ε, eq. (1.2)):

$$\varepsilon = \sqrt{\frac{a^2 - b^2}{a^2}} = \sqrt{1 - \left(\frac{b}{a}\right)^2} \tag{7.1}$$

where a and b are an ellipse's half major and minor axes (diameter and height) respectively.

The eccentricity of an ellipse is a measure of how circular the ellipse is. As the eccentricity value ranges from 0 to 1, the ellipse ranges from circular to highly elongated. According to eq. (1.2) and non-parametric bootstrap techniques (B = 1000 resampling) the distribution of the bootstrapped statistic was obtained. Due to the presence of extreme

values in the dataset bootstrapping was performed by weighting frequency values. In other words, once the value becomes extreme enough, the weight for that observation becomes very small in the resampling procedure so the influence of the observation is minimal. These weights are the relative frequencies of particle diameters from TEM and particle heights from AFM.

In addition, the question of interest "How spherical are the nanoparticles synthesised in this study?" is addressed according to the the Kruskal-Wallis hypothesis test. The Kruskal-Wallis test is the non-parametric analog to One-way Analysis of Variance. This test is used to determine if there are "significant" differences among the population medians (instead of the population means). The Kruskal-Wallis H statistic is an overall test statistic that enables one to test the general hypothesis that all population medians are equal. However, the investigator is not extremely interested in this general hypothesis but is interested in comparisons amongst the individual groups. According to that nanoparticle types were compared to establish a ranking of eccentricity, and hence sphericity (where a low eccentricity corresponds to a high sphericity). Silver-chromium alloy nanoparticles were found to be the most spherical, followed by the silver-gold nanoshells, PEG-functionalised silver and finally pure silver nanoparticles (Table A.1).

Eccentricity (e) test:

Kruskal-Wallis: Multiple Comparisons

Kruskal-Wallis Test on the data

Group	N	Median	Ave Rank	Z
AgCr	1000	0.7741	1706.8	-9.29
Ag	1000	0.8584	2249.0	7.86
AgPEG	1000	0.8522	2263.4	8.31
AgAu	1000	0.7805	1782.9	-6.88
Overall	4000		2000.5	

H = 198.31 DF = 3 **P = 0.000**
H = 198.31 DF = 3 P = 0.000 (adjusted for ties)

Kruskal-Wallis: All Pairwise Comparisons

```
----------------------------------------

Comparisons:                    6
Ties:                           73
Family Alpha:                   0.2
Bonferroni Individual Alpha:    0.033
Bonferroni Z-value (2-sided):   2.128

Sign confidence interval for median

                                  Confidence
                       Achieved     Interval
          N  Median  Confidence   Lower   Upper  Position
AgCr   1000  0.7741      0.8628  0.7551  0.7830       477
                        0.8676  0.7551  0.7832       NLI
                        0.8787  0.7550  0.7838       476
Ag     1000  0.8584      0.8628  0.8479  0.8689       477
                        0.8676  0.8478  0.8691       NLI
                        0.8787  0.8476  0.8695       476
AgPEG  1000  0.8522      0.8628  0.8451  0.8638       477
                        0.8676  0.8451  0.8639       NLI
                        0.8787  0.8451  0.8640       476
AgAu   1000  0.7805      0.8628  0.7694  0.7931       477
                        0.8676  0.7693  0.7934       NLI
                        0.8787  0.7690  0.7941       476
```

Kruskal-Wallis: Conclusions

```
The following groups showed significant differences (adjusted for ties):

Groups                  Z vs. Critical value       P-value
AgCr vs. AgPEG          10.7775 >= 2.128           0.000
AgCr vs. Ag             10.4985 >= 2.128           0.000
AgPEG vs. AgAu           9.3035 >= 2.128           0.000
Ag vs. AgAu              9.0245 >= 2.128           0.000

The graph displays boxplots of the groups with their sign confidence intervals
for the medians. This graph is extremely useful because you can visually see the
eccentricity values of the nanoparticles with respect to the others (a low
eccentricity corresponds to a high sphericity)
```

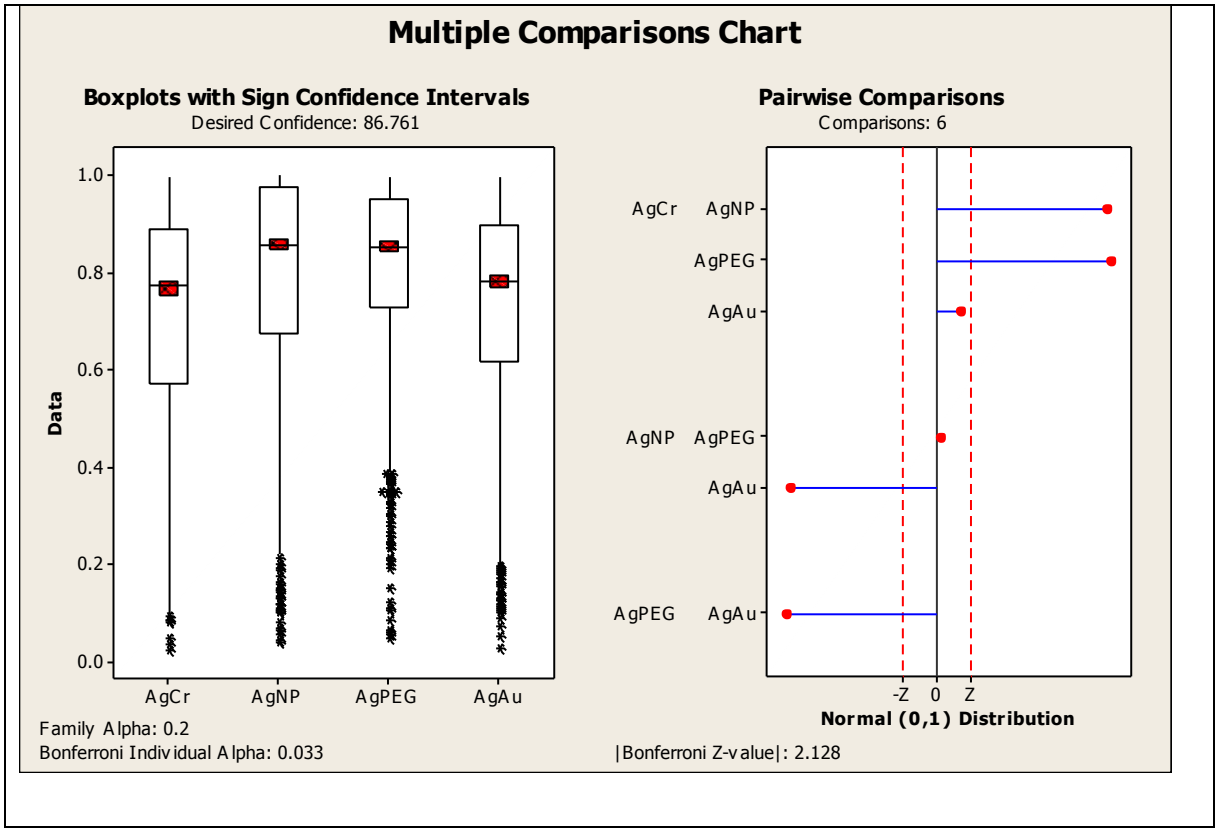

Table A.1 Kruskal Wallis hypothesis test and Multiple comparisons (significance level= 0.05)

Appendix B

Hypothesis testing

This chapter includes full statistical testing results from Chapters 4 and 5. The Control *dataset contains measurements from control E. coli on glass, 1%, 2% and 4% agarose. The* LB *dataset contains measurements from E. coli on 2% agarose in LB medium: control, kanamycin, ampicillin* t_1 *and* t_2 *and polymyxin B* t_1 *and* t_2*. The* bicarb *dataset contains measurements for E. coli on 1% agarose in sodium bicarbonate buffer (SB): control, silver ions (Ag+), 10 nm silver nanoparticles (AgNP_10) and 30 nm silver nanoparticles (AgNP_30).*

B.1 Global testing

Global analysis of variance (ANOVA) tests were performed to establish differences between treatments on the bacteria metrics: height, width, length and volume. ANOVA assumes sample data is normally distributed (tested with the Shapiro-Wilk (SW) test on residuals) and that sample variances are equal (tested with Bartlett's (B) test). If these assumptions were invalid (either test reporting a p-value < 0.05) the non-parametric Kruskal-Wallis (KW) test was applied.

In both cases, the null hypothesis is that all samples within each dataset were drawn from the same parent distribution, and that any differences between means (parametric) or medians (non-parametric) are statistically insignificant. A p-value < 0.05 would constitute a rejection of the null hypothesis, and require further analysis using post-hoc analysis (Sections B.2 and B.3).

Control	Height	Width	Length	Volume
SW	0.5562015	0.08143222	0.4999075	0.2547242
B	0.05501307	0.6115711	0.2887924	0.1246872
ANOVA	**4.820571e-18**	**0.0007645979**	**0.003349759**	0.1568405
LB				
SW	0.03409097	0.3834045	0.3161996	0.06261774
B	4.245994e-07	1.153134e-06	0.6527316	0.004473686
ANOVA/KW	**1.429916e-10**	**0.004004665**	**0.0004152984**	**1.248271e-07**
Bicarb				
SW	0.5011855	0.7373723	0.4046079	0.5904589
B	0.1591371	0.3074194	0.9107035	0.5953237
ANOVA	**1.915068e-05**	**0.0004552544**	0.3492938	**0.004314604**

Table B.1 p-values for parametric (ANOVA) and non-parametric (KW) global tests for differences between means or medians for each dataset. Shapiro-Wilk (SW) and Bartlett's (B) tests for normality were used to verify that assumptions for parametric testing were robust. If either a SW or B test failed, the non-parametric KW test result is listed. p-values below the 0.05 significance level are highlighted in red.

B.2 Parametric post-hoc testing

Once a global test (Section B.1) has established differences between means or medians within groups, post-hoc analysis allows multiple comparisons to be made between the groups in each dataset. Tukey's Honest Significance Difference was used to establish which (parametric) samples differed for each metric and dataset whose p-value was below 0.05.

```
  Tukey multiple comparisons of means
    95% family-wise confidence level

#########################
 controls Height
#########################
                              diff       lwr       upr    p adj
glass-four_percent         19.28024  10.35086  28.20962 6.2e-06
one_percent-four_percent   62.98038  52.44198  73.51877 0.0e+00
two_percent-four_percent   39.72973  30.43573  49.02372 0.0e+00
one_percent-glass          43.70013  33.48185  53.91842 0.0e+00
two_percent-glass          20.44948  11.52010  29.37886 2.1e-06
two_percent-one_percent   -23.25065 -33.78905 -12.71225 4.2e-06
#########################
 controls Width
#########################
```

```
                                 diff         lwr         upr     p adj
glass-four_percent        0.073776224  0.02146199  0.12609045 0.0028398
one_percent-four_percent  0.039281169 -0.02245975  0.10102209 0.3331211
two_percent-four_percent -0.002727273 -0.05717765  0.05172310 0.9991143
one_percent-glass        -0.034495055 -0.09436054  0.02537043 0.4198628
two_percent-glass        -0.076503497 -0.12881773 -0.02418927 0.0019023
two_percent-one_percent  -0.042008442 -0.10374936  0.01973248 0.2763881
#########################
 controls Length
#########################
                               diff       lwr          upr     p adj
glass-four_percent       -0.6500699 -1.483220  0.18308047 0.1727367
one_percent-four_percent -0.8869260 -1.870205  0.09635287 0.0897256
two_percent-four_percent -1.2763636 -2.143534 -0.40919320 0.0017674
one_percent-glass        -0.2368560 -1.190267  0.71655484 0.9086884
two_percent-glass        -0.6262937 -1.459444  0.20685670 0.1988651
two_percent-one_percent  -0.3894377 -1.372717  0.59384118 0.7131541
#########################
 lb Length
#########################
                          diff         lwr        upr     p adj
amp_t2-amp_t1        0.3798205 -0.73826978  1.4979108 0.9180699
kan-amp_t1           0.8741640 -0.17536430  1.9236922 0.1568574
pol_t1-amp_t1        1.0022388  0.07193146  1.9325462 0.0273420
pol_t2-amp_t1        0.7053761 -0.31725700  1.7280092 0.3414179
two_percent-amp_t1 -0.5421997 -1.59172793  0.5073286 0.6570589
kan-amp_t2           0.4943434 -0.72473970  1.7134266 0.8412677
pol_t1-amp_t2        0.6224183 -0.49567200  1.7405086 0.5814893
pol_t2-amp_t2        0.3255556 -0.87045136  1.5215625 0.9670917
two_percent-amp_t2 -0.9220202 -2.14110334  0.2970629 0.2438498
pol_t1-kan           0.1280749 -0.92145339  1.1776031 0.9992023
pol_t2-kan          -0.1687879 -1.30096109  0.9633853 0.9979077
two_percent-kan     -1.4163636 -2.57288745 -0.2598398 0.0077380
pol_t2-pol_t1       -0.2968627 -1.31949583  0.7257703 0.9567635
two_percent-pol_t1 -1.5444385 -2.59396676 -0.4949102 0.0007110
two_percent-pol_t2 -1.2475758 -2.37974897 -0.1154025 0.0223629
#########################
 bicarb Height
#########################
                    diff        lwr      upr     p adj
AgNP_30-Ag+         9.009844  -9.062178 27.08187 0.5526072
AgNP_10-Ag+        27.305923  11.841240 42.77061 0.0001175
bicarb-Ag+         27.478659  10.673994 44.28332 0.0003746
AgNP_10-AgNP_30    18.296078   3.397520 33.19464 0.0103153
bicarb-AgNP_30     18.468814   2.183625 34.75400 0.0203548
bicarb-AgNP_10      0.172736 -13.160149 13.50562 0.9999852
#########################
 bicarb Width
#########################
                        diff         lwr         upr     p adj
```

```
AgNP_30-Ag+       -0.091917333 -0.16774555 -0.01608911 0.0116006
AgNP_10-Ag+       -0.107325507 -0.17221362 -0.04243740 0.0003176
bicarb-Ag+        -0.103942976 -0.17445350 -0.03343245 0.0014789
AgNP_10-AgNP_30   -0.015408174 -0.07792089  0.04710454 0.9136078
bicarb-AgNP_30    -0.012025643 -0.08035651  0.05630522 0.9659160
bicarb-AgNP_10     0.003382531 -0.05256079  0.05932585 0.9985096
#########################
 bicarb Volume
#########################
                      diff          lwr        upr     p adj
AgNP_30-Ag+       -0.02022222 -0.136182200 0.09573776 0.9667872
AgNP_10-Ag+        0.05125604 -0.047973825 0.15048590 0.5229606
bicarb-Ag+         0.11692063  0.009092716 0.22474855 0.0287072
AgNP_10-AgNP_30    0.07147826 -0.024119040 0.16707556 0.2070069
bicarb-AgNP_30     0.13714286  0.032648177 0.24163754 0.0054306
bicarb-AgNP_10     0.06566460 -0.019886485 0.15121568 0.1878035
```

Table B.2 p-values for parametric multiple comparisons between samples. p-values < 0.05 are highlighted in red and indicate statistically significant differences between the corresponding samples.

B.3 Non-parametric post-hoc testing

Multiple comparisons between samples in non-normally distributed datasets were conducted using a Kruskal-Wallis framework (Siegel and Castellan 1998).

```
Multiple comparison test after Kruskal-Wallis
p.value: 0.05

#########################
 lb Height
#########################
                     obs.dif critical.dif difference
amp_t1-amp_t2       3.604575     27.06952      FALSE
amp_t1-kan         40.473262     25.40960       TRUE
amp_t1-pol_t1      20.000000     22.52321      FALSE
amp_t1-pol_t2      24.715686     24.75846      FALSE
amp_t1-two_percent 55.382353     25.40960       TRUE
amp_t2-kan         36.868687     29.51461       TRUE
amp_t2-pol_t1      16.395425     27.06952      FALSE
amp_t2-pol_t2      21.111111     28.95592      FALSE
amp_t2-two_percent 51.777778     29.51461       TRUE
kan-pol_t1         20.473262     25.40960      FALSE
kan-pol_t2         15.757576     27.41048      FALSE
kan-two_percent    14.909091     28.00002      FALSE
pol_t1-pol_t2       4.715686     24.75846      FALSE
pol_t1-two_percent 35.382353     25.40960       TRUE
pol_t2-two_percent 30.666667     27.41048       TRUE
#########################
 lb Width
#########################
```

	obs.dif	critical.dif	difference
amp_t1-amp_t2	1.7908497	27.06952	FALSE
amp_t1-kan	21.4171123	25.40960	FALSE
amp_t1-pol_t1	20.3823529	22.52321	FALSE
amp_t1-pol_t2	2.4852941	24.75846	FALSE
amp_t1-two_percent	6.4465241	25.40960	FALSE
amp_t2-kan	19.6262626	29.51461	FALSE
amp_t2-pol_t1	18.5915033	27.06952	FALSE
amp_t2-pol_t2	0.6944444	28.95592	FALSE
amp_t2-two_percent	8.2373737	29.51461	FALSE
kan-pol_t1	1.0347594	25.40960	FALSE
kan-pol_t2	18.9318182	27.41048	FALSE
kan-two_percent	27.8636364	28.00002	FALSE
pol_t1-pol_t2	17.8970588	24.75846	FALSE
pol_t1-two_percent	26.8288770	25.40960	TRUE
pol_t2-two_percent	8.9318182	27.41048	FALSE

##########################

lb Volume

##########################

	obs.dif	critical.dif	difference
amp_t1-amp_t2	5.228758	27.06952	FALSE
amp_t1-kan	46.117647	25.40960	TRUE
amp_t1-pol_t1	29.852941	22.52321	TRUE
amp_t1-pol_t2	28.825980	24.75846	TRUE
amp_t1-two_percent	33.844920	25.40960	TRUE
amp_t2-kan	40.888889	29.51461	TRUE
amp_t2-pol_t1	24.624183	27.06952	FALSE
amp_t2-pol_t2	23.597222	28.95592	FALSE
amp_t2-two_percent	28.616162	29.51461	FALSE
kan-pol_t1	16.264706	25.40960	FALSE
kan-pol_t2	17.291667	27.41048	FALSE
kan-two_percent	12.272727	28.00002	FALSE
pol_t1-pol_t2	1.026961	24.75846	FALSE
pol_t1-two_percent	3.991979	25.40960	FALSE
pol_t2-two_percent	5.018939	27.41048	FALSE

Table B.3 p-values for non-parametric multiple comparisons between samples. Significant differences between samples are highlighted in red.

Bibliography

Adrian, M., J. Dubochet, J. Lepault and A. W. McDowall (1984). "Cryo-electron microscopy of viruses." Nature **308**(5954): 32-36.

Aherne, D., D. M. Ledwith, M. Gara and J. M. Kelly (2008). "Optical Properties and Growth Aspects of Silver Nanoprisms Produced by a Highly Reproducible and Rapid Synthesis at Room Temperature." Advanced Functional Materials **18**(14): 2005-2016.

Alivisatos, A. P. (1996). "Semiconductor Clusters , Nanocrystals , and Quantum Dots." Science **271**(5251): 933-937.

Alsteens, D., V. Dupres, K. M. C. Evoy, L. Wildling, H. J. Gruber and Y. F. Dufrêne (2008). "Structure, cell wall elasticity and polysaccharide properties of living yeast cells, as probed by AFM." Yeast **19**(38).

Amato, E., Y. A. Diaz-Fernandez, A. Taglietti, P. Pallavicini, L. Pasotti, L. Cucca, C. Milanese, P. Grisoli, C. Dacarro, J. M. Fernandez-Hechavarria and V. Necchi (2011). "Synthesis, characterization and antibacterial activity against Gram positive and Gram negative bacteria of biomimetically coated silver nanoparticles." Langmuir **27**(15): 9165-9173.

AMMRF. (2013). "SEM layout and function." Retrieved 19/09/13, from http://www.ammrf.org.au/myscope/sem/practice/principles/layout.php.

Ando, T., N. Kodera, E. Takai, D. Maruyama, K. Saito and A. Toda (2001). "A high-speed atomic force microscope for studying biological macromolecules." Proceedings of the National Academy of Sciences of the United States of America **98**(22): 12468-12472.

Andrews, J. M. (2001). "Determination of minimum inhibitory concentrations." The Journal of Antimicrobial Chemotherapy **48 Suppl 1**: 5-16.

Arbain, R., M. Othman and S. Palaniandy (2011). "Preparation of iron oxide nanoparticles by mechanical milling." Minerals Engineering **24**(1): 1-9.

Arora, S., J. M. Rajwade and K. M. Paknikar (2012). "Nanotoxicology and in vitro studies: the need of the hour." Toxicology and Applied Pharmacology **258**(2): 151-165.

Autumn, K., Y. A. Liang, S. T. Hsieh, W. Zesch, W. P. Chan, T. W. Kenny, R. Fearing and R. J. Full (2000). "Adhesive force of a single gecko foot-hair." Nature **405**(6787): 681-685.

Berman, E. (1980). Toxic metals and their analysis. Heyden.

Bernhard, W. (1969). "A new staining procedure for electron microscopical cytology." Journal of Ultrastructure Research **27**(3–4): 250-265.

Betzig, E., G. H. Patterson, R. Sougrat, O. W. Lindwasser, S. Olenych, J. S. Bonifacino, M. W. Davidson, J. Lippincott-Schwartz and H. F. Hess (2006). "Imaging Intracellular Fluorescent Proteins at Nanometer Resolution." Science **313**(5793): 1642-1645.

Beveridge, T. J. (2001). "Use of the Gram stain in microbiology." Biotechnic & Histochemistry **76**(3): 111-118.

Binnig, G., C. F. Quate and C. Gerber (1986). "Atomic force microscope." Physical Review Letters **56**(9).

Binnig, G., H. Rohrer, C. Gerber and E. Weibel (1982). "Surface studies by scanning tunneling microscopy." Physical Review Letters **49**(1): 57-61.

Binnig, G., H. Rohrer, C. Gerber and E. Weibel (1982). "Tunneling through a controllable vacuum gap." Applied Physics Letters **40**(2): 178-180.

Bishop, K. J. M., C. E. Wilmer, S. Soh and B. A. Grzybowski (2009). "Nanoscale Forces and Their Uses in Self-Assembly." Small **5**(14): 1600-1630.

Bohren, C. F. and D. R. Huffman (1998). Absorption and Scattering of Light by Small Particles. John Wiley & Sons.

Bolshakova, A. V., O. I. Kiselyova and I. V. Yaminsky (2004). "Microbial Surfaces Investigated Using Atomic Force Microscopy." Biotechnology Progress **20**(6): 1615-1622.

Borm, P. J. A., D. Robbins, S. Haubold, T. Kuhlbusch, H. Fissan, K. Donaldson, R. Schins, V. Stone, W. Kreyling, J. Lademann, J. Krutmann, D. Warheit and E. Oberdorster (2006). "The potential risks of nanomaterials: a review carried out for ECETOC." Particle and Fibre Toxicology **3**(11).

Boulos, L., M. Prévost, B. Barbeau, J. Coallier and R. Desjardins (1999). "LIVE/DEAD® BacLight™: application of a new rapid staining method for direct enumeration of viable and total bacteria in drinking water." Journal of Microbiological Methods **37**(1): 77-86.

Bragg, P. D. and D. J. Rainnie (1974). "The effect of silver ions on the respiratory chain of Escherichia coli." Canadian Journal of Microbiology **20**(6): 883-889.

Buguin, a., O. Du Roure and P. Silberzan (2001). "Active atomic force microscopy cantilevers for imaging in liquids." Applied Physics Letters **78**(19): 2982-2982.

Butt, H., B. Cappella and M. Kappl (2005). "Force measurements with the atomic force microscope: Technique, interpretation and applications." Surface Science Reports **59**(1-6): 1-152.

Chanyawadee, S., R. T. Harley, M. Henini, D. V. Talapin and P. G. Lagoudakis (2009). "Photocurrent Enhancement in Hybrid Nanocrystal Quantum-Dot p-i-n Photovoltaic Devices." Physical Review Letters **102**(7): 077402-077404.

Chen, B., X. Jiao and D. Chen (2010). "Size-Controlled and Size-Designed Synthesis of Nano/Submicrometer Ag Particles." Crystal Growth & Design **10**(8): 3378-3386.

Chen, X., A. Kis, A. Zettl and C. R. Bertozzi (2007). "A cell nanoinjector based on carbon nanotubes." Proceedings of the National Academy of Sciences of the United States of America **104**(20): 8218-8222.

Choi, O., K. K. Deng, N.-J. Kim, L. Ross, R. Y. Surampalli and Z. Hu (2008). "The inhibitory effects of silver nanoparticles, silver ions, and silver chloride colloids on microbial growth." Water Research **42**(12): 3066-3074.

Cleveland, J. P. (1998). "Energy dissipation in tapping-mode atomic force microscopy." Applied Physics Letters **59**(20): 2171-2171.

Coleman, J. N., U. Khan, W. J. Blau and Y. K. Gun'ko (2006). "Small but strong: A review of the mechanical properties of carbon nanotube–polymer composites." Carbon **44**(9): 1624-1652.

Colvin, V. L., M. C. Schlamp and A. P. Alivisatos (1994). "Light-emitting diodes made from cadmium selenide nanocrystals and a semiconducting polymer." Nature **370**(6488): 354-357.

Cross, S. E., Y.-S. Jin, J. Rao and J. K. Gimzewski (2007). "Nanomechanical analysis of cells from cancer patients." Nature Nanotechnology **2**(12): 780-783.

Dahl, J. (2012). "Gram negative cell wall." Retrieved 07/11/12, from http://upload.wikimedia.org/wikipedia/commons/8/8b/Gram_negative_cell_wall.svg.

Danilatos, G. (1994). "Environmental scanning electron microscopy and microanalysis." Microchimica Acta **114-115**(1): 143-155.

Dao, M., C. T. Lim and S. Suresh (2003). "Mechanics of the human red blood cell deformed by optical tweezers." Journal of the Mechanics and Physics of Solids **51**(11–12): 2259-2280.

Davies, C. W. and A. L. Jones (1949). "The precipitation of silver chloride from aqueous solutions. Part I." Discussions of the Faraday Society **5**(0): 103-111.

Davis, B. D. (1987). "Mechanism of bactericidal action of aminoglycosides." Microbiological reviews **51**(3): 341-350.

de Andrade Rosa, I., W. de Souza and M. Benchimol (2013). "High-resolution scanning electron microscopy of the cytoskeleton of Tritrichomonas foetus." Journal of Structural Biology **183**(3): 412-418.

Dickerson, E. B., E. C. Dreaden, X. Huang, I. H. El-Sayed, H. Chu, S. Pushpanketh, J. F. McDonald and M. A. El-Sayed (2008). "Gold nanorod assisted near-infrared plasmonic photothermal therapy (PPTT) of squamous cell carcinoma in mice." Cancer Letters **269**(1): 57-66.

Donaldson, K., V. Stone, C. L. Tran, W. Kreyling and P. J. a. Borm (2004). "Nanotoxicology." Occupational and Environmental Medicine **61**(9): 727-728.

Dong, X., X. Ji, H. Wu, L. Zhao, J. Li and W. Yang (2009). "Shape Control of Silver Nanoparticles by Stepwise Citrate Reduction." The Journal of Physical Chemistry C **113**(16): 6573-6576.

Dransfield, G. P. (2000). "Inorganic Sunscreens." Radiation Protection Dosimetry **91**(1-3): 271-273.

Dundee, U. o. (2007). "Figure 4: Transmission electron microscopy (TEM)." Retrieved 23/10/12, from http://learning.covcollege.ac.uk/content/Jorum/MIC_Specimen-prep-and-basic-microscopy-skills-LM1.2-3Feb08/page13.htm.

Dupres, V., F. D. Menozzi, C. Locht, B. H. Clare, N. L. Abbott, C. Bompard, D. Raze and Y. F. Dufrêne (2005). "Nanoscale mapping and functional analysis of individual adhesins on living bacteria." Nature Methods **2**(7): 515-521.

Dusemund, B., A. Hoffmann, T. Salzmann, U. Kreibig and G. Schmid (1991). "Cluster matter : the transition of optical elastic scattering to regular reflection." Zeitschrift für Physik D Atoms, Molecules and Clusters **20**(1): 305-308.

Edwards, C. (1990). Microbiology of Extreme Environments. Open University Press.

Efron, B. and R. J. Tibshirani (1993). An introduction to the Bootstrap. Chapmann & Hall.

Eigler, D. M. and E. K. Schweizer (1990). "Positioning single atoms with a scanning tunnelling microscope." Nature **344**(6266): 524-526.

Elghanian, R. (1997). "Selective Colorimetric Detection of Polynucleotides Based on the Distance-Dependent Optical Properties of Gold Nanoparticles." Science **277**(5329): 1078-1081.

Ellison, R. T. and T. J. Giehl (1991). "Killing of gram-negative bacteria by lactoferrin and lysozyme." The Journal of Clinical Investigation **88**(4): 1080-1091.

Engel, Y., R. Elnathan, A. Pevzner, G. Davidi, E. Flaxer and F. Patolsky (2010). "Supersensitive Detection of Explosives by Silicon Nanowire Arrays." Angewandte Chemie International Edition **49**(38): 6830-6835.

Englebienne, P. (1998). "Use of colloidal gold surface plasmon resonance peak shift to infer affinity constants from the interactions between protein antigens and antibodies specific for single or multiple epitopes." The Analyst **123**(7): 1599-1603.

Fadeel, B. and A. E. Garcia-Bennett (2010). "Better safe than sorry: Understanding the toxicological properties of inorganic nanoparticles manufactured for biomedical applications." Advanced Drug Delivery Reviews **62**(3): 362-374.

Fahnestock, K. J., M. Manesse, H. A. McIlwee, C. L. Schauer, R. Boukherroub and S. Szunerits (2009). "Selective detection of hexachromium ions by localized surface plasmon

resonance measurements using gold nanoparticles/chitosan composite interfaces." The Analyst **134**(5): 881-886.

Fantner, G. E., G. Schitter, J. H. Kindt, T. Ivanov, K. Ivanova, R. Patel, N. Holten-Andersen, J. Adams, P. J. Thurner, I. W. Rangelow and P. K. Hansma (2006). "Components for high speed atomic force microscopy." Ultramicroscopy **106**(8–9): 881-887.

Faraday, M. (1857). "The Bakerian Lecture: Experimental Relations of Gold (and Other Metals) to Light." Philosophical Transactions of the Royal Society of London **147**: 145-181.

Farkas, J., P. Christian, J. A. Gallego-Urrea, N. Roos, M. Hassellöv, K. E. Tollefsen and K. V. Thomas (2011). "Uptake and effects of manufactured silver nanoparticles in rainbow trout (Oncorhynchus mykiss) gill cells." Aquatic Toxicology **101**(1): 117-125.

Feldmann, C. and H.-O. Jungk (2001). "Polyol-Mediated Preparation of Nanoscale Oxide Particles." Angewandte Chemie International Edition **40**(2): 359-362.

Feng, Q. L., J. Wu, G. Q. Chen, F. Z. Cui, T. N. Kim and J. O. Kim (2000). "A mechanistic study of the antibacterial effect of silver ions on Escherichia coli and Staphylococcus aureus." Journal of Biomedical Materials Research **52**(4): 662-668.

Fernández-Morán, H. (1952). "The submicroscopic organization of vertebrate nerve fibres: An electron microscope study of myelinated and unmyelinated nerve fibres." Experimental Cell Research **3**(2): 282-359.

Ferrari, M. (2005). "Cancer nanotechnology: opportunities and challenges." Nature Reviews Cancer **5**(3): 161-171.

Feynman, R. P. (1960). "Plenty of room at the bottom." Engineering and Science **23**(5): 22-36.

Fischer, H. C. and W. C. W. Chan (2007). "Nanotoxicity: the growing need for in vivo study." Current Opinion in Biotechnology **18**(6): 565-571.

Flick, D. F., H. F. Kraybill and J. M. Dimitroff (1971). "Toxic effects of cadmium: A review." Environmental Research **4**(2): 71-85.

Fratzl, P., H. S. Gupta, E. P. Paschalis and P. Roschger (2004). "Structure and mechanical quality of the collagen-mineral nano-composite in bone." Journal of Materials Chemistry **14**(14): 2115-2123.

Frens, G. (1973). "Controlled nucleation for the regulation of the particle size in monodisperse gold suspensions." Nature Physical Science **241**(105): 20-22.

Gao, X., Y. Cui, R. M. Levenson, L. W. K. Chung and S. Nie (2004). "In vivo cancer targeting and imaging with semiconductor quantum dots." Nature Biotechnology **22**(8): 969-976.

Garcia, M. A. (2011). "Surface plasmons in metallic nanoparticles: fundamentals and applications." Journal of Physics D: Applied Physics **44**(28): 283001.

Garcia, R. (2010). Amplitude Modulation Atomic Force Microscopy. Wiley-VCH.

Ge, L., S. Sethi, L. Ci, P. M. Ajayan and A. Dhinojwala (2007). "Carbon nanotube-based synthetic gecko tapes." Proceedings of the National Academy of Sciences of the United States of America **104**(26): 10792-10795.

Geim, A. K. and K. S. Novoselov (2007). "The rise of graphene." Nature Materials **6**(3): 183-191.

Geisse, N. A. (2009). "AFM and combined optical techniques." Materials Today **12**(7-8): 40-45.

Gerber, C. and H. P. Lang (2006). "How the doors to the nanoworld were opened." Nature Nanotechnology **1**(1): 3-5.

Gharghi, M., C. Gladden, T. Zentgraf, Y. Liu, X. Yin, J. Valentine and X. Zhang (2011). "A Carpet Cloak for Visible Light." Nano Letters **11**(7): 2825-2828.

Giessibl, F. J., S. Hembacher, H. Bielefeldt and J. Mannhart (2000). "Subatomic Features on the Silicon (111)-(7×7) Surface Observed by Atomic Force Microscopy." Science **289**(5478): 422-425.

Glatter, O. and O. Kratky (1982). Small Angle X-ray Scattering. Academic Press.

Gobin, A. M., D. P. O'Neal, D. M. Watkins, N. J. Halas, R. A. Drezek and J. L. West (2005). "Near infrared laser-tissue welding using nanoshells as an exogenous absorber." Lasers in Surgery and Medicine **37**(2): 123-129.

Gontard, L. C., R. E. Dunin-Borkowski, M. H. Gass, A. L. Bleloch and D. Ozkaya (2009). "Three-dimensional shapes and structures of lamellar-twinned fcc nanoparticles using ADF STEM." Journal of Electron Microscopy **58**(3): 167-174.

Goodman, R. P., I. A. T. Schaap, C. F. Tardin, C. M. Erben, R. M. Berry, C. F. Schmidt and A. J. Turberfield (2005). "Chemistry: Rapid chiral assembly of rigid DNA building blocks for molecular nanofabrication." Science **310**(5754): 1661-1665.

Gosline, J. M., P. A. Guerette, C. S. Ortlepp and K. N. Savage (1999). "The mechanical design of spider silks: from fibroin sequence to mechanical function." Journal of Experimental Biology **202**(23): 3295-3303.

Grant, S. G., J. Jessee, F. R. Bloom and D. Hanahan (1990). "Differential plasmid rescue from transgenic mouse DNAs into Escherichia coli methylation-restriction mutants." Proceedings of the National Academy of Sciences of the United States of America **87**(12): 4645-4649.

Haes, A. J. and R. P. Van Duyne (2002). "A nanoscale optical biosensor: sensitivity and selectivity of an approach based on the localized surface plasmon resonance spectroscopy of triangular silver nanoparticles." Journal of the American Chemical Society **124**(35): 10596-10604.

Haguenau, F., P. W. Hawkes, J. L. Hutchison, B. Satiat–Jeunemaître, G. T. Simon and D. B. Williams (2003). "Key Events in the History of Electron Microscopy." Microscopy and Microanalysis **9**(02): 96-138.

Haruta, M. (2003). "When Gold Is Not Noble: Catalysis by Nanoparticles." The Chemical Record **3**(2): 75-87.

Haruta, M., T. Kobayashi, H. Sano and N. Yamada (1987). "Novel Gold Catalysts for the Oxidation of Carbon Monoxide at a Temperature far Below 0°C." Chemistry Letters **16**(2): 405-408.

Heintzmann, R. and G. Ficz (2006). "Breaking the resolution limit in light microscopy." Briefings in Functional Genomics & Proteomics **5**(4): 289-301.

Heinz, W. F. and J. H. Hoh (1999). "Spatially resolved force spectroscopy of biological surfaces using the atomic force microscope." Trends in Biotechnology **17**(4): 143-150.

Hell, S. W. and J. Wichmann (1994). "Breaking the diffraction resolution limit by stimulated emission: stimulated-emission-depletion fluorescence microscopy." Optics Letters **19**(11): 780-782.

Horcas, I., R. Fernandez, J. M. Gomez-Rodriguez, J. Colchero, J. Gomez-Herrero and A. M. Baro (2007). "WSXM: A software for scanning probe microscopy and a tool for nanotechnology." Review of Scientific Instruments **78**(1): 013705-013708.

Hossain, S. T. and S. K. Mukherjee (2013). "Toxicity of cadmium sulfide (CdS) nanoparticles against Escherichia coli and HeLa cells." Journal of Hazardous Materials **260**(0): 1073-1082.

Huh, Y.-M., Y.-W. Jun, H.-T. Song, S. Kim, J.-S. Choi, J.-H. Lee, S. Yoon, K.-S. Kim, J.-S. Shin, J.-S. Suh and J. Cheon (2005). "In Vivo Magnetic Resonance Detection of Cancer by Using Multifunctional Magnetic Nanocrystals." Journal of the American Chemical Society **127**(35): 12387-12391.

Humphris, A. D. L., M. J. Miles and J. K. Hobbs (2005). "A mechanical microscope: High-speed atomic force microscopy." Applied Physics Letters **86**(3): 034106-034103.

Hunt, G., I. Lynch, F. Cassee, R. Handy, T. Fernandes, M. Berges, T. Kuhlbusch, M. Dusinska and M. Riediker (2013). "Towards a Consensus View on Understanding Nanomaterials Hazards and Managing Exposure: Knowledge Gaps and Recommendations." Materials **6**(3): 1090-1117.

Hutter, E. and J. H. Fendler (2004). "Exploitation of Localized Surface Plasmon Resonance." Advanced Materials **16**(19): 1685-1706.

Hutter, J. L. and J. Bechhoefer (1993). "Calibration of atomic-force microscope tips." Review of Scientific Instruments **64**(7): 1868-1868.

Hwang, E. T., J. H. Lee, Y. J. Chae, Y. S. Kim, B. C. Kim, B.-I. Sang and M. B. Gu (2008). "Analysis of the Toxic Mode of Action of Silver Nanoparticles Using Stress-Specific Bioluminescent Bacteria." Small **4**(6): 746-750.

Iijima, S. (1991). "Helical microtubules of graphitic carbon." Nature **354**(6348): 56-58.

Jana, N. R., L. Gearheart and C. J. Murphy (2001). "Seeding growth for size control of 5-40 nm diameter gold nanoparticles." Langmuir **17**(22): 6782-6786.

Jana, N. R. and X. Peng (2003). "Single-Phase and Gram-Scale Routes toward Nearly Monodisperse Au and Other Noble Metal Nanocrystals." Journal of the American Chemical Society **125**(47): 14280-14281.

Jesse, S., S. V. Kalinin, R. Proksch, A. P. Baddorf and B. J. Rodriguez (2007). "The band excitation method in scanning probe microscopy for rapid mapping of energy dissipation on the nanoscale." Nanotechnology **18**(43): 435503-435503.

Jian, J. K., X. L. Chen, W. J. Wang, L. Dai and Y. P. Xu (2003). "Growth and morphologies of large-scale SnO2 nanowires, nanobelts and nanodendrites." Applied Physics A **76**(2): 291-294.

Jin, R., Y. W. Cao, C. A. Mirkin, K. L. Kelly, G. C. Schatz and J. G. Zheng (2001). "Photoinduced conversion of silver nanospheres to nanoprisms." Science **294**(5548): 1901-1901.

Johannsen, M., U. Gneveckow, L. Eckelt, A. Feussner, N. Waldöfner, R. Scholz, S. Deger, P. Wust, S. A. Loening and A. Jordan (2005). "Clinical hyperthermia of prostate cancer using magnetic nanoparticles: Presentation of a new interstitial technique." International Journal of Hyperthermia **21**(7): 637-647.

Jollès, P. and J. Jollès (1984). "What's new in lysozyme research?" Molecular and Cellular Biochemistry **63**(2): 165-189.

Jones, N., B. Ray, K. T. Ranjit and A. C. Manna (2008). "Antibacterial activity of ZnO nanoparticle suspensions on a broad spectrum of microorganisms." FEMS Microbiology Letters **279**(1): 71-76.

Jung, W. K., H. C. Koo, K. W. Kim, S. Shin, S. H. Kim and Y. H. Park (2008). "Antibacterial activity and mechanism of action of the silver ion in Staphylococcus aureus and Escherichia coli." Applied and Environmental Microbiology **74**(7): 2171-2178.

Kahlweit, M. (1975). "Ostwald ripening of precipitates." Advances in Colloid and Interface Science **5**(1): 1-35.

Kelly, K. L., E. Coronado, L. L. Zhao and G. C. Schatz (2003). "The Optical Properties of Metal Nanoparticles: The Influence of Size, Shape, and Dielectric Environment." The Journal of Physical Chemistry B **107**(3): 668-677.

Keun Kwon, I., S. Kidoaki and T. Matsuda (2005). "Electrospun nano- to microfiber fabrics made of biodegradable copolyesters: structural characteristics, mechanical properties and cell adhesion potential." Biomaterials **26**(18): 3929-3939.

Khizroev, S. and D. Litvinov (2004). "Focused-ion-beam-based rapid prototyping of nanoscale magnetic devices." Nanotechnology **15**(3): R7.

Kim, Y. H., D. K. Lee, H. G. Cha, C. W. Kim, Y. C. Kang and Y. S. Kang (2006). "Preparation and Characterization of the Antibacterial Cu Nanoparticle Formed on the Surface of SiO2 Nanoparticles." The Journal of Physical Chemistry B **110**(49): 24923-24928.

Kisielowski, C., B. Freitag, M. Bischoff, H. van Lin, S. Lazar, G. Knippels, P. Tiemeijer, M. van der Stam, S. von Harrach, M. Stekelenburg, M. Haider, S. Uhlemann, H. Müller, P. Hartel, B. Kabius, D. Miller, I. Petrov, E. A. Olson, T. Donchev, E. A. Kenik, A. R. Lupini, J. Bentley, S. J. Pennycook, I. M. Anderson, A. M. Minor, A. K. Schmid, T. Duden, V. Radmilovic, Q. M. Ramasse, M. Watanabe, R. Erni, E. A. Stach, P. Denes and U. Dahmen (2008). "Detection of Single Atoms and Buried Defects in Three Dimensions by Aberration-Corrected Electron Microscope with 0.5-Å Information Limit." Microscopy and Microanalysis **14**(05): 469-477.

Kitano, K. and A. Tomasz (1979). "Triggering of autolytic cell wall degradation in Escherichia coli by beta-lactam antibiotics." Antimicrobial Agents and Chemotherapy **16**(6): 838-848.

Kittler, S., C. Greulich, J. Diendorf, M. Köller and M. Epple (2010). "Toxicity of Silver Nanoparticles Increases during Storage Because of Slow Dissolution under Release of Silver Ions." Chemistry of Materials **22**(16): 4548-4554.

Klasen, H. J. (2000). "Historical review of the use of silver in the treatment of burns. I. Early uses." Burns **26**(2): 117-130.

Knoll, M. and E. Ruska (1932). "Beitrag zur geometrischen Elektronenoptik. I." Annalen der Physik **404**(5): 607-640.

Kohl, H. and L. Reimer (2008). Transmission Electron Microscopy. Springer.

Kopito, R. R. (2000). "Aggresomes, inclusion bodies and protein aggregation." Trends in Cell Biology **10**(12): 524-530.

Krug, H. F. and P. Wick (2011). "Nanotoxicology: an interdisciplinary challenge." Angewandte Chemie International Edition **50**(6): 1260-1278.

Lansdown, A. B. G. (2010). Silver in Healthcare: Its Antimicrobial Efficiency and Safety in Use. RSC Publishing.

Lee, C., J. Y. Kim, W. I. Lee, K. L. Nelson, J. Yoon and D. L. Sedlak (2008). "Bactericidal effect of zero-valent iron nanoparticles on Escherichia coli." Environmental Science & Technology **42**(13): 4927-4933.

Li, W., Y. Guo and P. Zhang (2010). "SERS-Active Silver Nanoparticles Prepared by a Simple and Green Method." The Journal of Physical Chemistry C **114**(14): 6413-6417.

Li, W. Z., S. S. Xie, L. X. Qian, B. H. Chang, B. S. Zou, W. Y. Zhou, R. A. Zhao and G. Wang (1996). "Large-Scale Synthesis of Aligned Carbon Nanotubes." Science **274**(5293): 1701-1703.

Liau, S. Y., D. C. Read, W. J. Pugh, J. R. Furr and A. D. Russell (1997). "Interaction of silver nitrate with readily identifiable groups: relationship to the antibacterial action of silver ions." Letters in Applied Microbiology **25**(4): 279-283.

Liff, S. M., N. Kumar and G. H. McKinley (2007). "High-performance elastomeric nanocomposites via solvent-exchange processing." Nature Materials **6**(1): 76-83.

Lim, B., M. Jiang, P. H. C. Camargo, E. C. Cho, J. Tao, X. Lu, Y. Zhu and Y. Xia (2009). "Pd-Pt Bimetallic Nanodendrites with High Activity for Oxygen Reduction." Science **324**(5932): 1302-1305.

Link, S. and M. A. El-Sayed (2000). "Shape and size dependence of radiative, non-radiative and photothermal properties of gold nanocrystals." International Reviews in Physical Chemistry **19**(3): 409-453.

Liu, J. and R. Hurt (2010). "Ion Release Kinetics and Particle Persistence in Aqueous Nano-Silver Colloids." Environmental Science & Technology **44**(6): 2169-2175.

Liu, J., D. A. Sonshine, S. Shervani and R. H. Hurt (2010). "Controlled release of biologically active silver from nanosilver surfaces." ACS Nano **4**(11): 6903-6913.

Liu, S., A. K. Ng, R. Xu, J. Wei, C. M. Tan, Y. Yang and Y. Chen (2010). "Antibacterial action of dispersed single-walled carbon nanotubes on Escherichia coli and Bacillus subtilis investigated by atomic force microscopy." Nanoscale **2**(12): 2744-2750.

Liu, S., L. Wei, L. Hao, N. Fang, M. W. Chang, R. Xu, Y. Yang and Y. Chen (2009). "Sharper and Faster "Nano Darts" Kill More Bacteria: A Study of Antibacterial Activity of Individually Dispersed Pristine Single-Walled Carbon Nanotube." ACS Nano **3**(12): 3891-3902.

Lok, C.-N., C.-M. Ho, R. Chen, Q.-Y. He, W.-Y. Yu, H. Sun, P. K.-H. Tam, J.-F. Chiu and C.-M. Che (2006). "Proteomic Analysis of the Mode of Antibacterial Action of Silver Nanoparticles." Journal of Proteome Research **5**(4): 916-924.

Lok, C.-N., C.-M. Ho, R. Chen, Q.-Y. He, W.-Y. Yu, H. Sun, P. K.-H. Tam, J.-F. Chiu and C.-M. Che (2007). "Silver nanoparticles: partial oxidation and antibacterial activities." Journal of Biological Inorganic Chemistry **12**(4): 527-534.

McKendry, R., M.-E. Theoclitou, T. Rayment and C. Abell (1998). "Chiral discrimination by chemical force microscopy." Nature **391**(6667): 566-568.

McKendry, R. A. (2012). "Nanomechanics of superbugs and superdrugs: new frontiers in nanomedicine." Biochemical Society Transactions **40**(4): 603-608.

Meyer, G. and N. M. Amer (1988). "Novel optical approach to atomic force microscopy." Applied Physics Letters **53**(12): 1045-1047.

Mitchell, D. G. and M. S. Cohen (2004). MRI Principles. Saunders.

Mitchell, R. and J.-D. Gu (2010). Environmental Microbiology. Wiley-Blackwell.

Morales, A. M. and C. M. Lieber (1998). "A Laser Ablation Method for the Synthesis of Crystalline Semiconductor Nanowires." Science **279**(5348): 208-211.

Morita, S., I. Otsuka and N. Mikoshiba (1988). "Scanning tunneling microscopy in air and liquid." Physica Scripta **38**(2): 277.

Morones, J. R., J. L. Elechiguerra, A. Camacho, K. Holt, J. B. Kouri, J. T. Ramírez and M. J. Yacaman (2005). "The bactericidal effect of silver nanoparticles." Nanotechnology **16**: 2346-2346.

Moser, J., J. Guttinger, A. Eichler, M. J. Esplandiu, D. E. Liu, M. I. Dykman and A. Bachtold (2013). "Ultrasensitive force detection with a nanotube mechanical resonator." Nature Nanotechnology **8**(7): 493-496.

Mott, D., B. Cotts, I. I. S. Lim, J. Luo, H.-Y. Park, P. N. Njoki, M. J. Schadt and C.-J. Zhong (2008). "Size Determination of Nanoparticles Based on Tapping-Mode Atomic Force Microscopy Measurements." Journal of Scanning Probe Microscopy **3**(1): 1-8.

Müller, D. J. and Y. F. Dufrêne (2011). "Atomic force microscopy: a nanoscopic window on the cell surface." Trends in Cell Biology **21**(8): 461-469.

Mulvaney, P. (1996). "Surface Plasmon Spectroscopy of Nanosized Metal Particles." Langmuir **12**(3): 788-800.

Murdock, R. C., L. Braydich-Stolle, A. M. Schrand, J. J. Schlager and S. M. Hussain (2008). "Characterization of nanomaterial dispersion in solution prior to in vitro exposure using dynamic light scattering technique." Toxicological Sciences **101**(2): 239-253.

Murray, P. R. (2007). Manual of Clinical Microbiology. ASM Press.

Nanotechnologies, T. P. o. E. (2014). "Consumer Products Inventory." Retrieved March, 2014, from http://www.nanotechproject.org/inventories/consumer/.

Neidhardt, F. C. (1996). Escherichia coli and Salmonella: cellular and molecular biology. ASM Press

Nelson, C. M., R. P. Jean, J. L. Tan, W. F. Liu, N. J. Sniadecki, A. A. Spector and C. S. Chen (2005). "Emergent patterns of growth controlled by multicellular form and mechanics." Proceedings of the National Academy of Sciences of the United States of America **102**(33): 11594-11599.

Newman, T. H. (1987). "High resolution patterning system with a single bore objective lens." Journal of Vacuum Science & Technology B: Microelectronics and Nanometer Structures **5**(1): 88-88.

NIH. (2013). "ClinicalTrials.gov." Retrieved 3 October, 2013, from http://clinicaltrials.gov/.

Nonnenmacher, M., M. P. O'Boyle and H. K. Wickramasinghe (1991). "Kelvin probe force microscopy." Applied Physics Letters **58**(25): 2921-2923.

Oberdorster, G., E. Oberdorster and J. Oberdorster (2005). "Nanotoxicology: An Emerging Discipline Evolving from Studies of Ultrafine Particles." Environmental Health Perspectives **113**(7): 823-839.

Pal, S., Y. K. Tak and J. M. Song (2007). "Does the antibacterial activity of silver nanoparticles depend on the shape of the nanoparticle? A study of the Gram-negative bacterium Escherichia coli." Applied and Environmental Microbiology **73**(6): 1712-1720.

Palade, G. E. (1952). "A STUDY OF FIXATION FOR ELECTRON MICROSCOPY." The Journal of Experimental Medicine **95**(3): 285-298.

Park, H.-J., J. Y. Kim, J. Kim, J.-H. Lee, J.-S. Hahn, M. B. Gu and J. Yoon (2009). "Silver-ion-mediated reactive oxygen species generation affecting bactericidal activity." Water Research **43**(4): 1027-1032.

Patnaik, S. and D. Hopkins (2004). Strength of Materials: A Unified Theory. Elsevier: Butterworth-Heinemann.

Paulo, Á. and R. García (2001). "Tip-surface forces, amplitude, and energy dissipation in amplitude-modulation (tapping mode) force microscopy." Physical Review B **64**(19): 1-4.

Pecharsky, V. K. and P. Y. Zavalij (2009). Fundamentals of Powder Diffraction and Structural Characterization of Materials. Springer Science+Business Media.

Pecora, R. (1985). Dynamic Light Scattering: Applications of Photon Correlation Spectroscopy. Plenum Press.

Peiris, P. M., L. Bauer, R. Toy, E. Tran, J. Pansky, E. Doolittle, E. Schmidt, E. Hayden, A. Mayer, R. A. Keri, M. A. Griswold and E. Karathanasis (2012). "Enhanced Delivery of Chemotherapy to Tumors Using a Multicomponent Nanochain with Radio-Frequency-Tunable Drug Release." ACS Nano **6**(5): 4157-4168.

Pillai, S., K. R. Catchpole, T. Trupke and M. A. Green (2007). "Surface plasmon enhanced silicon solar cells." Journal of Applied Physics **101**(9): 093105-093108.

Ping, G., L. Huimin, H. Xiaoxiao, W. Kemin, H. Jianbing, T. Weihong, Z. Shouchun and Y. Xiaohai (2007). "Preparation and antibacterial activity of Fe3O4 @Ag nanoparticles." Nanotechnology **18**(28): 285604.

Plodinec, M., M. Loparic, R. Suetterlin, H. Herrmann, U. Aebi and C.-A. Schoenenberger (2011). "The nanomechanical properties of rat fibroblasts are modulated by interfering with the vimentin intermediate filament system." Journal of Structural Biology **174**(3): 476-484.

Popov, A. P., A. V. Priezzhev, J. Lademann and R. Myllylä (2005). "TiO2 nanoparticles as an effective UV-B radiation skin-protective compound in sunscreens." Journal of Physics D: Applied Physics **38**(15): 2564.

Postgate, J. (2000). Microbes and Man. Cambridge Univesity Press.

Poynton, H. C., J. M. Lazorchak, C. a. Impellitteri, B. J. Blalock, K. Rogers, H. J. Allen, A. Loguinov, J. L. Heckman and S. Govindasmawy (2012). "Toxicogenomic Responses of Nanotoxicity in Daphnia magna Exposed to Silver Nitrate and Coated Silver Nanoparticles." Environmental Science & Technology **46**(11): 6288-6296.

Radmacher, M., M. Fritz, C. M. Kacher, J. P. Cleveland and P. K. Hansma (1996). "Measuring the viscoelastic properties of human platelets with the atomic force microscope." Biophysical Journal **70**(1): 556-567.

Ramirez, M. S. and M. E. Tolmasky (2010). "Aminoglycoside modifying enzymes." Drug Resistance Updates **13**(6): 151-171.

Raschke, G., S. Kowarik, T. Franzl, C. Sönnichsen, T. A. Klar, J. Feldmann, A. Nichtl and K. Kürzinger (2003). "Biomolecular Recognition Based on Single Gold Nanoparticle Light Scattering." Nano Letters **3**(7): 935-938.

Recommendation (2011/696/EU). Commission Recommendation of 18 October 2011 on the definition of nanomaterial**:** 38-40.

Riccardi, C. and I. Nicoletti (2006). "Analysis of apoptosis by propidium iodide staining and flow cytometry." Nature Protocols **1**(3): 1458-1461.

Rice, J. A. (2007). Mathematical Statistics and Data Analysis. Brooks/Cole.

Ridler, T. W. and S. Calvard (1978). "Picture Thresholding Using an Iterative Selection Method." Systems, Man and Cybernetics, IEEE Transactions on **8**(8): 630-632.

Rogach, A. L. (2011). "Fluorescence energy transfer in hybrid structures of semiconductor nanocrystals." Nano Today **6**(4): 355-365.

Rolfe, M. D., C. J. Rice, S. Lucchini, C. Pin, A. Thompson, A. D. S. Cameron, M. Alston, M. F. Stringer, R. P. Betts, J. Baranyi, M. W. Peck and J. C. D. Hinton (2012). "Lag Phase Is a Distinct Growth Phase That Prepares Bacteria for Exponential Growth and Involves Transient Metal Accumulation." Journal of Bacteriology **194**(3): 686-701.

Rotsch, C. and M. Radmacher (2000). "Drug-induced changes of cytoskeletal structure and mechanics in fibroblasts: an atomic force microscopy study." Biophysical Journal **78**(1): 520-535.

Rugar, D., H. J. Mamin, P. Guethner, S. E. Lambert, J. E. Stern, I. McFadyen and T. Yogi (1990). "Magnetic force microscopy: General principles and application to longitudinal recording media." Journal of Applied Physics **68**(3): 1169-1183.

Ruparelia, J. P., A. K. Chatterjee, S. P. Duttagupta and S. Mukherji (2008). "Strain specificity in antimicrobial activity of silver and copper nanoparticles." Acta Biomaterialia **4**(3): 707-716.

Rust, M. J., M. Bates and X. Zhuang (2006). "Sub-diffraction-limit imaging by stochastic optical reconstruction microscopy (STORM)." Nature Methods **3**(10): 793-796.

Sahin, O. and N. Erina (2008). "High-resolution and large dynamic range nanomechanical mapping in tapping-mode atomic force microscopy." Nanotechnology **19**(44): 445717-445717.

Sayre, R. M. and N. Kollias (1990). "Physical sunscreens." Journal of the Society of Cosmetic Chemists **109**(April): 103-109.

Schatten, H. (2013). Scanning Electron Microscopy for the Life Sciences. Cambridge University Press.

Schemmel, A. and H. E. Gaub (1999). "Single molecule force spectrometer with magnetic force control and inductive detection." Review of Scientific Instruments **70**(2): 1313-1317.

Schmidt, W. (2005). Optical Spectroscopy in Chemistry and Life Sciences. Wiley-VCH.

Schreurs, W. J. (1982). "Effect of silver ions on transport and retention of phosphate by Escherichia coli." Journal of Bacteriology **152**(1): 7-13.

Segal, M. (2009). "Surely you're happy, Mr. Feynman!" Nature Nanotechnology **4**(12): 786-788.

Serwer, P. (1983). "Agarose gels: Properties and use for electrophoresis." Electrophoresis **4**(6): 375-382.

Shekhawat, G. S. and V. P. Dravid (2005). "Nanoscale imaging of buried structures via scanning near-field ultrasound holography." Science **310**(5745): 89-92.

Shkilnyy, A., M. Soucé, P. Dubois, F. Warmont, M.-L. Saboungi and I. Chourpa (2009). "Poly(ethylene glycol)-stabilized silver nanoparticles for bioanalytical applications of SERS spectroscopy." The Analyst **134**(9): 1868-1872.

Siddhartha, S., B. Tanmay, R. Arnab, S. Gajendra, P. Ramachandrarao and D. Debabrata (2007). "Characterization of enhanced antibacterial effects of novel silver nanoparticles." Nanotechnology **18**(22): 225103.

Siegel, S. and N. J. Castellan (1998). Nonparametric Statistics for The Behavioral Sciences. McGraw-Hill.

Singer, S. J. (1959). "Preparation of an Electron-dense Antibody Conjugate." Nature **183**(4674): 1523-1524.

Slonczewski, J. and J. W. Foster (2009). Microbiology: an evolving science. W.W. Norton & Co.

Soenen, S. J., J. Demeester, S. C. De Smedt and K. Braeckmans (2013). "Turning a frown upside down: Exploiting nanoparticle toxicity for anticancer therapy." Nano Today **8**(2): 121-125.

Sondi, I. and B. Salopek-Sondi (2004). "Silver nanoparticles as antimicrobial agent: a case study on E. coli as a model for Gram-negative bacteria." Journal of Colloid and Interface Science **275**(1): 177-182.

Sotiriou, G. A. and S. E. Pratsinis (2010). "Antibacterial activity of nanosilver ions and particles." Environmental Science & Technology **44**(14): 5649-5654.

Spellberg, B., R. Guidos, D. Gilbert, J. Bradley, H. W. Boucher, W. M. Scheld, J. G. Bartlett, J. Edwards and t. I. D. S. o. America (2008). "The Epidemic of Antibiotic-Resistant Infections: A Call to Action for the Medical Community from the Infectious Diseases Society of America." Clinical Infectious Diseases **46**(2): 155-164.

Spratt, B. G. (1983). "Penicillin-binding Proteins and the Future of Beta-Lactam Antibiotics." Journal of General Microbiology **129**: 1247-1260.

Stevenson, A. P. Z., D. Blanco Bea, S. Civit, S. Antoranz Contera, A. Iglesias Cerveto and S. Trigueros (2012). "Three strategies to stabilise nearly monodispersed silver nanoparticles in aqueous solution." Nanoscale Research Letters **7**: 151.

Stokes, D. J. (2008). Principles and Practice of Variable Pressure/Environmental Scanning Electron Microscopy (VP-ESEM). John Wiley & Sons.

Sun, C., K. Du, C. Fang, N. Bhattarai, O. Veiseh, F. Kievit, Z. Stephen, D. Lee, R. G. Ellenbogen, B. Ratner and M. Zhang (2010). "PEG-Mediated Synthesis of Highly Dispersive Multifunctional Superparamagnetic Nanoparticles: Their Physicochemical Properties and Function In Vivo." ACS Nano **4**(4): 2402-2410.

Suresh, A. K., D. a. Pelletier and M. J. Doktycz (2013). "Relating nanomaterial properties and microbial toxicity." Nanoscale **5**(2): 463-474.

Suresh, S. (2007). "Biomechanics and biophysics of cancer cells." Acta Biomaterialia **3**(4): 413-438.

Taratula, O., A. Kuzmov, M. Shah, O. B. Garbuzenko and T. Minko (2013). "Nanostructured lipid carriers as multifunctional nanomedicine platform for pulmonary co-delivery of anticancer drugs and siRNA." Journal of Controlled Release **171**(3): 349-357.

Tetard, L., A. Passian, K. T. Venmar, R. M. Lynch, B. H. Voy, G. Shekhawat, V. P. Dravid and T. Thundat (2008). "Imaging nanoparticles in cells by nanomechanical holography." Nature Nanotechnology **3**(8): 501-505.

Thompson, M. and J. N. Walsh (1989). Handbook of Inductively Coupled Plasma Spectrometry. Blackie Academic & Professional.

Toshima, N. and T. Yonezawa (1998). "Bimetallic nanoparticles—novel materials for chemical and physical applications." New Journal of Chemistry **22**(11): 1179-1201.

Trigueros, S. (2008). *Personal communication*.

Trigueros, S., A. Raman, A. Cartagena, A. P. Z. Stevenson, M. Susilo, E. Nauman and S. Antoranz Contera (2011). "Mapping nanomechanical properties of live cells using multi-harmonic atomic force microscopy." Nature Nanotechnology **6**(12): 809-814.

Tsuji, N., R. Ueji, Y. Minamino and Y. Saito (2002). "A new and simple process to obtain nano-structured bulk low-carbon steel with superior mechanical property." Scripta Materialia **46**(4): 305-310.

Turkevich, J. and J. Hillier (1949). "Electron Microscopy of Colloidal Systems." Analytical Chemistry **21**(4): 475-485.

Turkevich, J., P. C. Stevenson and J. Hillier (1951). "A study of the nucleation and growth processes in the synthesis of colloidal gold." Discussions of the Faraday Society **11**(c): 55-75.

Valden, M., X. Lai and D. W. Goodman (1998). "Onset of Catalytic Activity of Gold Clusters on Titania with the Appearance of Nonmetallic Properties." Science **281**(5383): 1647-1650.

Vallee, R. B. and P. Hook (2003). "Molecular motors: A magnificent machine." Nature **421**(6924): 701-702.

Verma, A. and F. Stellacci (2010). "Effect of surface properties on nanoparticle-cell interactions." Small **6**(1): 12-21.

Vieu, C., F. Carcenac, A. Pépin, Y. Chen, M. Mejias, A. Lebib, L. Manin-Ferlazzo, L. Couraud and H. Launois (2000). "Electron beam lithography: Resolution limits and applications." Applied Surface Science **164**(1-4): 111-117.

Villarrubia, J. S. (1997). "Algorithms for Scanned Probe Microscope Image Simulation , Surface Reconstruction , and Tip Estimation." Journal Of Research Of The National Institute Of Standards And Technology **102**(4): 425-454.

Vogel, V. (2008). 5. Nanomedicine. Weinheim : Wiley-VCH

Voïtchovsky, K., S. Antoranz Contera, M. Kamihira, A. Watts and J. F. Ryan (2006). "Differential stiffness and lipid mobility in the leaflets of purple membranes." Biophysical Journal **90**(6): 2075-2085.

Voïtchovsky, K., J. J. Kuna, S. Antoranz Contera, E. Tosatti and F. Stellacci (2010). "Direct mapping of the solid-liquid adhesion energy with subnanometre resolution." Nature Nanotechnology **5**(April): 401-405.

Wang, Z. L. (2003). "New developments in transmission electron microscopy for nanotechnology." Advanced Materials **15**(18): 1497-1514.

Watts, J. F. and J. Wolstenholme (2003). An Introduction to Surface Analysis by XPS and AES. Wiley.

Waxman, D. J. and J. L. Strominger (1983). "Penicillin-binding proteins and the mechanism of action of beta-lactam antibiotics." Annual Review of Biochemistry **52**: 825-869.

Weisenhorn, A. L., P. K. Hansma, T. R. Albrecht and C. F. Quate (1989). "Forces in atomic force microscopy in air and water." Applied Physics Letters **54**(26): 2651-2653.

Weissleder, R. (2001). "A clearer vision for in vivo imaging." Nature Biotechnology **19**(4): 316-317.

Weller, H. (1993). "Colloidal Semiconductor Q-Particles: Chemistry in the Transition Region Between Solid State and Molecules." Angewandte Chemie International Edition **32**(1): 41-53.

Williams, R. C. (1953). "A method of freeze-drying for electron microscopy." Experimental Cell Research **4**(1): 188-201.

Witholt, B., M. Boekhout, M. Brock, J. Kingma, H. V. Heerikhuizen and L. D. Leij (1976). "An efficient and reproducible procedure for the formation of spheroplasts from variously grown Escherichia coli." Analytical Biochemistry **74**(1): 160-170.

Wu, G., R. H. Datar, K. M. Hansen, T. Thundat, R. J. Cote and A. Majumdar (2001). "Bioassay of prostate-specific antigen (PSA) using microcantilevers." Nature Biotechnology **19**(9): 856-860.

Xiu, Z.-M., J. Ma and P. J. J. Alvarez (2011). "Differential effect of common ligands and molecular oxygen on antimicrobial activity of silver nanoparticles versus silver ions." Environmental Science & Technology **45**(20): 9003-9008.

Xiu, Z.-M., Q.-B. Zhang, H. L. Puppala, V. L. Colvin and P. J. J. Alvarez (2012). "Negligible particle-specific antibacterial activity of silver nanoparticles." Nano Letters **12**(8): 4271-4275.

Xu, M., N. Lu, H. Xu, D. Qi, Y. Wang, S. Shi and L. Chi (2010). "Fabrication of flexible superhydrophobic biomimic surfaces." Soft Matter **6**(7): 1438-1438.

Yang, X., W. Yang, Q. Wang, H. Li, K. Wang, L. Yang and W. Liu (2010). "Atomic force microscopy investigation of the characteristic effects of silver ions on Escherichia coli and Staphylococcus epidermidis." Talanta **81**(4-5): 1508-1512.

Yasuda, T., T. Okuno and H. Yasuda (1994). "Contact Angle of Water on Polymer Surfaces." Langmuir **10**(7): 2435-2439.

Yoo, E., J. Kim, E. Hosono, H.-s. Zhou, T. Kudo and I. Honma (2008). "Large Reversible Li Storage of Graphene Nanosheet Families for Use in Rechargeable Lithium Ion Batteries." Nano Letters **8**(8): 2277–2282.

Yu, M.-F., O. Lourie, M. J. Dyer, K. Moloni, T. F. Kelly and R. S. Ruoff (2000). "Strength and Breaking Mechanism of Multiwalled Carbon Nanotubes Under Tensile Load." Science **287**(5453): 637-640.

Yurdumakan, B., N. R. Raravikar, P. M. Ajayan and A. Dhinojwala (2005). "Synthetic gecko foot-hairs from multiwalled carbon nanotubes." Chemical Communications(30): 3799-3801.

Zavascki, A. P., L. Z. Goldani, J. Li and R. L. Nation (2007). "Polymyxin B for the treatment of multidrug-resistant pathogens: a critical review." The Journal of Antimicrobial Chemotherapy **60**(6): 1206-1215.

Zhang, Q., J. Xie, Y. Yu and J. Y. Lee (2010). "Monodispersity control in the synthesis of monometallic and bimetallic quasi-spherical gold and silver nanoparticles." Nanoscale **2**(10): 1962-1975.

Zheng, G., F. Patolsky, Y. Cui, W. U. Wang and C. M. Lieber (2005). "Multiplexed electrical detection of cancer markers with nanowire sensor arrays." Nature Biotechnology **23**(10): 1294-1301.

Zheng, Q. and Q. Jiang (2002). "Multiwalled Carbon Nanotubes as Gigahertz Oscillators." Physical Review Letters **88**(4): 045503.

Zhong, Q., D. Inniss, K. Kjoller and V. B. Elings (1993). "Fractured polymer/silica fiber surface studied by tapping mode atomic force microscopy." Surface Science **290**(1–2): L688-L692.

Zhu, W., J. Xiao, D. Wang, J. Liu, J. Xiong, L. Liu, X. Zhang and Y. Zeng (2009). "Experimental study of nano-HA artificial bone with different pore sizes for repairing the radial defect." International Orthopaedics **33**(2): 567-571.